PNAS
www.pnas.org

Supplementary Information for

"Zinc isotopes in Late Pleistocene fossil teeth from a Southeast Asian cave setting preserve paleodietary information"

Nicolas Bourgon, Klervia Jaouen, Anne-Marie Bacon, Klaus Peter Jochum, Elise Dufour, Philippe Duringer, Jean-Luc Ponche, Renaud Joannes-Boyau, Quentin Boesch, Pierre-Olivier Antoine, Manon Hullot, Ulrike Weis, Ellen Schulz-Kornas, Manuel Trost, Denis Fiorillo, Fabrice Demeter, Elise Patole-Edoumba, Laura Shackelford, Tyler Dunn, Alexandra Zachwieja, Somoh Duangthongchit, Thongsa Sayavonkhamdy, Phonephanh Sichanthongtip, Daovee Sihanam, Viengkeo Souksavatdy, Jean-Jacques Hublin, Thomas Tütken

Corresponding author: Nicolas BOURGON
Email: nicolas_bourgon@eva.mpg.de

This PDF file includes:

www.pnas.org/cgi/doi/10.1073/pnas.1911744117

Supplementary Information 1: Context

1.1. Geology

1.1.1 Location and geological context

The studied area is located in the northeastern part of Laos about 290 km NNE from Vientiane, in the Hua Pan province (**Fig.S1**). The site can be reached by the road n°1C from Luang Prabang to the small city of Muang Hiam (also called Vieng Thong) (**Fig.S2**), and from there, towards the north approximately 60 km to Xoneuna city (also called Muang Xon) (**Fig.S3**). The cave is located 6 km SE from the center of the city.

The basement of the region consists of Palaeozoic granite and diorite (1). These rocks are covered with a widespread light metamorphic sedimentary formation characterized by grey to yellow poorly cemented arkosic sandstones interbedded with pelites, and attributed to the Silurian, or perhaps partly to the Devonian (1). This latter formation is strongly deformed and folded. This detrital sedimentary formation is capped by a thick limestone unit still poorly dated, and attributed by Saurin (1) to an interval between the Late Carboniferous (Moscovian) and the Permian, some outcrops displaying many tabulate corals (mostly tetracorals). Furthermore, crinoidal remains as well as calcified sponges (stromatoporoids) developed in laminated calcite with some vertical pillars, are frequent. The karstic formation belongs to the northern Annamitic Chain oriented broadly NNW-SSE. Locally, the thick limestone unit forms a variety of tower karsts that emerge here and there from the forest. This unit consists of a pluri-decametric massive sparitic dark-grey carbonate without marl intercalation. Grey to black cherts occur in some places often reworked inside the cave. The mountain contains a widespread karstic network in which bone-rich breccias and sandy clays can be found.

The Tam Hay Marklot cave is located at the foot of a karstic hill totally covered by forest (**Fig.S4a**). The entrance of the cave is constituted by a large and open chamber of about 10 m long and 8 m wide (**Fig.S4b-c**), but the entrance of the well-developed gallery (very narrow less than 0.60 m in diameter) (**Fig.S4d-e**) is at the end of this chamber. The first passageway leads to a first chamber of about 15 m long, and the second passageway to the main gallery, which can be followed entirely to the end of the cavity. The 235 m long cave consists of a succession of wide to narrow galleries ranging from one to ten meters wide (**Fig.S5**). The height of the main gallery is in average around three meters.

Some 150 m from the entrance, the gallery is partly flooded on about sixty meters. After, this part of the gallery narrows gradually ending in a dead-end. The soil of the gallery from the entrance to about two thirds of the cavity is entirely covered by a soft and partly wet light brown sediment formed by a sandy to gravely clays. The greatest part of the vertebrate remains was found in this soft sediment forming the soil of the cave, until at least the drowned part of the gallery. After this part, the cave ground is made up by solid flowstone. The soft sediment has a thickness of at least one meter. The lower part is more gravely. Since the vertebrate remains were mainly located in the first 40 cm, no further explorations were conducted deeper for the moment, but further investigations will be conducted in 2020.

1.1.2 Description and analysis of the sedimentary deposits

The karstic filling, homogeneous along the cave, is summarized in **Fig.S6** through three sections. The roof and walls of the cave are formed by a compact grey-colored limestone. Four different deposits were recognized in the cave: soft sandy to gravelly clays on the soil; well-cemented conglomerate mixed with breccias plastered on the wall from the base up to two-thirds of the height of the gallery; speleothems cemented on both roof and walls included on the conglomerate; and a 1 to 4 cm dark brown mud covering the soil and partly the walls from place to place. Details of the facies are given in **Fig.S7**:

- The soft sandy to gravelly clays cover almost the entire soil of the cave. The sedimentary facies greatly vary from place to place inside the cave, but generally displays pure silty to sandy sticky clays

in the first upper 30-60 cm, whereas the lower part up to a depth of one meter is made mainly of small to coarse-grained mixed gravels and clays. Furthermore, the lower part of the deposit is generally cross-bedded with numerous erosion surfaces. Most of the teeth come from the upper clayey sediment. Although the vertebrate remains can be found everywhere in the gallery from the entry to the drowned part of the gallery, their richness in this soft sediment varies from place to place. In some places close to the wall of the gallery, the soft sediment can be poorly to hardly cemented by calcite (**Fig.S7**). This calcitic cementation is a secondary diagenetic phenomenon due to the water circulation along the wall.
- The conglomerate and breccias plastered on the wall contain a large range of pebbles and cobbles up to 20 cm in size, cemented by small gravels and coarse-grained sandstones (**Fig.S7a**). The maturity of the clasts is highly variable. Full-rounded pebbles and cobbles are mixed with very angular clasts generally in contact with each other. The greater quantity of clasts consists of full-rounded fine-grained yellow colored sandstones sometimes rich in micas similar to the weakly metamorphic Devonian sandstones described above. The second type of clasts is constituted by angular square-shaped black cherts. The great hardness of these cryptocrystalline silica occurrences compared to the hardness of the sandstones can't explain the important difference in the maturity of the clasts. It is obvious that these two types of rocks of different maturity don't have the same sedimentary history. Cherts probably originated from the substratum of the cave (limestone formation) and have been transported over only short distances, whereas the composition of the sandstone suggests a long transport. In fact, similar black chert concretions can be found easily in situ in the limestone formation, thus their local provenience is indisputable. Concerning the sandstone pebbles, they are similar to those observed in the river two hundred meters below the Marklot cave in the valley.
- The speleothems (in green on **Fig.S7d**) cover the roof and walls (limestone substratum) in the entire gallery. In many places, speleothems obviously cover the conglomerate plastered on the walls, but are also covered by the soft clayey sediments, which are the last deposited sediments.
- The thinnest deposit is a centimetric scale brown soft mud that covers all of the other deposits up to one-meter height from the floor of the gallery. That suggests an episodic flooding of the cave during the rainy season, also explaining the cross-bedded sands and gravels in some places, on the soft sediment of the floor.

1.1.3 Cave filling history

The study of the cavity reveals a complicated depositional history, which consists of at least four types of deposits, roughly superimposed upon each other (**Fig.S7**). The oldest deposit is the conglomerate/breccias covered by all of the other sediments (speleothems on the roof and walls, sandy to gravelly clays on the soil and soft mud, successively).

The perfect imbrication of the flat pebbles (red arrow on **Fig.S7a-b**) suggests a water flow orientated from inside to outside, which raises several questions. First, there is today no gallery or pipe being able to bring such conglomerate inside the cave. Secondly, there is today no likely origin on the top of the tower karst sandstone formation that could have provided all of this gravel/pebble material. Similar gravels and pebbles (mainly the sandstones) can be found in the current river crossing the town two hundred meters below, which also strongly suggests that this intrakarstic conglomerate could be very old. With an incision of 0.2 m per thousand years on average (2), this deposit situated at least 200 m above the current alluvial plain could be potentially 2 million years old.

The presence of relicts of conglomerates plastered very high on the walls shows that the gallery was filled by sediment to the roof, and then was almost entirely emptied before the sandy clay unit was deposited on the cave floor. That means that a major phase of karstic erosion separates the two described sedimentary units, and that there is a long range of time between the conglomerate and the clayey sediment (red line on **Fig.S7d**). The numerous erosion surfaces inside the clayey deposits of the soil, as well as the vertical and lateral alternation of mud, sands and small gravels, suggest that the deposit has been sedimented in several phases. Furthermore, the occurrence of a thin layer of sticky mud plastered on the wall, as well as marks of the level of the water at different heights inside the main

gallery, are evidence that the cave is still episodically flooded today, most likely during the rainy seasons. This can also explain why the concentration of fossil remains is not uniform in the cave, but occurs in placer-like loci. Furthermore, some marks of the level of the water in the cave (upper limit of the soft mud) correspond exactly to the height of the second passageway, which probably plays the role of a water outfall. The origin of vertebrate remains is for the moment unknown (primary deposit or reworking of old fossiliferous deposits).

In relation to the speleothems, we observed that their location is highly variable from place to place in the cave but that, in most cases, they occur between the conglomerate and the sandy clays deposits. In this case, their deposition obviously took place after the phase of emptying the major part of the conglomerate/breccias and before the deposit of the clayey sediment. The thin mud layer that covers all of the other facies is the result of episodic flooding of the cave and represents the last known deposit.

1.2. Faunal description

The full faunal analysis from the Tam Hay Marklot fauna are presented here and in **Tab.S7**.

1.2.1. Artiodactyla

Within bovids, 115 teeth show the basic pattern of Caprinae, with smooth enamel, styles and stylids more prominent than main cusps, and no ectostylid. Dental dimensions allow the clear distinction of two taxa, one of large size close to the modern *Capricornis* species (*C. sumatraensis* or *C. milneedwardsi*), and a second one of small size close to the modern *Naemorhedus* species (*N. goral* or *N. caudatus*, the dimensions of *C. crispus* being intermediar (3)). We assign the Marklot specimens to *Capricornis* sp. and *Naemorhedus* cf. *caudatus* (P3 and P4 of square shape, metastyle well developed on M3). Dimensions of the large caprinae from Marklot (*Capricornis* sp.) are comparable to those of late Middle to Late Pleistocene specimens (3–9).

In relation to the large-sized bovids, it seems that at least two taxa occurred at Marklot. The main differences are observable on lower premolars and m3. On the first set of premolars, the main cuspids (hypoconid, entoconid, protoconid, and metaconid) appear well-developed buccolingually; the p2s are small mesiodistally and massive; on lingual side, we observe the presence of deep valleys between cuspids, and the enamel is often thick, all are features encountered in *Bos* species. Some m1/m2 exhibit rounded and voluminous metaconid and entoconid, and m3s a salient entostylid, which forms a deep notch with the hypoconulid. These features are close to the morphology observed in the modern *Bos frontalis* (being aware that *Bos* species may be easily confused on size and morphology). On another set of teeth, premolars are flatter and more elongated (with a range of variation showing no overlap with that of *Bos*), with shallow valleys and grooves between cuspids and a thinner enamel, as in *Bubalus bubalis* (synonym to *B. arnee*). We assign cautiously the teeth to *Bos* sp. (close to *Bos* cf. *frontalis)* (n = 37) and *Bubalus bubalis* (N=40), whereas 27 teeth remain difficult to identify.

The 287 suid specimens (277 permanent and 10 deciduous teeth) of Marklot show the typical morphological pattern of *Sus* (molar bunodont with bulky cusps and cuspids and numerous accessory tubercles, showing a star-like shape when worn). The teeth however display differences that suggest the presence of two distinct species. This is particularly observable on third molars (m3 and M3), and upper premolars (P4), whereas we were not able to detect clear differences on the other cheek teeth (except one m2 much elongated). The great majority of M3s display a high degree of variation with well-developed anterior cingulum with bulky folds, well-developed median accessory cusps, and main cusps sometimes duplicated. The morphology of the posterior portion of the crowns is complex, with a pentacone associated with numerous tubercles on the labial side. Likewise, for m3s, with a large pentaconid surrounded by numerous tubercles. On P4s, the cingulum is anteriorly and posteriorly developed and ended at the base of their crowns by two small cusps. We also observe the presence of a posterior sagittal couplet. This morphology is characteristic of *Sus scrofa*. A small number of teeth (m3 and M3) shows a different pattern: on M3, the anterior cingulum is thinner with a crenulated

enamel, the median cusp behind the first row (hyperpreconule) is few developed whereas the median cusp behind the second row is absent (pentapreconule); on m3s, the accessory median cusp behind the talonid is particularly small, a feature observed in *Sus barbatus* (10). On P4s, the cingulum is not marked and the cuplet is absent. Two taxa can be recorded at Marklot, *Sus scrofa* which includes most likely a great number of teeth, and *Sus* cf. *barbatus* only recognized on a small number of teeth (N=17). We didn't observe significant size differences between *S. scrofa* and *S. barbatus* at Marklot. Moreover, both species exhibit range variations comparable to those of modern species, rather than to those of the late Middle Pleistocene specimens (Khok Sung and Thum Wiman Nakin (3, 4) for *S. barbatus*, and Coc Muoi (8) for *S. scrofa*.

Numerous teeth exhibit the morphological pattern and dimensions of the large deer, *Rusa unicolor* (N=390): presence of an anterior fold on m1/m2, well-developed on m3; ectostylid always present on m1/m2; presence of a small anterior and, more rarely, posterior ectostylid on m3s; p4 molarized (11); salient cusps and styles on upper premolars; large paracone and metacone on upper molars. The Marklot species overlap in morphology and dimensions with the modern and late Middle to Late Pleistocene species.

The identification of middle-sized and small-sized cervids is more difficult due to the large overlap in dimensions and morphology (4). Within these cervids, some teeth are slightly larger with these characteristics: parastylid few developed on p2; a small anterior first valley on p3/p4; an entoconid as developed as the metaconid and entostylid; the entoconid and entostylid fused at the mid-height of the crown on p4; cones and conids of molars with a rounded shape; on m3s, large and rounded hypoconulid; parastyle more developed than the other styles on upper molars. All of these features are present in *Rucervus eldii* (N=27). Dimensions of the Marklot m3s, p3s/p4s, fall within the ranges of variation of the modern species (3). We also recognized a different taxon on the basis of a slightly smaller size and features close to the *Axis porcinus* pattern (N=22): parastylid well-developed forming a V-shaped valley with the paraconid; metaconid bilobed on p4s; entoconid and entostylid fused; V-shaped cones and conids on molars; on m3s, large and elongated hypoconulid. Specimens from the late Middle Pleistocene Thum Wiman Nakin site allocated to this species appear much greater (4).

Muntiacinae species also occur, which can be distinguished by the smallest dimensions of their teeth and the following features: few developed protoconid and parastylid oriented more anteriorly on lower premolars; few salient cones and conids on molars; upper molars with cone-shaped crowns; small styles on upper premolars and molars. The specimens remain however difficult to identify at the species level (*Muntiacus* sp.) (N=105). They are close in dimensions to the *Muntiacus* species of the Late Pleistocene Duoi U'Oi site (8), and to the modern *M. muntiacus grandicornis* measured by the authors at the Raffles museum in Singapore.

1.2.2. Perissodactyla

The rhinocerotid sample consists of 32 dental elements, which unambiguously document at least two extant species, namely the Javan rhinoceros, *Rhinoceros sondaicus* (N=10), and the Sumatran rhinoceros, *Dicerorhinus sumatrensis* (N=9), whereas 13 tooth fragments could not be identified at the genus or species levels and were accordingly referred to as Rhinocerotina indet.

Rhinoceros sondaicus is notably documented by a right D2 with a medifossette and a sharp parastyle sagittally oriented. A fragmentary P2 has an oblique cingular spur at the entrance of the lingual valley. A fragment of one M1 displays a thick hypocone, lacking a lingual groove. The fragmentary M3 has a thick paracone rib, vanishing well before the neck. The d4 fragment has a quadrangular occlusal outline. One p4 has a very thick labial enamel, an oblique cingular spur at the ectolophid groove, the latter being pointing mesiodorsally in lateral view. All of these features are characteristic of *R. sondaicus*, based on comparison with the dental material from individuals either recent (MNHN-AC)

or fossil (Punung locality, Java: Museum Naturalis of Leiden; Coc Muoi, Vietnam: Institute of Archaeology, Ha Noi).

Dicerorhinus sumatrensis is recognized thanks to the presence of a mesiolingual groove on the sagittally pinched hypocone of one fragmentary D4 and on permanent teeth (broken M2). A fragment of one M3, also with a sagittally pinched hypocone, shows a slightly convex ectometaloph in occlusal view, with a distolingual cingulum restricted to a small spur, further determining a shallow groove lingual to it. The complete d2 falls within the size range of *D. sumatrensis*. It is narrower than d2s referred to as *R. sondaicus*, with a shallow anterolabial groove and a posterior valley closed. Several fragmentary d3s and d4s have unconstricted metaconid and entoconid, and a distal border of the metalophid straight and oblique, which allows to assign them to *D. sumatrensis*. The labial fragment of m1 has a vertical ectolophid groove, reaching the neck. Together with small dimensions (especially regarding width), all of these features are considered as diagnostic based on comparison with dental material from individuals either recent (MNHN-AC; Cambridge Museum) or fossil (Sibrambang and Lida Ajer Caves, Sumatra; Museum Naturalis of Leiden).

Two teeth of tapir are also recorded at Marklot: one lower left canine (Tapiridae indet.), and one fragment of a jugal tooth (*Tapirus* sp.).

1.2.3. Carnivora

In relation to the Felidae, we recognized a small-sized felid on one m1 (a very simple morphology with two sharp blades) and five small canines (N=6). Within the sample of specimens belonging to large felids, several fragmentary large teeth (four P4, 2 p4, and one m1) and one complete upper I3 suggest the presence of *Panthera tigris* (N=7). Four other complete premolars (one P3, two P4, and one p4) exhibit the morphology and size of *Panthera pardus* (N=4), with dimensions falling in the range size of modern Asian *P. pardus* (taken by the authors at the Museum Naturalis in Leiden). The two P4 display well-developed cusps, one mesial in the line of blades and a second one oriented lingually. A sample of six fragmentary canines are assigned to large Carnivora.

Four complete, one fragmentary, and two heavily worn upper M1 belong to a small-sized melinae, a badger, most likely *Arctonyx* on the basis of morphology and size (hypocone elongated distally, lingual cusps well-developed). The dimensions of M1s (length: 14-16.2 mm; width: 10.2-11.1 mm) are particularly small, close to those of modern species of *Arctonyx: A. dictator* (measurements taken by the authors at the National History Museum, London, and *A. collaris collaris* (12), rather to that of Pleistocene specimens (13).

Four complete permanent teeth belong to a large-sized canidae. This sample shows however a great variation in teeth dimensions, with one large P4 falling within that of *Cuon javanicus antiquus* (12), one P3 and one m1 are small like in individuals from modern Asian populations, *C. a. adustus* (Myanmar), *C. a. sumatrensis* (Malaysia), *C. a. javanicus* (East Java) (measured by the authors at the National History Museum, London), whereas one very small M1 appears outside of the range of variation of modern and fossil populations.

Three ursids are present at Marklot: *Ursus thibetanus* has been identified based on 17 permanent teeth. The most striking characteristics are: presence of a lingual cusp on P4; outline of the M1 crown elongated with a weak cingulum; a large paracone and an elongated talonid on M2. Dimensions of the teeth are particularly great, in comparison with the other available but small modern and fossil samples (6–9, 12, 13). *Helarctos malayanus* is represented by 7 permanent teeth. The occlusal outline of the M2s is squarer with a less developed talonid. One M2 is particularly massive (10). One lower m2 is assigned to *Ailuropoda melanoleuca*. The tooth is smaller than those measured in a recent population (12).

1.2.4. Primates

Twenty-two permanent teeth conform to the morphology of the genus *Macaca* among Cercopithecidae. On the basis of the dimensions of upper molars, it seems that at least two species were present at Marklot. The large molars have the size of Late Pleistocene specimens (Duoi U'Oi, Tam Hang, and Lang Trang (6, 7, 13), close to the modern *M. nemestrina* or *M. mulatta* (data taken by the authors at the National History Museum, London; and *M. nemestrina*, *M. mulatta* or *M. arctoides* (14)), whereas a set of small teeth appear close to *M. fascicularis* (data taken by the authors at the National History Museum, London). O ther species are difficult to identify due to the large size overlap between taxa. Three *Pongo* teeth, two molars and one canine, are recorded, but these limited data preclude an assignment either to *Pongo pygmaeus* or to the Late Pleistocene *P. devosi* identified in China and Vietnam (15).

1.2.5. Rodentia

Only teeth of large-sized rodents belonging to Hystricidae are recorded at Marklot (N=151): 134 have the dimensions of the *Hystrix* species, whereas 17 smaller could be assigned to the genus *Atherurus*, most likely *A. macrourus*, the only species recorded in the Pleistocene of Southeast Asia. The length variations of upper (M1-M3) and lower (m1-m3) molars exceed largely those of modern *Hystrix* (*Acanthion*) *brachyura* s. l., and even those of the taller modern species *Hystrix* (*Hystrix*) *indica* (16). While falling in size closer to *H. indica*, we allocate the Marklot teeth cautiously to *Hystrix* sp.

1.3. Direct dating of Tam Hay Marklot fossil teeth

1.3.1. Material and methods

Samples

Four mammalian tooth samples of the Marklot assemblage discovered in 2015 and selected from the five samples exported in 2018 for direct dating (SCUMK-01, SCUMK-02, SCUMK-03A, SCUMK-03B and SCUMK-R1) were prepped for U-series dating and analysed at Southern Cross University and the University of Wollongong (**Tab.S8**).

U-series dating protocol and parameters

Teeth were cut to expose the different dental tissues using a low-speed saw with a rotating diamond blade of 300 µm thickness. Each section was then analyzed by quadrupole LA-ICP-MS for uranium distribution and with a Neptune Plus LA-MC-ICP-MS for uranium series measurements with the following setting: jet sample Ni 83506 and x skimmer Ni 76250 cones. The instrument was tuned with the NIST610 at 60% laser energy (2.49 J/cm^2), frequency 5 Hz, spot size 65 µm, scan speed of 5 µm/sec, He: 900 ml/min, N_2: 10 ml/min with obtained value of ^{238}U=1.28 V, ^{232}Th=1.05 V. Each sample was pre-ablated at 40% laser energy (3.3 J/cm^2), frequency 5 Hz, spot size 150 um, and scan speed of 200 um/sec, before conducting measurements of 310 µm rasters long at 80% laser energy (6.27 J/cm^2), frequency 20 Hz, spot size 150 µm, and scan speed of 5 µm/sec. For each sample between 9 and 10 rasters were drawn on the samples perpendicular to the growth axis of the tooth (from enamel tip to the pulp cavity). Each raster was analyzed twice consecutively and then data were averaged to obtain one minimum U-series age. Therefore, for each sample, we have calculated several minimum U-series ages (depending on the number of rasters and the data quality). Ages were not calculated when U concentration was below 1 ppm or when U/Th ratio was below 500. When values permitted, using the raster's sequence along the growth axis, a modelled U-series age was calculated using a Diffusion-Adsorption-Decay (DAD) model (17). Baseline and drifts were corrected using a NIST 612 glass disc, while two coral reference materials (the MIS 7 Faviid and MIS5 Porites corals from the Southern Cook Islands (18)) were used to correct ^{234}U/^{238}U and ^{230}Th/^{238}U ratios and assess the accuracy of measurements. Each coral reference material was analyzed by solution MC-ICPMS and used for reference. To account for potential matrix effects, a bovid tooth fragment from South Africa with known isotope concentrations was used to verify measurements. To account for tailing effects, measurements were carried out at half-masses of 229.5 and 230.5 for ^{230}Th and 233.5 and 234.5 for ^{234}U (19).

1.3.2. Results

The U-series dating results for SCUMK-01, SCUMK-02, SCUMK-03 and SCUMK-R1 are presented in **Tab.S9-S12**, and range between **37.4 ka +/- 0.9 and 13.1 ka +/- 0.5**.

1) The ages for SCUMK-R1 ranges between **37.0 ka +/- 1.5 and 25.0 ka +/- 0.9** with a mean age estimated at **31.2 ka +/- 1.3**.
2) The ages for SCUMK-01 ranges between **26.4.0 ka +/- 0.8 and 29.8 ka +/- 1.0** with a mean age estimated at **27.6 ka +/- 1.0**.
3) The ages for SCUMK-02 ranges between **37.0 ka +/- 1.3 and 39.1 ka +/- 1.4** with a mean age estimated at **37.4 ka +/- 0.9**.
4) The ages for SCUMK-03A ranges between **12.0 ka +/- 0.5 and 13.4 ka +/- 0.9** with a mean age estimated at **13.1 ka +/- 0.5**.

The $^{234}U/^{238}U$ ratio was consistent between the samples, except for sample SCUMK-01 which had slightly lower values. Despite the important difference in minimum age between SCUMK-03A (13 ka) and SCUMK-02 (37 ka) it does not appear to be a different diffusion environment and therefore the age discrepancy could only be an artefact of a later diffusion of U for SCUMK-03. Yet, because the distribution of U around the dental tissue in SCUMK-03A is rather uniform, it appears likely that the tooth represents a later deposition event than SCUMK-02.

In order to advance the dating accuracy, we have modelled each tooth using the DAD model (**Tab.S13 and FigS42-45**), which take into consideration the diffusion rate, the distance and size of each dental tissue and the diffusion pathway (17).

The difference between the mean U-series age and the model DAD age is within error the same and therefore indistinguishable (**Tab.S13**). The results show that the samples can be considered as closed system, and that the minimum ages obtained with the U-series are close to the 'true' age of the sample obtained by the DAD model. In other words, the results indicate that the teeth recovered from Tam Hay Marklot site have different ages.

1.4. General chronology and ecology of Marklot cave fauna

The mammalian faunal assemblage with the occurrence of modern taxa and the absence of archaic taxa (*Stegodon*, *Megatapirus*, or extinct rhinocerotid species), the dimensions of teeth close to those of the post-Middle Pleistocene taxa (species experienced overall trends of dental size decrease throughout the Pleistocene), and the dating, which show an age range of 38.4–13.5 ka, document a mammalian assemblage during a time period which encompasses the later section of the glacial stage MIS 3 through all MIS 2, including the Last Glacial Maximum (26.5–19 ka). Isotopic results suggest a mixed environment from closed low-light tropical rainforest to open savannah.

The dating of a tooth of orangutan (*Pongo* sp.) at 38.4 ka shows that during the periglacial MIS 3 period, at this latitude, the great ape still occupied closed, low-light tropical forests. In this mixed environment, the diet of the tiger (*Panthera tigris*) relied on prey species preferentially from open woodlands where they could find large-sized cervids and bovids, whereas diet of canids much more relied on forest-dwelling species. The diet of the other large predator, the leopard (*P. pardus*) relied on prey species from both ecosystems.

Supplementary Information 2: Stable isotope analysis

Stable isotope analysis is now a widely used method in archaeological and paleontological fields, yielding new insights into the past of animals and human alike (20–25). Although a large array of materials and tissues can be subjected to such analyses, dental enamel is of particular interest as it is metabolically inert after formation and is not very sensitive to post-mortem diagenesis and

alteration(26–29). It thus consists in an important material for palaeodietary and paleoenvironmental research (26, 30–32). However, enamel bioapatite (a biological carbonate-bearing hydroxylapatite) records the isotopic composition of the "whole" diet consumed and this only over the growth and mineralisation period of the teeth in animals (or hominins), thus representing a narrow subadult period (33, 34).

2.1. Variation of Zn stable isotope values in tooth enamel

Zinc is an element of Group 2B of the periodic table, the last column of the *d* block. While it is not a transition metal *per se*, it is sometimes included with them as its properties are more similar to these than to the post-transition metals. Zn possess five naturally occurring stable isotopes, ^{64}Zn (48.63%), ^{66}Zn (27.90%), ^{67}Zn (4.10%), ^{68}Zn (18.75%) (35), with an average relative atomic mass of 65.37777 (36).

Zn is a trace element but it is an important agent in many biological processes and is vital for most living organisms. Indeed, it has a reactive stability in a cellular environment governed by oxidation-reduction processes because of its single oxidation state (2+). Its ligands are multiples (37) and it is involved in all six enzyme classes and most of the regulatory proteins (38), as well as being involved in many biochemical functions (37).

In terrestrial context, the primary source of zinc in a given food web ultimately comes from the plants. Subsequently, two main parameters have been presented to explain the Zn isotope composition of plants: the initial Zn isotope ratios of the soil (39, 40) and the biological fractionation that occurs between the plant and the soil as well as within the plant itself during nutrient transport (39, 41–44).

The initial ^{66}Zn/^{64}Zn ratio (expressed as δ^{66}Zn value) of the soil is in turn controlled by the nature of the underlying bedrock. While igneous rocks exhibit a narrow and homogenous δ^{66}Zn values (+0.3 ± 0.14‰ (2σ)) (42, 45), sedimentary rocks exhibit a broader range of δ^{66}Zn values (45–47) with the highest values observed for marine carbonates (up to +1.4‰) (48, 49). In the case of Tam Hay Marklot cave, three major rock units are present at the local scale in the cave surrounding (see "***Supplementary Information 1: Context - 1.1.Geology***"): an exposed magmatic bedrock composed of granite, widespread arkosic sandstone and finally a sedimentary cover consisting of marine limestone. While δ^{66}Zn stable isotope analysis have not been conducted on any of these bedrocks, the limestone cover is likely to exhibit higher values than the other two. It is then reasonable to assume that local geology may impact local isotope ratios of the food web, thus possibly explaining some of the variability observed in enamel δ^{66}Zn values among the fossil teeth.

Within plants themselves, an initial fractionation occurs between the roots and the soil, during zinc uptake in the rhizosphere (41, 43). As a results, roots and shoots are generally enriched in heavy isotopes relative to the litter layer in which they grow (39, 41–43). Additionally, low δ^{66}Zn values are systematically observed the most aerial parts of the plants (39, 41, 42). It is believed that once the Zn is in the xylem, an active uptake of heavy isotopes by cells out of the xylem occurs during its transport, thus favoring the mobility of light isotopes to the most aerial parts of the plants (39, 42). As such, a correlation seems to exist between δ^{66}Zn in leaves and the length of the plants, both within a single plant and between species. Generally speaking, low growing plants such as herbaceous species are thus expected to have higher δ^{66}Zn values compared to high growing plants like trees (39, 41, 42).

Similar to plants, the isotopic composition of Zn in trophic chains' consumers (i.e. animal tissues) is governed by two factors: the initial Zn isotope ratios of the food products (plants in the case of herbivores and animals in the case of carnivores) and the isotopic fractionation occurring during intestinal absorption (50–56).

As it was the case for plants, in $\delta^{66}Zn$ values is prompted by the initial Zn isotopic composition of the foods consumed. For plant consumption, different species and parts, as well as difference in growth height, are all likely to induce different $\delta^{66}Zn$ values in the consumer. Similarly, the $\delta^{66}Zn$ values of body tissues resulting from meat consumption will depend on which parts and organ were consumed, with muscles usually being ^{66}Zn depleted relative to the average isotopic composition of the body (50, 53, 57, 58). It was suggested that biological activity fractionates Zn isotopes in the body among organs, thus explaining variability in body tissues (52, 53). Additionally, plant products usually have the most elevated $\delta^{66}Zn$ values (57, 58), whereas muscles exhibit low values (50, 53, 57, 58). Contrary to the classic trophic level tracer $\delta^{15}N_{collagen}$ values then, the higher the trophic level of an animal is, the lower are the Zn isotope ratios of its body tissues (50, 57–60).

2.2. Variation of strontium isotope ratios in tooth enamel

The geographical distribution of strontium isotopes is mostly determined by the evolution of ^{87}Sr in a geologic system. Contrary to the other strontium isotopes, ^{87}Sr is radiogenic, as a result from the radioactive decay of ^{87}Rb. The relative content and ratio of ^{87}Sr to ^{86}Sr is thus a function of both the age of the rock and original rubidium (Rb) amount of a given bedrock. This leads to a general trend of higher $^{87}Sr/^{86}Sr$ ratio in older rocks and lower values in younger rocks.

Strontium isotopes are widely used as geochemical signatures to “source” individuals (whether animals or humans) to a geologic area. This is because the $^{87}Sr/^{86}Sr$ ratio recorded in enamel is directly related to that of the diet and ultimately to that of the soils and water available to the plants, at the very base of the food web. The underlying concept is that the strontium isotopic signature is mostly preserved and carried from the eroding geologic bedrock to the soil (61) and then enters as bioavailable Sr into the plants (62). This signature is then preserved in its consumers, no matter the trophic level (i.e. from plants to herbivores and from herbivores to carnivores) (63). While there are additional non-geologic sources of variations in this $^{87}Sr/^{86}Sr$ ratio, an isotopic signature from specimens can then be associated with a biologically-available signature from a given location or region. This correlation between $^{87}Sr/^{86}Sr$ ratios within a food web with underlying geology signature was originally demonstrated in ecological studies (64–66) and quickly applied to archaeological context (67–69).

2.3. Variation of carbon and oxygen stable isotope values in tooth enamel

The carbon isotopic composition of bioapatite reflects that of diet, whereas the oxygen reflects mainly that of ingested water (20, 26, 30, 31, 70–73).

Reliance on food resources can be assessed through the existence of "isotopically" distinct resources in the environment. In tropical context, there exists an isotopic distinction in $\delta^{13}C$ values between plants using C_3 and C_4 photosynthetic pathways (74–76). The $\delta^{13}C$ values observed in studied faunal or hominin material thus convey the relative proportion of C_4 grassland and C_3 forest/woodland as carbon sources in their diet and, indirectly, to their associated environments (9, 77–80). C_3 plants predominate over the terrestrial vegetation biomass and are composed of trees, bushes, shrubs and grasses (74–76, 81). For the geographic area in this study, a $\delta^{13}C$ range of -37‰ to -23‰ is considered for C_3 plants, as higher values (>-23‰) are restricted to particular context and species (74, 75, 82). C_4 plants occur primarily in tropical and subtropical grassland and savanna regions, as well as in in temperate grassland regions in North and South America and Africa (81). They are mainly composed of grasses and sedges, and present higher $\delta^{13}C$ values of -17‰ to -10‰ (74, 75). It is noteworthy to mention that the terms C_3 and C_4 refer only to plant’s photosynthetic pathways. Technically, they are therefore strictly appropriate to describe the diet of herbivores. However, these terms will be used for all taxa in the present study to refer to an exploitation of resources provided from an environment dominated by either C_3 or C_4 plants, rather than a consumption of the plants themselves. Finally, the emission of burning fuel over the past 150 years has decreased the $\delta^{13}C$ of atmospheric CO_2, consequently influencing the $\delta^{13}C$ of all living organisms. As the $\delta^{13}C$ values of plants are based on modern samples, they must be corrected (~ 1.5‰) (83) when comparing with organisms that predate the atmospheric CO_2 shift due

to fossil fuel burning. Therefore, the upper $\delta^{13}C$ limit for C_3 used for the present study is shifted from -23‰ to -21.5‰, and the lower limit for C_4 plants from -17‰ to -15.5‰.

The diet's isotopic composition is then metabolized and incorporated into the tissues of animals (26). Trophic fractionation occurs when the food's carbon is metabolized and incorporated into the tissues of animals (bone collagen, enamel carbonate, hair, etc.), but is not homogenous and varies across animals (20, 26, 31, 73). No $\delta^{13}C$ diet-enamel spacing was thus applied to tooth enamel $\delta^{13}C_{apatite}$ values in this paper, because empirically determined diet-enamel ^{13}C enrichment factors (or closely related ones) are not determined for too many of the investigated fossil species. Thus, only $\delta^{13}C_{apatite}$ values are compared, which avoids the necessity of assumptions (however well-founded and logical) otherwise needed in order to assign diet-enamel $\delta^{13}C$ spacing to species with no such available data. However, this still enables to distinguish C_3 and C_4 plant-feeders

The oxygen isotopic composition ($\delta^{18}O$) of tooth enamel in homeothermic animals is regulated by that of body water, which consists of a complex combination of the effect of climate, diet, and physiology (71, 72, 84–88). Enamel oxygen isotope composition is nevertheless primarily controlled by the composition of drinking water and chemically-bound water in diet, i.e. free water found in plants (71, 72, 88–91). The isotopic composition of both of these is in turn mostly dependent on latitude and climate and temperature, moisture content, amount of precipitation and isotopic composition of precipitation (32, 71, 92). In tropical and subtropical regions, it has been shown that the $\delta^{18}O$ values of vegetation mostly reflect either evaporative potential or the source-effect of rainfall (93–95).

Carbon and oxygen isotope composition offer another insight into paleoenvironmental conditions in densely forested C_3 ecosystems through low values resulting from a "Canopy Effect" (96). The lowest $\delta^{18}O$ and $\delta^{13}C$ values are found in flora and fauna living on the forest floor (96–107) and can consequently be used as a tracer to infer the density of a forest cover. Additionally, $\delta^{18}O$ and $\delta^{13}C$ values from densely forested areas and ones that are more open will discriminate from one another with higher values associated with open settings (106–109).

2.4. Variation of nitrogen stable isotope values in collagen

Collagen-bound nitrogen isotope composition ($\delta^{15}N$) is usually 3 to 5‰ higher than dietary protein (23, 110, 111). This diet-consumer spacing can thus be used to assess the trophic level of an organism within a given food web, and particularly to identify the consumption of animal protein in the diet. Herbivores from terrestrial food web thus usually show $\delta^{15}N$ values 3 to 5‰ higher than the plants (i.e., 3 to 7‰), whereas carnivores will exhibit values, again, of 3 to 5‰ higher than their prey (i.e., 6 to 12‰). Omnivore's $\delta^{15}N$ values will usually fall between both ranges, according to the proportion of plant and animal proteins in their diet. However, the $\delta^{15}N$ values of plants is not homogeneous (112–114), which can lead to difference in absolute $\delta^{15}N$ values from one food web to another. Nevertheless, by comparing specimens from a wide range of diet (herbivores, omnivores and carnivores) for a given food web, it is possible to assign trophic level positions to specimens. The same trophic level effect can also be observed in aquatic ecosystems, but because many more steps usually take place in the food chain in aquatic ecosystems, $\delta^{15}N$ values of top-level consumers tend to be much higher (115).

Supplementary Information 3: Methods

3.1. Sample collection

The material used in this study consists of a selection of diverse taxa from the Tam Hay Marklot cave assemblage, covering a large range of distinct dietary habits. Each of the species' specific trophic ecology was assigned based on analogous modern-day fauna's dietary behaviors (116–119)A total of 72 teeth, belonging to 22 taxa, were selected for the present isotopic analysis. One to six specimens per species were used (**Tab.S1**). Within each taxon, the same type of tooth (ex: left p3) were selected to insure they belonged to different individuals. However, the same "right" and "left" teeth were sometimes selected but were considered to belong to distinct individuals based on different dental wear

stages. In addition to their original submitter number, each specimen was assigned an S-EVA code associated with samples prepared at the department of Human Evolution of the Max Planck Institute for Evolutionary Anthropology (Leipzig, Germany). Enamel was mechanically cleaned using a handheld drill equipped with a diamond-tipped burr to remove both adhering external material and a superficial layer of enamel. Subsequently, three different samples for each specimen was taken along the full height of the crown, using a either a diamond-tip cutting wheel or diamond-tipped burr: 4.8 to 23.5 mg (average 10.5 mg ± 7.3 mg (2σ)) for Zn isotope analysis (a minimum of 5 mg is recommended for the analysis), 9.4 to 25.8 mg for Sr isotope analysis and 4.1 to 13.7 mg for C and O isotope analysis. The varying amount of material collected was due to differences in relative thickness of the enamel, the height of the crown and the overall aspect of the teeth.

3.2. Zinc analytical technique

Enamel samples were digested in 1 ml of HCl 1.0 N, then evaporated and dissolved again in HBr 1.5 N. Zn was then purified in two steps the modified ion exchange method adapted from Moynier et al. (2006) (120), first described in Jaouen et al. (2016) (57). Zn was purified in pre-conditioned microcolumns on 1 ml AG-1x8 resin (200-400 dry mesh size, 106-180 μm wet bead size) using 2 ml of HBr 1.5 N for matrix residue elution and 5 ml of HNO_3 0.5 N for Zn elution. Samples were then dried and re-dissolved in 1 ml HNO_3 0.5 N. Every preparation batch of 13 samples included at least one reference material (in-house reference material AZE bone powder and/or the NIST SRM 1400 bone ash) and a blank in order to assess the quality of the column chromatography purification. These replicate measurements allow to correct values of the enamel samples run at the same time, while also controlling the precision of the mass spectrometer (2σ (AZE) = 0.08‰; 2σ (NIST SRM 1400) = 0.06‰). Zinc isotopic ratios were measured using the protocol of Toutain et al. (2008) (121) and Cu doping, on a Thermo Neptune Multi-collector ICP-MS at the Max Planck Institute for Evolutionary Anthropology (Leipzig, Germany). The dentine and sediment samples were measured on a Thermo Neptune Plus Multi-collector ICP-MS atthe "Observatoire Midi Pyrénées" (Toulouse, France). The in-house standard Zn AA-MPI was used for standard bracketing. Isotopic ratios were expressed relative to the international standard JMC-Lyon. Isotopic abundances are presented in δ (delta) notation expressed as deviation per mil (‰), as follows: $\delta^{66}Zn = ({}^{66}Zn/{}^{64}Zn_{sample}/{}^{66}Zn/{}^{64}Zn_{standard} - 1) \times 1000$. Repeated analysis (n=89) of almost every specimen were also performed to determine the homogeneity of the enamel samples. The overall average analytical repeatability for these fossil samples was ±0.04‰ (2σ) (**Tab.S3**). Following a protocol adapted from the one used for Sr by Copeland et al. (2008) (122) and first used in Jaouen et al. (2016) (59), regression equation based on the ^{64}Zn signal intensity (V) of three solutions with known concentrations (150, 300 and 600 ppb) were used to estimate the Zn concentrations of samples. The accuracy of these obtained Zn concentration was evaluated through the known concentration of international reference material NIST SRM 1400 (bone ash) and deemed accurate (expected Zn concentration = 181 ± 6 ppm (2σ); measured Zn concentration 190 ± 19.4 ppm (2σ)).

3.3. Strontium analytical technique

Sample preparation used a modified method of Copeland et al. (2008) (122), as presented in Britton et al. (2009) (123). Enamel samples were digested in 2 ml of HNO_3 14.3 N, then evaporated and dissolved in 1 ml HNO_3 3.0 N. Samples are then loaded into 1 ml of pre-conditioned microcolumns containing Sr-spec™ resin (50-100 μm particle size). Matrix residues were eluted with 1.2 ml HNO_3 3 N and strontium was eluted from the resin with 1.5 ml ultrapure deionized water (18.2 MΩ), dried and then re-dissolved in 2 ml HNO_3 0.5 N. Every preparation batch of 10 samples included at least one reference material (NIST SRM 1486 bone meal) and a blank in order to assess the quality of the column chromatography purification. Analysis of $^{87}Sr/^{86}Sr$ ratios were measured using a Thermo Scientific Neptune Multi-collector ICP-MS at the Max Planck Institute for Evolutionary Anthropology. All $^{87}Sr/^{86}Sr$ measurements were corrected for interferences from rubidium (Rb) and normalized for instrumental mass bias to $^{88}Sr/^{86}Sr = 8.375209$ (exponential law). External normalization of data was achieved with analysis of the international strontium isotope reference material NIST SRM 987 during

each analytical session ($^{87}Sr/^{86}Sr$ value = 0.7102957 ± 0.000021 (2σ) (n = 58)). All $^{87}Sr/^{86}Sr$ values reported here were adjusted so SRM987 = 0.710240 (124), with a correction offset of + 0.000056 (n = 58). Strontium concentrations of the enamel samples were determined through regression equation based on the ^{88}Sr signal intensity (V) of three solutions with known concentrations (100, 400 and 700 ppb), using the method described in Copeland et al. (2008) (122).

3.4. Carbonate carbon and oxygen isotope analytical technique

Each sample were soaked in a 1 ml of 0.1 M acetic acid (CH_3COOH) solution for four hours at room temperature, rinsed three times in distilled water and then dried overnight at 65 °C. Stable carbon and oxygen isotopic composition of every samples were analyzed using a Thermo Scientific Delta V Advantage isotopic mass spectrometer coupled to a Thermo Scientific Kiel IV Carbonate Device chemical preparer, at the "Service de Spectrométrie de Masse Isotopique du Muséum (SSMIM)" in Paris. Isotopic abundances are presented in δ (delta) notation expressed as deviation per mil (‰), as follows: $\delta^{13}C = (^{13}C/^{12}C_{sample}/^{13}C/^{12}C_{standard} - 1) \times 1000$ and $\delta^{18}O = (^{18}O/^{16}O_{sample}/^{18}O/^{16}O_{standard} - 1) \times 1000$. Analyses of an internal laboratory reference material (Marble LM) normalized to the International Atomic Energy Agency reference material (NBS-19) (**Tab.S5**) were performed alongside fossil samples during every mass spectrometer run. These replicate measurements allow to correct values of the carbonate enamel samples run at the same time, while also controlling the precision of the mass spectrometer (2σ ($\delta^{13}C$) = 0.06‰; 2σ ($\delta^{18}O$) = 0.12‰).

3.5. Collagen carbon and nitrogen isotope analytical technique

A selection of specimens (n=23) from various taxon (n=16) was also taken to assess the preservation of organic material. Because most teeth from the assemblage show various degrees of porcupine gnawing of their roots, only 23 out of the 72 specimens had sufficient dentin material for such analysis. The root of the teeth was cleaned with a sandblaster using Korox® 50 (50 µm) 99.6% aluminum oxide sand. Samples were obtained by using a handheld drill equipped with a diamond-tip cutting wheel, where 198.2 to 677.5 mg of material was taken from the root area. Sample preparation for collagen extraction followed the protocol first described in Talamo and Richard (2011) (125). Samples were demineralized with HCl 0.5 N while refrigerated for several days (until no effervescence was observed), then rinsed with deionized water. NaOH 0.1 N was then added for 30 minutes to remove humics, followed by an HCl 0.5 N step for 15 minutes, with deionized water rinses after both steps. Following Longin's protocol (1971) (126), samples are gelatinized at pH 3 in a heater block at 75 °C for 20 h, and then filtered (Eeze-Filter™, Elkay Laboratory Products (UK) Ltd.), to remove small particles (<80 µm), and ultrafiltered (Sartorius "Vivaspin Turbo" 30 KDa ultrafilters). Finally, samples were lyophilized for 48 h (~ -28 °C). The preservation of the collagen was assessed for the samples with a sufficient yield by evaluating C:N (between 2.9 and 3.6) ratios, %C, %N, collagen yield (ideally not less than 1% of weight) and $\delta^{13}C$ and $\delta^{15}N$ values (127, 128). Stable isotope analysis was conducted using a Thermo Finnigan Flash EA coupled to a Delta V isotope ratio mass spectrometer. $\delta^{13}C$ values are measured relative to the V-PDB standard and $\delta^{15}N$ values are measured relative to the AIR standard.

3.6. Spatial element concentration profiles analytical technique

Spatial element concentration profiles were conducted on six fossils specimens (Tam Hay Marklot cave, Laos) and three modern ones (Center of Natural History of Hamburg, originally zoo animals from Hagenbeck Tierpark in Hamburg). Each tooth was sectioned longitudinally along bucco-lingual axis using an Isomet low speed saw (Bühler, Lake Bluff, US). In order to obtain a plane surface, the resulting surface of each tooth was then polished using an Ecomet 4000 variable speed grinder-polisher (Bühler, Lake Bluff, US), with Carbimet grit 360 [P600] (Bühler, Lake Bluff, US) paper. The measurement routines were performed with a Thermo Element2 single collector sector-field ICP-MS coupled with a New Wave UP213 Nd:YAG laser ablation system at the Max Planck Institute for Chemistry, Mainz. Spot analysis with laser beam size of 80 µm and a pulse repetition rate of 10 Hz was performed, in a line scan analysis at a speed of 10 µm/s after a preablation with 80 µm/s. Fluence (energy density) during the experiments was 13 J cm^{-2}. Concentration of the following 36 selected isotopes were

measured in the same run: Na^{23}, Mg^{25}, Al^{27}, Si^{29}, P^{31}, K^{39}, Ca^{43}, Mn^{55}, Fe^{57}, Cu^{63}, Zn^{66}, Zn^{67}, Zn^{68}, Rb^{85}, Sr^{86}, Sr^{88}, Cs^{133}, Ba^{137}, Ba^{138}, La^{139}, Ce^{140}, Pr^{141}, Nd^{143}, Sm^{147}, Eu^{151}, Gd^{157}, Tb^{159}, Dy^{161}, Ho^{165}, Er^{167}, Tm^{169}, Yb^{173}, Lu^{175}, Pb^{208}, Th^{232} and U^{238}. The synthetic glass NIST SRM 612 (n = 6) was used to calibrate element concentrations (129). Each monitored isotope was normalized to ^{43}Ca as the internal standard. During each LA-ICP-MS sequence, the accuracy and precision of the analysis was assessed by measuring ca. 160 μm long line scans on a pressed powder pellet of NIST SRM 1400.

3.7. Statistical analysis

To test our hypotheses, analyses were performed using the statistical program R (version 3.6.1) (130). Our response variable was $\delta^{66}Zn$ values and the tested predictors, associated with each $\delta^{66}Zn$ value were diet (carnivore, omnivore and herbivore), taxon, $\delta^{13}C$ values, $\delta^{18}O$ values, $^{87}Sr/^{86}Sr$ isotope ratios, Zn concentration, and the average body mass for that specific species. We fitted a Linear Mixed Model (LMMs) (131) with a Gaussian error structure and identity link (132) using the R-package "lme4" (version 1.1-17) (133). All quantitative predictors were inspected for whether they were roughly symmetrically distributed and were, when they showed to have a skewed distribution (Body mass and Zn concentration), log-transformed. In order to ease model convergence and achieve comparability of estimates, all quantitative predictors were subsequently z-transformed (to a mean of zero and a standard deviation of one). We included all predictors as fixed effects with the exception of taxon, which we included as a random intercepts effect. Furthermore, to keep type I error rate at the nominal level of 0.05 we included random slopes of $\delta^{13}C$, $\delta^{18}O$, $^{87}Sr/^{86}Sr$, and Zn concentration within taxon but no parameters for the correlations among random slopes and intercepts (134, 135). Collinearity among predictors was assessed using the function vif of the R-package "car" (136) applied to a standard linear model, excluding the random effect, was low (maximum of squared n^{th} root of Generalized Variance Inflation Factors, with n being twice the degrees of freedom of the respective predictor: 1.56). To assess model stability, we compared model estimates obtained from the full dataset with those obtained when excluding levels of the random effect (taxa) and as well as specimens, one at a time. This revealed model stability to be good. We checked whether the assumptions of normally distributed and homogeneous residuals were fulfilled by visual inspection of a QQ-plot (137) of the residuals and residuals plotted against fitted values, which revealed no obvious violations of these assumptions. In order to test the significance of the key test predictors, $^{87}Sr/^{86}Sr$ and body mass, we compared the full model with a null model lacking these two terms to avoid multiple testing (138). For this we used a likelihood ratio test, approximated using a *chi*-square distribution (139). We also tested the significance of individual fixed effect predictors using likelihood ratio tests comparing the full model and with models dropping predictors one at a time. We determined confidence intervals of model estimates by means of a parametric bootstrap (function bootMer of the package "lme4") utilizing 1,000 bootstraps. The sample size for the model was 69 specimens from 22 taxa, since three specimens could not be sampled for $^{87}Sr/^{86}Sr$ analysis.

Supplementary Information 4: Results

4.1 Zn stable isotope values ($\delta^{66}Zn$) in fossil tooth enamel from Tam Hay Marklot cave

The zinc isotopic composition of the 72 studied tooth enamel specimens from the Tam Hay Marklot fauna are presented here and in **Tab.S3**.

When every taxon and every diet category are considered, $\delta^{66}Zn$ values range from -0.04‰ (*Hystrix* sp.) to 1.03‰ (*Bos* sp.), with an average of 0.52‰ (± 0.54‰ (2σ)). Herbivores (n = 41; mean$\delta^{66}Zn$ = 0.68‰ ± 0.38‰ (2σ)) exhibit $\delta^{66}Zn$ values ranging from 0.29‰ (*Muntiacus* sp.) to 1.03‰ (*Bos* sp.), carnivores (n = 9; mean$\delta^{66}Zn$ = 0.09‰ ± 0.24‰ (2σ)) from -0.01‰ (*Panthera tigris*) to 0.34‰ (Canidae) and omnivores (n = 22; mean$\delta^{66}Zn$ = 0.41‰ ± 0.54‰ (2σ)) from -0.04‰ (*Hystrix* sp.) to 0.72‰ (*Sus* sp.).

Rhinoceros sondaicus (n = 5) exhibit the largest range of variation in $\delta^{66}Zn$ values (0.51‰) and *Ursus thibetanus* (n = 3) the smallest (0.05‰), with an average range throughout all different taxa of 0.27‰.

When the mean intraspecific $\delta^{66}Zn$ ranges of variation of each taxon are taken together, omnivores exhibit the largest one (0.30‰), followed by herbivores (0.28‰) and then finally carnivores (0.15‰). It is also noteworthy to mention that the range of variation in $\delta^{66}Zn$ values of herbivores taxa is increased by that of *Rhinoceros sondaicus*, itself influenced by a single outlier. If this outlier were to be ignored, the range of variation observed in herbivores taxa $\delta^{66}Zn$ would decrease to 0.25‰.

The overall range of $\delta^{66}Zn$ values for each broad diet category, as well as their taxon intraspecific variations, is in agreement with dietary habits. Indeed, omnivorous taxa (which diets can consist of various proportion of meat, eggs, insects, grubs, fruits, roots, tubers, leaves, stems, bark, etc.) exhibit the largest range and variability of $\delta^{66}Zn$ values. They display $\delta^{66}Zn$ values ranging from those associated with carnivorous taxa to those of strict herbivorous, with the bulk however consisting of intermediate values between carnivores and herbivores. This in turn most likely results from a varying proportion of meat in the diet. Herbivorous taxa range of $\delta^{66}Zn$ values, albeit smaller than that of omnivores, is also coherent with expectations. Values are generally higher and the relatively large range in $\delta^{66}Zn$ values is consistent with intake from different plants and plant parts (i.e. fruits, roots, tubers, leaves, stems, bark, etc.). Finally, carnivore taxa exhibit the lowest $\delta^{66}Zn$ values and the smallest range of variation, both being in agreement with a diet limited to meat consumption.

Additionally, sediment (n =5) and dentin samples (n = 13, from 7 specimens) and were analyzed for $\delta^{66}Zn$ values (**Tab.S14**) in order to assess the trend of post-mortem diagenesis alteration.

The $\delta^{66}Zn_{dentin}$ values range from 0.39‰ to 1.05‰ (**Tab.S14 and Fig.S40-42**). The offset observed between $\delta^{66}Zn_{dentin}$ and $\delta^{66}Zn_{enamel}$ is +0.22‰ ± 0.26‰ (2σ) (**Fig.S40**), which is agreement with $\delta^{66}Zn$ values obtained from modern fauna at Kobi Fora ($\Delta\delta^{66}Zn_{bone\text{-}enamel} \approx +0.2$‰) (57). Additionally, the trophic levels difference can still be observed, with carnivore having the lowest $\delta^{66}Zn$ values. The $\delta^{66}Zn_{sediment}$ values range from 0.12‰ to 0.69‰ (**Tab.S14**). The clay sample exhibits the lowest $\delta^{66}Zn$ value, as can be expected from a usually silicate-rich mineral, and the highest $\delta^{66}Zn$ value is found in the cemented fossil-bearing layer.

When $\delta^{66}Zn$ values from both sediments and dentin samples are compared with their respective Zn concentration (**Fig.S42**), no obvious trend could be observed. Thus, no clear post-mortem diagenesis alteration in dentin $\delta^{66}Zn$ values and Zn concentration can be observed.

4.2 Sr radiogenic isotope ratios ($^{87}Sr/^{86}Sr$) in fossil tooth enamel from Tam Hay Marklot cave

The radiogenic strontium isotope ratios ($^{87}Sr/^{86}Sr$) of 69 specimens from the Tam Hay Marklot fauna are presented here and in **Tab.S3 and Fig.S10-11**. Only 69 specimens out of 72 were analyzed, as not enough material was available from three specimens.

The $^{87}Sr/^{86}Sr$ ratios range from 0.7097 (*Hystrix* sp.) to 0.7243 (*Helarctos malayanus*), with an average of 0.7154 ± 0.0062 (2σ). The majority of the specimens falls within a range of $^{87}Sr/^{86}Sr$ ratios from 0.7135 (1st Qu.) to 0.7173 (3rd Qu.). *Axis* cf. *porcinus* (n = 2) exhibit the smallest intraspecific variation in $^{87}Sr/^{86}Sr$ isotope (0.0001) and *Helarctos malayanus* (n = 2) display the largest (0.0122 ± 0.0172 (2σ)), while the average variation observed for each taxon is of 0.0044 ± 0.006 (2σ).

No bioavailable strontium isotope ratios are available for the studied region and no local plants were analyzed in the current study. Description of the bedrocks geology is nonetheless available (1) and reported in "***Supplementary Information 1: Context - 1.1.Geology***". Three major units are identified in the surrounding area of the Tam Hay Marklot cave: Palaeozoic granite basement, a widespread Silurian light metamorphic sedimentary formation composed primarily of arkosic sandstone and finally a thick limestone unit attributed to an interval between the Late Carboniferous (Moscovian) and the

Permian (1). Considering the local geology of Tam Hay Marklot cave's region, it could be expected that the granite exhibits higher $^{87}Sr/^{86}Sr$ isotope than the other two the sedimentary substratum. Accordingly, the granite would also be expected to display lower $\delta^{66}Zn$ values than both sedimentary rock formations (45–49).

The preservation of pristine radiogenic strontium isotope ratios was investigated through a mixing line between Sr concentration and $^{87}Sr/^{86}Sr$ ratios (**Fig.S11**). The absence of any significant post-mortem Sr uptake was corroborated by the absence of relation between the two variables, as well as by the Sr concentrations also fall within the range of modern specimens (**Fig.S11**).

4.3 Carbon ($\delta^{13}C$) and oxygen ($\delta^{18}O$) stable isotope values in fossil tooth enamel from Tam Hay Marklot cave

The carbon and oxygen isotopic composition of the 72 studied specimens from the Tam Hay Marklot cave fauna are presented here and in **Tab.S3 and Fig.S8**.

Among the 22 taxa present in the sample, the $\delta^{13}C_{apatite}$ values range from -16.7‰ (*Ailuropoda melanoleuca*) to +2.4‰ (*Rucervus eldii*), with a mean $\delta^{13}C$ value of -10.11‰ (± 10.64‰ (2σ)). Herbivores (n = 41) present values -16.2‰ (*Rhinoceros sondaicus*) to +2.4‰ (*Rucervus eldii*), carnivores (n = 9) between -16.0‰ (Canidae (?*Cuon alpinus*)) and -4.0‰ (*Panthera pardus*) and omnivores (n = 22) between -15.4‰ (*Ursus thibetanus*) and -6.0‰ (*Sus* sp.). The majority of the specimens (65%, n = 47) display $\delta^{13}C_{apatite}$ values that reflect a C_3 diet ($\delta^{13}C_{apatite}$ < -8‰), with a moderate amount (25%, n = 18) showing a mixed C_3/C_4 diet (-8‰ > $\delta^{13}C_{apatite}$ < -2‰), and only few (10%, n = 7) being associated with a strict C_4 diet ($\delta^{13}C_{apatite}$ > -2‰). Large bovids (*Bos* sp., *Bubalus bubalis*) and *Panthera pardus* exhibit the largest variations in $\delta^{13}C$ values (respectively $\Delta^{13}C$ 14.1‰, 11.9‰ and 9.8‰) and *Helarctos malayanus*, *Axis* cf. *porcinus* and *Rucervus eldii* exhibits the smallest ones (respectively $\Delta^{13}C$ 0.2‰, 0.2‰ and 0.6‰). The average overall variation is 4.3‰ and the median 2.6‰.

The $\delta^{13}C_{apatite}$ values of -14.0‰ or lower result from a strong canopy effect, thus representative of a mesic closed low-light tropical rainforest (31, 80, 108, 109, 140–143), with arelatively high proportion (30%, n = 22) of specimens from Tam Hay Marklot cave being associated with these values . All three dietary categories (carnivores, omnivores and herbivores) are represented, for a total of 12 different taxa. *Rhinoceros sondaicus* (n = 5), in particular, is well represented in this ecoregion, with only a single specimen falling out of the aforementioned range of $\delta^{13}C_{apatite}$ values. Higher $\delta^{13}C_{apatite}$ values, between -14‰ and -8‰, consist of diets reflecting a reliance on mostly C_3 environment resources. It encompasses a similar proportion of specimens (35%, n = 25) to those associated with a strong canopy effect, and present the highest diversity in species (14/22 taxa). However, these C_3 associated $\delta^{13}C_{apatite}$ values can reflect either a mixed dietary reliance from closed forest and open woodlands (77, 108, 109, 142, 144) or a reliance on strictly mesic forest environment (80, 108, 109, 145). In the case of Tam Hay Marklot cave, the latter case seems the most coherent. Indeed, taxa associated with $\delta^{13}C_{apatite}$ values between -14.0‰ and -8.0‰, most notably but not restricted to *Pongo* sp. (orangutan), support the presence of a forest habitat, albeit probably not as dense as that of a closed low-light tropical rainforest. A natural break in the $\delta^{13}C_{apatite}$ values can also be observed around -10.0‰Finally, the highest end of $\delta^{13}C_{apatite}$ values encompass values reflecting mixed C_3-C_4 resources reliance (from -8.0‰ to -2.0‰) and strict C_4 plant-feeder (i.e. grazer)values (> -2.0‰). A fairly significant number of specimens (35%, n = 25) and taxa from Tam Hay Marklot (10/22) once again present such values. Such values cover a wide array of ecoregions going from mixed forest, to C_3 xeric woodland to C_3-C_4 "savannah" environment. While it can be difficult to define a clear limit between these various different ecoregions, they nonetheless all consist of open settings of varying degree.

The oxygen isotopic compositions of Tam Hay Marklot fauna vary from -10.0‰ (*Sus* sp.) to 0.2‰ (*Naemorhedus* cf. *caudatus*), with an average $\delta^{18}O_{apatite}$ values -5.7‰ (± 3.54‰ (2σ)). Herbivores

display values of -7.6‰ (*Capricornis* sp.) to -4.2‰ (*Bos* sp.), carnivores from -7.3‰ (*Panthera pardus* and Canidae (?*Cuon alpinus*)) to -3.2‰ (Canidae (?*Cuon alpinus*)) and omnivores from -10.0‰ (*Sus* sp.) to -4.1‰ (*Pongo* sp.). The average variation seen within taxa is 2.6‰ and the median 2.8‰. Contrary to expectations, the taxa that exhibit the largest variation in their $\delta^{18}O_{apatite}$ values were not systematically those that showed large variation in their $\delta^{13}C$ values as well.

4.4 Carbon ($\delta^{13}C$) and nitrogen ($\delta^{15}N$) stable isotope values in fossil teeth root dentin from Tam Hay Marklot cave

A sub-sample of 23 specimens, from 16 different taxa, were processed for collagen extraction to assess the preservation of organic material. The preservation of the collagen was assessed for the samples with a sufficient yield by evaluating C:N (between 2.9 and 3.6) ratios, %C, %N, collagen yield (not less than 1% of weight) and $\delta^{13}C$ and $\delta^{15}N$ values (127, 128). The collagen-bound stable carbon and nitrogen isotopic composition of the four specimens that yielded collagen are presented here and in **Tab.S4 and Fig.S9**.

Individuals with the highest to the lowest $\delta^{15}N_{collagen}$ are: *Muntiacus* sp. (10.56‰), *Sus* sp. (8.07‰), *Rhinoceros sondaicus* (6.63‰) and *Bos* sp. (3.15‰). The associated $\delta^{13}C_{collagen}$ values are -21.0‰, -21.7‰, -24.0‰ and -9.1‰, respectively.

The low $\delta^{15}N_{collagen}$ value of *Bos* sp. can be explained by the fact that the food resources consumed by this specimen come from a C_4 environment, and thus more open and dry than that associated with the other three specimens (112). Its trophic level is nevertheless consistent with a herbivorous diet (23, 24, 110, 111). The $\delta^{15}N_{collagen}$ value of the *Sus* sp. specimen, when compared to herbivorous *Rhinoceros sondaicus* specimen, is consistent to that of an omnivorous diet, as it is higher (+1.49‰) but not by a full trophic level (23, 110, 111). *Muntiacus* sp. exhibits the highest $\delta^{15}N_{collagen}$, which is almost a trophic level higher (+2.49‰) than that of *Sus* sp. and a full trophic level higher than that of *Rhinoceros sondaicus* (+3.93‰). This is surprising given that even an omnivorous diet is debated for the muntjac. While some studies suggest that they exhibit omnivores habits (146, 147), others show that it is not the case (119, 148, 149). At the very least, a full trophic level above herbivores, and slightly higher than that of *Sus* sp., is unexpected.

The $\delta^{13}C_{collagen}$ values are consistent with those ranging from mammals feeding in a C_4 open environment to a closed low-light tropical rainforest. They also mirror the $\delta^{13}C_{apatite}$ values obtained for the same specimens. A fairly constant $\delta^{13}C_{apatite\text{-}collagen}$ spacing (from 7.8 to 8.8‰; 8.2 ± 1.0‰ (2σ)) can also be observed and is slightly larger than expected spacings, especially for omnivores (26, 30, 73, 150).

4.5. Spatial element concentration profiles

Spatial element concentration profiles analysis was carried on (*Capricornis* sp., *Ursus thibetanus*, *Panthera pardus*, *Sus* sp. and *Macaca* sp.) and three modern teeth (*Bison bison*, *Hemitragus jemlahicus* and *Pteronura brasiliensis*) of various feeding behaviors (carnivorous, omnivorous and herbivorous). From the 36 selected isotopes measured, sets of spatial element concentration profiles are provided in **Fig.S12-S29** for the following elements: zinc [Zn], iron [Fe], manganese [Mn], aluminum [Al], magnesium [Mg], strontium [Sr], REE (rare earth elements, calculated as the sum of all measured REE concentrations) lead [Pb] and uranium [U].

Elements such Fe, Mn and Al and were used as diagenetic tracer because their ionic radius is close to that of Zn, making them more likely to share similar behaviors, and consequently to be altered in similar ways (151). In addition, REE, Pb and U were used to assess the presence of diagenesis in a broader sense. Indeed, because their ionic radius differs widely to that of Zn, they behave in a very different way and are not a reliable specific diagenesis tracer for elements such as Zn (152).

Similar concentrations and undisturbed distribution profiles of these elements were observed almost systematically across modern and fossil enamel samples, while in contrast the dentin and pulp cavity in fossil teeth displayed increase or decrease of these elements indicating diagenetic alteration. A total of 23 enamel cross section segments were analyzed over the 15 analysis conducted on the 6 fossil specimens. Only one, from the *Panthera pardus* specimen, showed Zn concentration distribution that deviates from pattern found in modern teeth. However, this was only observed for one of the cross-section segments analyzed on this specimen.

Supplementary Tables

Table S1

Taxon	SEVA	#ref	Diet[1,2,3,4]	Element
Capricornis sp.	34489	MI-20	Herbivore	m3 inf. right
Capricornis sp.	34490	MI-21	Herbivore	m3 inf. right
Capricornis sp.	34491	MI-22	Herbivore	m3 inf. right
Capricornis sp.	34492	MI-23	Herbivore	m3 inf. right
Capricornis sp.	34493	MI-24	Herbivore	m3 inf. right
Naemorhedus cf. *caudatus*	34494	MI-25	Herbivore	m3 inf. left
Naemorhedus cf. *caudatus*	34495	MI-26	Herbivore	m3 inf. left
Naemorhedus cf. *caudatus*	34496	MI-27	Herbivore	m3 inf. left
Naemorhedus cf. *caudatus*	34497	MI-28	Herbivore	m3 inf. left
Helarctos malayanus	34498	MI-103	Omnivore	M2 sup. left
Helarctos malayanus	34499	MI-121	Omnivore	M2 sup. left
Ursus thibetanus	34500	MI-117	Omnivore	M2 sup. right
Ursus thibetanus	34501	MI-119	Omnivore	M2 sup. left
Ursus thibetanus	34502	MI-122	Omnivore	M2 sup. left
Panthera pardus	34503	MI-134	Carnivore	P3 sup. right
Panthera pardus	34504	MI-135	Carnivore	p4 inf. left
Panthera pardus	34505	MI-136	Carnivore	P4 sup. left
Rusa unicolor	34506	MI-166	Herbivore	m3 inf. left
Rusa unicolor	34507	MI-180	Herbivore	m3 inf. left
Rusa unicolor	34508	MI-185	Herbivore	m3 inf. left
Rusa unicolor	34509	MI-187	Herbivore	m3 inf. left
Rusa unicolor	34510	MI-191	Herbivore	m3 inf. left
Rucervus eldii	34511	MI-512	Herbivore	m3 inf. left
Rucervus eldii	34512	MI-595	Herbivore	m3 inf. left
Axis cf. *porcinus*	34513	MI-556	Herbivore	m3 inf. left
Axis cf. *porcinus*	34514	MI-557	Herbivore	m3 inf. left
Muntiacus sp.	34515	MI-627	Herbivore	m3 inf. right
Muntiacus sp.	34516	MI-628	Herbivore	m3 inf. right
Muntiacus sp.	34517	MI-629	Herbivore	m3 inf. right
Muntiacus sp.	34518	MI-630	Herbivore	m3 inf. right
Muntiacus sp.	34519	MI-631	Herbivore	m3 inf. right
Bubalus bubalis	34520	MI-650	Herbivore	p2 (p3?) inf. right
Bubalus bubalis	34521	MI-651	Herbivore	p2 (p3?) inf. right
Bubalus bubalis	34522	MI-652	Herbivore	p2 (p3?) inf. left
Bubalus bubalis	34523	MI-653	Herbivore	p2 (p3?) inf. left
Bubalus bubalis	34524	MI-654	Herbivore	p2 (p3?) inf. left
Bos sp.	34525	MI-655	Herbivore	p2 inf. right
Bos sp.	34526	MI-656	Herbivore	p2 inf. right
Bos sp.	34527	MI-657	Herbivore	p2 inf. right
Bos sp.	34528	MI-658	Herbivore	p2 inf. left
Bos sp.	34529	MI-659	Herbivore	p2 inf. left
Panthera tigris	34530	MI-130	Carnivore	frag. p4 inf.right
Panthera tigris	34531	MI-693	Carnivore	frag. P4 sup. left

Panthera tigris	34532	MI-694	Carnivore	frag. P4 sup. left
Sus sp.	34533	MI-662	Omnivore	p4 inf. left
Sus sp.	34534	MI-663	Omnivore	p4 inf. left
Sus sp.	34535	MI-664	Omnivore	p4 inf. left
Sus sp.	34536	MI-665	Omnivore	p4 inf. left
Sus sp.	34537	MI-666	Omnivore	p4 inf. left
Sus sp.	34538	MI-667	Omnivore	p4 inf. left
Canidae (?*Cuon alpinus*)	34539	MI-131	Carnivore	m1 inf. right
Canidae (?*Cuon alpinus*)	34540	MI-681	Carnivore	P3 sup. right
Canidae	34543	MI-682	Carnivore	M1 sup. left
Pongo sp.	34541	MI-683	Omnivore	Canine
Pongo sp.	34542	MI-685	Omnivore	M sup. left
Ailuropoda melanoleuca	34544	MI-684	Herbivore	m2 inf. right
Tapiridae indet.	34545	MI-691	Herbivore	canine inf. left
Tapirus sp.	34546	MI-692	Herbivore	frag. dent jugale
Macaca sp.	34547	MI-695	Omnivore	m1/m2 inf. left
Macaca sp.	34548	MI-696	Omnivore	m1/m2 inf. left
Macaca sp.	34549	MI-697	Omnivore	pm inf. right
Macaca sp.	34550	MI-698	Omnivore	m1/m2 inf. left
Macaca sp.	34551	MI-699	Omnivore	pm inf. right
Hystrix sp.	34552	MI-700	Omnivore	incisor
Hystrix sp.	34553	MI-701	Omnivore	incisor
Hystrix sp.	34554	MI-702	Omnivore	incisor
Hystrix sp.	34555	MI-703	Omnivore	incisor
Rhinoceros sondaicus	34556	MI-686	Herbivore	m3 inf. left
Rhinoceros sondaicus	34557	MI-687	Herbivore	m3 inf. left
Rhinoceros sondaicus	34558	MI-688	Herbivore	m2 inf. left
Rhinoceros sondaicus	34559	MI-689	Herbivore	d3 inf. left
Rhinoceros sondaicus	34560	MI-690	Herbivore	d3 inf. right

Full list of fossil tooth specimens from Tam Hay Marklot cave (Laos) analyzed in this study, with corresponding S-EVA number, original number, broad dietary category and anatomical element. The dietary category assigned to each taxon was taken from [(1)]Nowak 1999, [(2)]Macdonals 2009 and [(3-4)]Johnsingh and Manjrekar 2013, 2015 (116–119).

Table S2

Sample	Sample matrix	SEVA	$\delta^{66}Zn$
Sandy to gravelly silty clays (fossil-bearing layer)	Sediment	35342	0.60
Calcitic cementation (fossil-bearing layer)	Sediment	35343	0.69
Clay from conglomerate	Sediment	35344	0.12
Conglomerate/breccias	Sediment	35345	0.53
Sediment attached to the enamel surface of sample 34556 (*Rhinoceros sondaicus*)	Sediment	34556-D_9	0.55
Rhinoceros sondaicus	Dentin	34556-D_1	0.65
Rhinoceros sondaicus	Dentin	34556-D_2	0.77
Rhinoceros sondaicus	Dentin	34556-D_3	0.82
Rhinoceros sondaicus	Dentin	34556-D_4	0.73
Rhinoceros sondaicus	Dentin	34556-D_7	0.71
Rhinoceros sondaicus	Dentin	34556-D_10	0.65
Rhinoceros sondaicus	Dentin	34556-D_mean	0.72
Capricornis sp.	Dentin	34489-D	0.81
Capricornis sp.	Dentin	34490-D	1.05
Capricornis sp.	Dentin	34492-D	0.99
Helarctos malayanus	Dentin	34498-D	0.73
Panthera pardus	Dentin	34505-D	0.39
Bubalus bubalus	Dentin	34524-D	0.85

Sediment and dentin $\delta^{66}Zn$ isotope values from Tam Hay Marklot cave (Laos) used to assess the impact of diagenesis on $\delta^{66}Zn$ values.

3 Table S3

Taxon	**SEVA**	**Diet**	**$\delta^{13}C$**	**$\delta^{18}O$**	**$^{87}Sr/^{86}Sr$**	**$\delta^{66}Zn\_1$**	**$\delta^{66}Zn\_2$**	**$\delta^{66}Zn\_3$**	**$\delta^{66}Zn$ mean**	**$\delta^{66}Zn$ 2 σ**
Capricornis sp.	34489	Herbivore	-13.4	-2.2	0.7136	0.52	0.53	0.51	0.52	0.02
Capricornis sp.	34490	Herbivore	-14.7	-5.2	0.7098	0.79	0.81	0.82	0.81	0.03
Capricornis sp.	34491	Herbivore	-15.2	-5.2	0.7112	0.64	0.68	0.69	0.67	0.05
Capricornis sp.	34492	Herbivore	-13.5	-7	0.7148	0.60	0.61	0.62	0.61	0.02
Capricornis sp.	34493	Herbivore	-14.6	-7.6	0.7148	0.80	0.76	0.78	0.78	0.04
Naemorhedus cf. *caudatus*	34494	Herbivore	-2.4	+0.2	0.7103	0.86	0.86	0.86	0.86	0.00
Naemorhedus cf. *caudatus*	34495	Herbivore	-3.9	-2.5	0.7109	0.91	0.90	0.90	0.90	0.01
Naemorhedus cf. *caudatus*	34496	Herbivore	-3.7	-1.8	0.7105	1.03	0.97	0.97	0.99	0.07
Naemorhedus cf. *caudatus*	34497	Herbivore	-2.5	-1.6	0.7123	0.76	0.77		0.76	0.01
Helarctos malayanus	34498	Omnivore	-14.7	-3.9	0.7121	0.68	0.67		0.67	0.01
Helarctos malayanus	34499	Omnivore	-14.9	-5.5	0.7243	0.25	0.22		0.24	0.04
Ursus thibetanus	34500	Omnivore	-15.4	-7.4	0.7166	0.44	0.43	0.41	0.43	0.03
Ursus thibetanus	34501	Omnivore	-13.3	-6.6	0.7188	0.38	0.36		0.37	0.03
Ursus thibetanus	34502	Omnivore	-14.4	-6.3	0.7177	0.40	0.38	0.39	0.39	0.02
Panthera pardus	34503	Carnivore	-7.9	-7.3	0.7135	-0.02	-0.03	0.02	-0.01	0.05
Panthera pardus	34504	Carnivore	-4.0	-7.3	0.7113	0.00	0.02	0.00	0.01	0.02
Panthera pardus	34505	Carnivore	-13.8	-6.8		0.10	0.07	0.09	0.08	0.03
Rusa unicolor	34506	Herbivore	-7.5	-5.7	0.7159	0.49	0.45		0.47	0.06
Rusa unicolor	34507	Herbivore	-5.3	-4.4	0.7149	0.50			0.50	
Rusa unicolor	34508	Herbivore	-6	-4.9	0.7185	0.47			0.47	
Rusa unicolor	34509	Herbivore	-3.4	-4.9	0.7117	0.85	0.74	0.76	0.78	0.12
Rusa unicolor	34510	Herbivore	-7.9	-6.1	0.7147	0.61			0.61	
Rucervus eldii	34511	Herbivore	+2.4	-5.3	0.7144	0.56	0.55		0.55	0.01
Rucervus eldii	34512	Herbivore	+1.8	-3.1	0.7140	0.72	0.70		0.71	0.03
Axis cf. *porcinus*	34513	Herbivore	-0.8	-5.8	0.7117	0.75	0.69		0.72	0.08
Axis cf. *porcinus*	34514	Herbivore	-0.6	-5.3	0.7118	0.62			0.62	
Muntiacus sp.	34515	Herbivore	-13.8	-7.4	0.7160	0.62	0.57		0.60	0.07
Muntiacus sp.	34516	Herbivore	-14.8	-8.1	0.7174	0.47	0.46		0.47	0.01

Muntiacus sp.	34517	Herbivore	-12.7	-8.1	0.7195	0.22	0.36		0.29	0.20
Muntiacus sp.	34518	Herbivore	-14.4	-5	0.7163	0.46	0.43	0.47	0.46	0.04
Muntiacus sp.	34519	Herbivore	-14.5	-7.5	0.7158	0.66	0.64	0.64	0.64	0.02
Bubalus bubalis	34520	Herbivore	-10.3	-6.0	0.7151	0.59			0.59	
Bubalus bubalis	34521	Herbivore	-4.0	-6.6		0.53	0.46		0.50	0.10
Bubalus bubalis	34522	Herbivore	+1.0	-4.7		0.66	0.60		0.63	0.08
Bubalus bubalis	34523	Herbivore	-10.9	-6.3	0.7159	0.62	0.49	0.53	0.55	0.13
Bubalus bubalis	34524	Herbivore	+0.1	-5.9	0.7139	0.81	0.81	0.80	0.81	0.01
Bos sp.	34525	Herbivore	-2.5	-4.2	0.7160	0.75			0.75	
Bos sp.	34526	Herbivore	-14.4	-6.1	0.7165	0.95			0.95	
Bos sp.	34527	Herbivore	-0.3	-4.6	0.7173	0.77			0.77	
Bos sp.	34528	Herbivore	-10.0	-7.6	0.7156	1.02	1.03	1.03	1.03	0.01
Bos sp.	34529	Herbivore	-13.1	-5.9	0.7154	0.96	1.00	0.96	0.98	0.05
Panthera tigris	34530	Carnivore	-4.3	-3.2	0.7126	-0.03	0.04	-0.05	-0.01	0.09
Panthera tigris	34531	Carnivore	-6.9	-3.5	0.7147	0.03	0.09	0.04	0.05	0.06
Panthera tigris	34532	Carnivore	-10.0	-6.8	0.7170	0.14	0.20	0.14	0.16	0.07
Sus sp.	34533	Omnivore	-7.6	-7.5	0.7149	0.72	0.70	0.69	0.70	0.03
Sus sp.	34534	Omnivore	-8.6	-10	0.7210	0.48	0.52	0.51	0.50	0.04
Sus sp.	34535	Omnivore	-6.0	-5.9	0.7168	0.73	0.73	0.70	0.72	0.03
Sus sp.	34536	Omnivore	-13.5	-5.8	0.7181	0.62	0.58	0.63	0.61	0.05
Sus sp.	34537	Omnivore	-14.0	-7.6	0.7154	0.37	0.26		0.32	0.16
Sus sp.	34538	Omnivore	-13.2	-5.4	0.7202	0.64	0.58	0.61	0.61	0.06
Canidae (?*Cuon alpinus*)	34539	Carnivore	-16.0	-7.3	0.7205	0.05	-0.01		0.02	0.08
Canidae (?*Cuon alpinus*)	34540	Carnivore	-11.4	-3.2		0.23	0.18		0.20	0.07
Canidae	34543	Carnivore	-13.2	-6		0.60	0.61		0.60	0.01
Pongo sp.	34541	Omnivore	-14.8	-4.1	0.7159	0.38			0.38	
Pongo sp.	34542	Omnivore	-13.5	-4.6	0.7103	0.33	0.35	0.33	0.34	0.02
Ailuropoda melanoleuca	34544	Herbivore	-16.7	-6.3	0.7121	0.52	0.53		0.53	0.01
Tapiridae indet.	34545	Herbivore	-15.5	-5.9	0.7211	0.51	0.48		0.50	0.04
Tapirus sp.	34546	Herbivore	-11.3	-7.9	0.7200	0.41	0.37		0.39	0.06

Macaca sp.	34547	Omnivore	-13.9	-5.3	0.7158	0.21	0.22		0.22	0.01
Macaca sp.	34548	Omnivore	-14.2	-5.3	0.7178	0.12	0.15	0.18	0.15	0.06
Macaca sp.	34549	Omnivore	-15.1	-5.6	0.7182	0.35	0.36		0.35	0.01
Macaca sp.	34550	Omnivore	-13.3	-4.7	0.7166	0.30	0.29		0.30	0.01
Macaca sp.	34551	Omnivore	-12.9	-4.6	0.7107	0.29	0.34		0.32	0.07
Hystrix sp.	34552	Omnivore	-11.5	-7.6	0.7134	0.42	0.41	0.42	0.42	0.01
Hystrix sp.	34553	Omnivore	-11.5	-5.5	0.7147	0.31	0.27		0.29	0.06
Hystrix sp.	34554	Omnivore	-7.9	-5.2	0.7097	0.45	0.42	0.44	0.43	0.03
Hystrix sp.	34555	Omnivore	-11.6	-8.5	0.7168	-0.01	-0.04	-0.08	-0.04	0.07
Rhinoceros sondaicus	34556	Herbivore	-16.2	-6.5	0.7199	0.51	0.52		0.52	0.01
Rhinoceros sondaicus	34557	Herbivore	-13.3	-5.5	0.7173	0.86			0.86	
Rhinoceros sondaicus	34558	Herbivore	-15.6	-6.3	0.7156	0.90			0.90	
Rhinoceros sondaicus	34559	Herbivore	-15.3	-7.1	0.7186	0.83	0.75		0.79	0.11
Rhinoceros sondaicus	34560	Herbivore	-14.6	-7.5	0.7150	1.03			1.03	

Enamel stable isotope results of $\delta^{13}C_{apatite}$, $\delta^{18}O_{apatite}$, $^{87}Sr/^{86}Sr$ and $\delta^{66}Zn$ from the 72 fossil tooth specimens from Tam Hay Marklot cave (Laos).

Table S4

Identifier	Taxon	% Coll	$\delta^{13}C_{collagen}$	$\delta^{15}N_{collagen}$	%C	%N	C:N ratio
SEVA 34517	*Muntiacus* sp.	0.70	-21.03	+10.56	43.97	15.86	3.23
SEVA 34527	*Bos* sp.	0.59	-9.15	+3.15	44.29	15.92	3.25
SEVA 34537	*Sus* sp.	0.37	-21.68	+8.07	34.72	12.54	3.23
SEVA 34556	*Rhinoceros sondaicus*	0.17	-24.04	+6.63	40.92	14.39	3.32

Dentin $\delta^{13}C$ and $\delta^{15}N$ values from collagen extraction for the four of the 23 of the sub sample of 23 dentin samples, for which collagen extraction was attempted.

Table S5

Reference material	Element	Substance	Measured value (‰)	SD	n	Expected value (‰)	SD
Marbre-LM(1) (theoretical value normalized to NBS-19)	C&O	Carbonate (in house)	+2.17‰ ($\delta^{13}C$) −2.00‰ ($\delta^{18}O$)	0.05 0.03	24	+2.13‰ ($\delta^{13}C$) −1.83‰ ($\delta^{18}O$)	NA
EVA-0009 Methionine(2)	C&N	Methionine (in house)	-28.28 ($\delta^{13}C$) -4.88 ($\delta^{15}N$)	0.09 0.26	7	-28.28‰ ($\delta^{13}C$) -4.98‰ ($\delta^{15}N$)	NA
IAEA-N-1 (153–156)	N	Ammonium Sulfate	+0.43 ($\delta^{15}N$)	N/A	1	+0.40‰ ($\delta^{15}N$)	0.2
IAEA-CH-6 (153, 157)	C	Sucrose	-10.31 ($\delta^{13}C$)	N/A	1	-10.449‰ ($\delta^{13}C$)	0.033
IAEA-N-2 (153–156)	N	Ammonium Sulfate	+20.31 ($\delta^{15}N$)	N/A	1	+20.30‰ ($\delta^{15}N$)	0.2
IAEA-CH-7 (153, 157)	C	Polyethylene foil	-31.74 ($\delta^{13}C$)	N/A	1	-32.151‰ ($\delta^{13}C$)	0.05
NIST SRM 1577b(2)	C&N	Bovine liver	-21.24 ($\delta^{13}C$) +7.61 ($\delta^{15}N$)	0.04 0.04	2	-21.40‰ ($\delta^{13}C$) 7.60‰ ($\delta^{15}N$)	NA
NIST SRM 1486 (60)	Sr	Bone meal	0.709306 ($^{87}Sr/^{86}Sr$)	0.000026	7	0.709299	0.000027
AZE (60)	Zn	Dentin (in house)	+1.59 ($\delta^{66}Zn$)	0.04	11	+1.50 ($\delta^{66}Zn$)	0.1
NIST SRM 1400 (60)	Zn	Bone ash	+0.95 ($\delta^{66}Zn$)	0.03	6	+1.0 ($\delta^{66}Zn$)	0.04

(1) Expected values obtained through in-house long-term measurements at the "Service de Spectrométrie de Masse Isotopique du Muséum (SSMIM)" in Paris.
(2) Expected values obtained through in-house long-term measurements at the Max Planck Institute for Evolutionary Anthropology, in Leipzig.

List of reference materials with their respective measured and expected values for different isotopes.
Table S6

	Est.	SE	LowerCI	UpperCI	X^2	Df	*P*	Min	Max
Intercept	0.074	0.078	-0.086	0.230			-	0.008	0.135
Diet (1)	NA	NA			23.289	2	0.000		
dietHerbivore	0.523	0.088	0.340	0.701				0.461	0.582
dietOmnivore	0.441	0.095	0.249	0.633				0.384	0.520
$^{87}Sr/^{86}Sr$ (2)	-0.097	0.023	-0.144	-0.050	12.101	1	0.001	-0.109	-0.079
$\delta^{13}C_{apatite}$ (3)	-0.008	0.023	-0.058	0.041	0.230	1	0.632	-0.043	-0.005
$\delta^{18}O_{apatite}$ (4)	0.006	0.027	-0.051	0.063	0.135	1	0.713	-0.005	0.030
Zinc concentration (5)	-0.050	0.036	-0.133	0.031	2.163	1	0.141	-0.101	0.002
Body mass (6)	0.116	0.035	0.047	0.187	9.892	1	0.002	0.095	0.143

(1) Dummy coded with carnivores being the reference category
(2) z-transformed to a mean of 0 and a standard deviation of 1; whereas the original mean and sd were 0.7154 and 0.0031 $^{87}Sr/^{86}Sr$, respectively
(3) z-transformed to a mean of 0 and a standard deviation of 1; whereas the original mean and sd were -9.99‰ and 5.4‰ $\delta^{13}C_{apatite}$, respectively
(4) z-transformed to a mean of 0 and a standard deviation of 1; whereas the original mean and sd were -5.71‰ and 1.78‰ $\delta^{18}O_{apatite}$, respectively
(5) z-transformed to a mean of 0 and a standard deviation of 1; whereas the original mean and sd were 114.32 and 140.35 ppm, respectively (before log-transformed)
(6) z-transformed to a mean of 0 and a standard deviation of 1; whereas the original mean and sd were 330.51 and 497.07 kg, respectively (before natural log-transformed)

Results of the Linear Mixed Model modelling $\delta^{66}Zn$ values as a function of several predictors (estimates and standard errors, confidence limits of the model, results of likelihood ratio tests, and the range of estimates obtained for the model when dropping levels of random effects one at a time).

Table S7

Taxa	Permanent teeth	Deciduous teeth	Total
Artiodactyla			
Rusa unicolor	367	23	390
Rucervus eldii	17	10	27
Axis cf. *porcinus*	18	4	22
Muntiacus sp.	101	4	105
Middle-sized Cervidae	29	1	30
Bos sp. (*Bos* cf. *frontalis*)	37	-	37
Bubalus bubalis	40	-	40
Large-sized Bovidae (*Bos*/*Bubalus*)	27	7	34
Capricornis sp. (*Capricornis* cf. *sumatrensis*)	83	-	83
Naemorhedus cf. *caudatus*	32	-	32
Sus sp. (S. *scrofa*/*S. barbatus*)	264	10	274
Sus cf. *barbatus*	17	-	17
Proboscidea			
Elephas sp.	-	1	1
Perissodactyla			
Rhinoceros sondaicus	7	3	10
Dicerorhinus sumatrensis	4	5	9
Rhinocerotina indet.	≥7	≥4	13
Tapiridae indet.	1	-	1
Tapirus sp.	1	-	1
Carnivora			
Canidae (?*Cuon alpinus*)	4	-	4
Panthera pardus	4	-	4
Panthera tigris	7	-	7
Small-sized Felidae	6	-	6
Large Carnivora	6	-	6
Ursus thibetanus	17	-	17
Helarctos malayanus	7	-	7
Ursidae indet. (*U. thibetanus*/*H. malayanus*)	5	-	5
Small-sized melinae (*Arctonyx* sp.)	7	-	7
Ailuropoda melanoleuca	1	-	1
Primates		-	
Macaca sp.	22	-	22
Pongo sp.	3	-	3
Rodentia		-	
Hystrix sp.	134	-	134
Atherurus cf. *macrourus*	17	-	17
		-	
Total (NISP)	**1292**	**72**	**1364**

Inventory of specimens (isolated teeth) of mammals recovered at the Marklot site. N: Total number of specimens.

Table S8

Sample name	Field number	Taxon	Tooth type
SCUMK-01	1092	Large bovid (*Bos*/*Bubalus*)	M_1 or M_2
SCUMK-02	3	*Pongo* sp.	R-M_1
SCUMK-03A	1003	*Bos* cf. *frontalis*	R-P_3
SCUMK-03B	1005	*Bos* cf. *frontalis*	R-P_3
SCUMK-R1	1058	*Dicerorhinus sumatrensis*	L-P_3

Sample description from fossil teeth of the Tam hay Marklot assemblage prepared for U-series dating.

Table S9

Sample	U	U/Th	$^{230}Th/^{238}U$	2s-error	$^{234}U/^{238}U$	2s-error	Age (ka)	2s-error
SCUMKR1_1	-0.02	0	-5.3000	5.3000	1.4600	0.5300		
SCUMKR1_2	-0.12	-1473	0.5270	0.0340	1.4710	0.0300		
SCUMKR1_3	-0.12	1192	0.4990	0.0410	1.4590	0.0100		
SCUMKR1_4	-0.12	315	0.4960	0.0570	1.4480	0.0120		
SCUMKR1_5	-0.11	463	0.4780	0.0560	1.5110	0.0270		
SCUMKR1_6	3.46	20353	0.3880	0.0140	1.4880	0.0110	**37.0**	**1.5**
SCUMKR1_7	3.68	26286	0.3582	0.0090	1.4770	0.0120	**35.0**	**1.5**
SCUMKR1_8	5.10	25500	0.3320	0.0140	1.4790	0.0120	**32.0**	**1.6**
SCUMKR1_9	6.21	51750	0.2653	0.0057	1.4651	0.0081	**25.0**	**0.9**
SCUMKR1_10	5.98	-31474	0.2866	0.0079	1.4660	0.0110	**27.0**	**1.1**
SCUMKR1 mean age							**31.2**	**1.3**

U-series results for the Tam Hay Marklot tooth specimen SCUMKR1 (*Dicerorhinus sumatrensis*).

Table S10

Sample	U	U/Th	$^{230}Th/^{238}U$	2s-error	$^{234}U/^{238}U$	2s-error	Age (ka)	2s-error
SCUMK01_1	-0.01	-1	-0.1000	2.0000	0.4400	0.7600		
SCUMK01_2	-0.07	-84	1.3000	1.2000	1.9000	0.7000		
SCUMK01_3	-0.07	-1470	0.5900	0.1600	1.4610	0.0920		
SCUMK01_4	0.61	-6100	0.1120	0.0560	1.4130	0.0510		
SCUMK01_5	9.73	57235	0.2738	0.0049	1.4014	0.0062	**26.9**	0.6
SCUMK01_6	12.13	8308	0.2914	0.0063	1.3987	0.0089	**27.7**	0.9
SCUMK01_7	10.47	7027	0.2840	0.0120	1.4000	0.0110	**27.5**	1.7
SCUMK01_8	10.74	3556	0.2732	0.0057	1.3981	0.0069	**26.4**	0.8
SCUMK01_9	7.90	600	0.3110	0.0100	1.3640	0.0150	**29.8**	1.0
SCUMK01 mean age							**27.6**	1.0

U-series results for the Tam Hay Marklot tooth specimen SCUMK01 (large bovid).

Table S11

Sample	U	U/Th	$^{230}Th/^{238}U$	2s-error	$^{234}U/^{238}U$	2s-error	Age (ka)	2s-error
SCUMK02_1	-0.12	293	0.5400	0.0110	1.4518	0.0065		
SCUMK02_2	-0.12	-2306	0.5340	0.0350	1.4580	0.0120		
SCUMK02_3	6.70	-26800	0.3803	0.0081	1.4680	0.0077	**37.2**	1.1
SCUMK02_4	12.50	-113636	0.4160	0.0270	1.4729	0.0092	**37.2**	0.9
SCUMK02_5	16.01	53367	0.3889	0.0055	1.4730	0.0048	**37.2**	0.5
SCUMK02_6	16.47	1647000	0.3872	0.0042	1.4717	0.0051	**37.3**	0.6
SCUMK02_7	16.03	320600	0.3884	0.0050	1.4706	0.0061	**37.0**	1.3
SCUMK02_8	17.73	1773000	0.3870	0.0100	1.4714	0.0084	**39.1**	1.4
SCUMK02_9	17.28	7714	0.3906	0.0069	1.4730	0.0067	**37.3**	0.8
SCUMK02_10	17.10	13680	0.3929	0.0061	1.4718	0.0064	**37.4**	0.7
SCUMK02 mean age							**37.4**	**0.9**

U-series results for the Tam Hay Marklot tooth specimen SCUMK02 (*Pongo* sp.).

Table S12

Sample	U	U/Th	$^{230}Th/^{238}U$	2s-error	$^{234}U/^{238}U$	2s-error	Age (ka)	2s-error
SCUMK03_1	-0.03	-32	0.1700	0.2000	0.9300	0.3800		
SCUMK03_2	0.11	335	0.1360	0.0610	1.5000	0.1300		
SCUMK03_3	4.42	19217	0.1443	0.0049	1.4360	0.0130	**13.1**	0.5
SCUMK03_4	5.30	589	0.1392	0.0080	1.4240	0.0300	**12.0**	0.5
SCUMK03_5	5.10	9273	0.1482	0.0050	1.4430	0.0082	**13.4**	0.5
SCUMK03_6	5.16	5864	0.1475	0.0043	1.4358	0.0092	**13.4**	0.4
SCUMK03_7	4.70	1382	0.1477	0.0055	1.4465	0.0093	**13.3**	0.5
SCUMK03_8	4.20	592	0.1465	0.0049	1.4270	0.0110	**13.4**	0.5
SCUMK03_9	3.87	2037	0.1473	0.0091	1.4430	0.0140	**13.4**	0.9
SCUMK03A mean age							**13.1**	0.5

U-series results for the Tam Hay Marklot tooth specimen SCUMK03 (*Bos* sp. (*Bos* cf. *frontalis*)).

Table S13

Sample	Mean Age U-series (ka)	Number of rasters	Age DAD (ka)	2s-Error
SCUMK-R1	31.2ka+/-1.3	5	**31.4**	**+2.9/-2.7**
SCUMK-01	27.6ka+/-1.0	7	**28.1**	**+1.2/-1.2**
SCUMK-02	37.4ka+/-0.9	8	**38.4**	**+1.0/-1.2**
SCUMK-03A	13.1ka+/-0.5	7	**13.5**	**+1.0/-1.0**

DAD model results for each fossil tooth sample from the Tam Hay Marklot assemblage prepared for U-series dating.

Table S14

Sample	Sample matrix	SEVA	$\delta^{66}Zn$
Sandy to gravelly silty clays (fossil-bearing layer)	Sediment	35342	0.60
Calcitic cementation (fossil-bearing layer)	Sediment	35343	0.69
Clay from conglomerate	Sediment	35344	0.12
Conglomerate/breccias	Sediment	35345	0.53
Sediment attached to the enamel surface of sample 34556 (*Rhinoceros sondaicus*)	Sediment	34556-D_9	0.55
Rhinoceros sondaicus	Dentin	34556-D_1	0.65
Rhinoceros sondaicus	Dentin	34556-D_2	0.77
Rhinoceros sondaicus	Dentin	34556-D_3	0.82
Rhinoceros sondaicus	Dentin	34556-D_4	0.73
Rhinoceros sondaicus	Dentin	34556-D_7	0.71
Rhinoceros sondaicus	Dentin	34556-D_10	0.65
Rhinoceros sondaicus	Dentin	34556-D_mean	0.72
Capricornis sp.	Dentin	34489-D	0.81
Capricornis sp.	Dentin	34490-D	1.05
Capricornis sp.	Dentin	34492-D	0.99
Helarctos malayanus	Dentin	34498-D	0.73
Panthera pardus	Dentin	34505-D	0.39
Bubalus bubalus	Dentin	34524-D	0.85

Sediment and dentin $\delta^{66}Zn$ isotope values from Tam Hay Marklot cave (Laos) used to assess the impact of diagenesis on $\delta^{66}Zn$ values.

Supplementary Figures

Figure S1

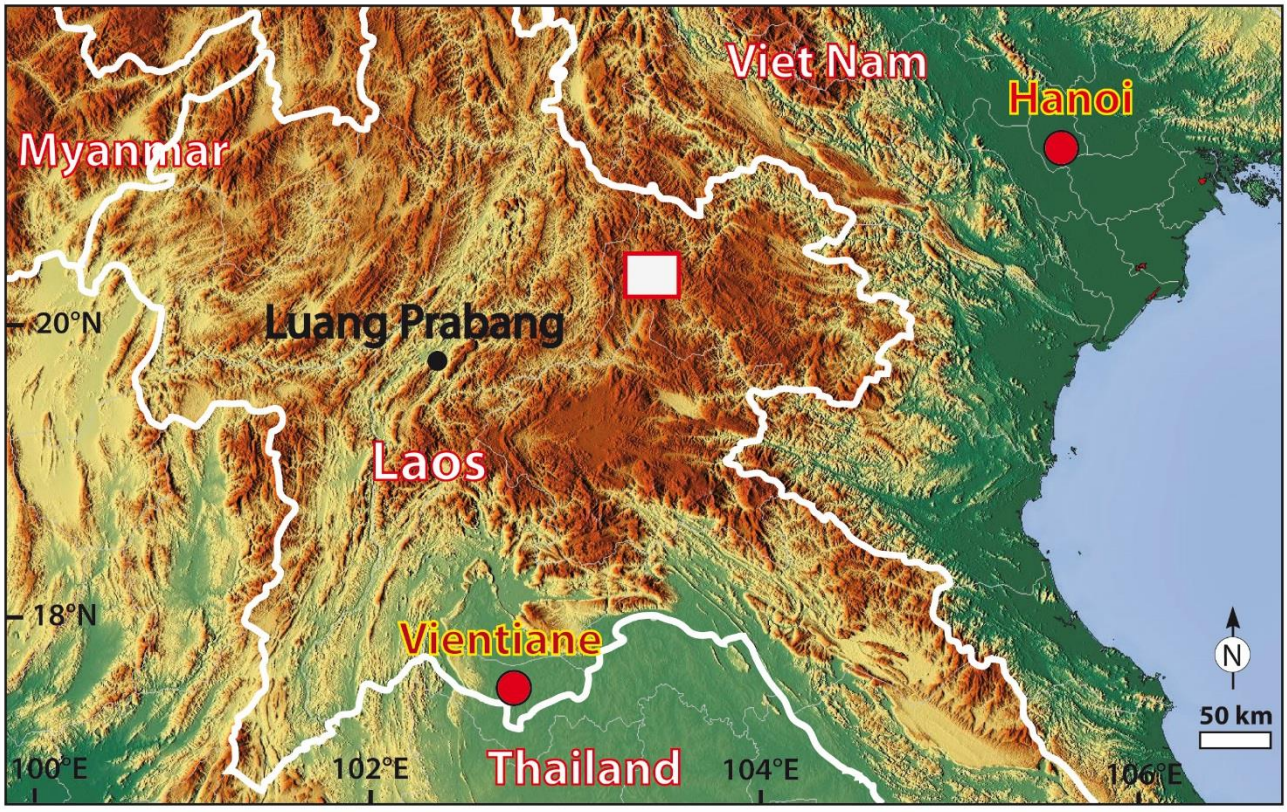

Map of the Indochinese Peninsula with the location of the studied area in northeast Laos.

Figure S2

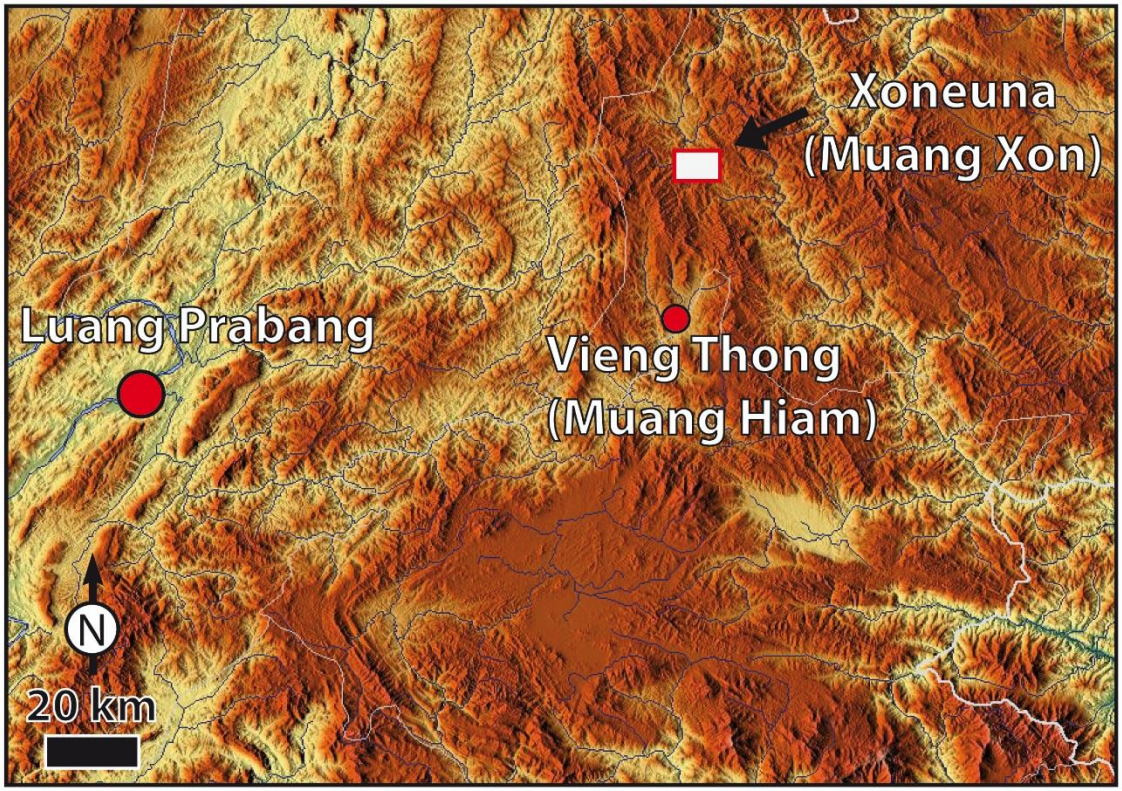

Map of Laos showing the studied area in the Hua Pan Province, 130 km NNE from Luang Prabang.

Figure S3

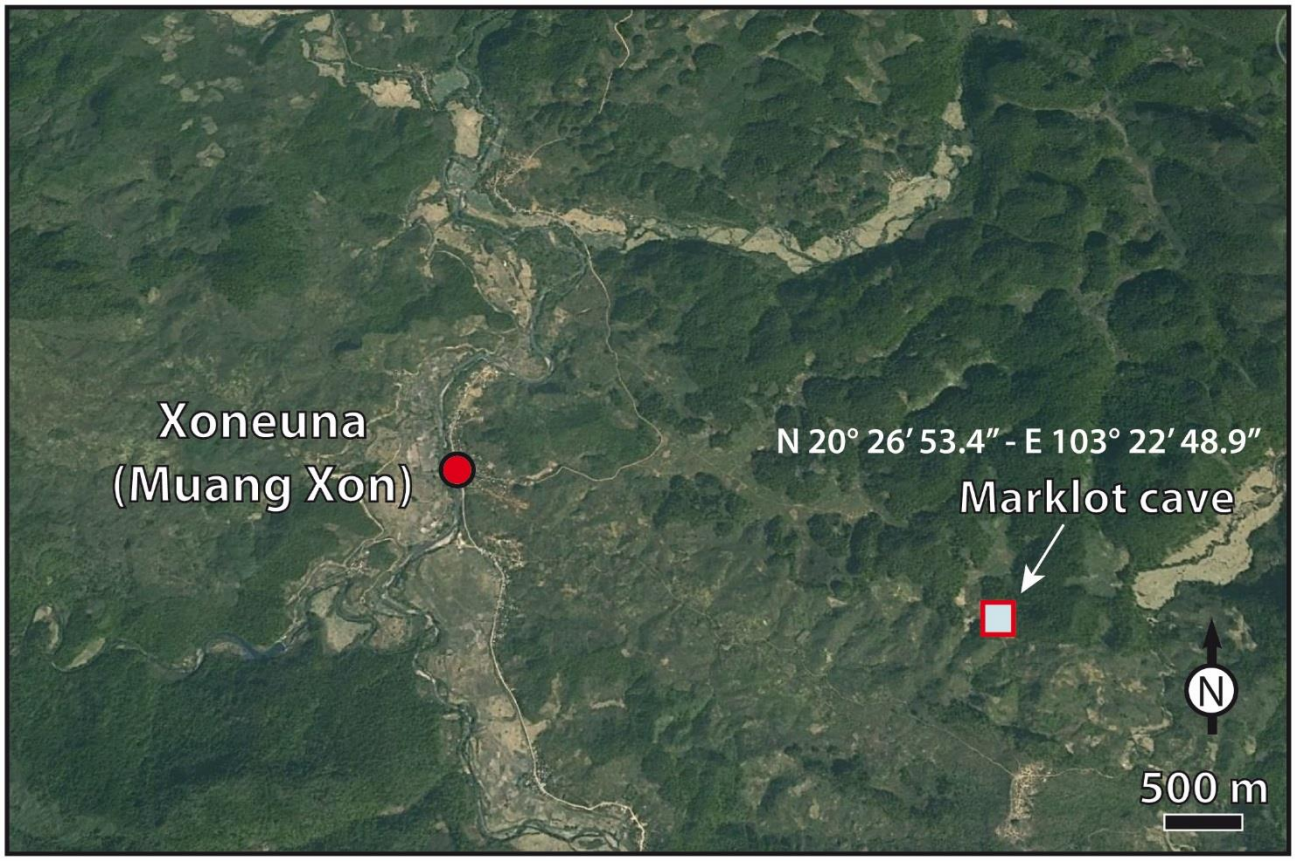

Satellite view of the studied area with the location of the cave 6 km SE from the city of Xoneuna (Muang Xon).

Figure S4

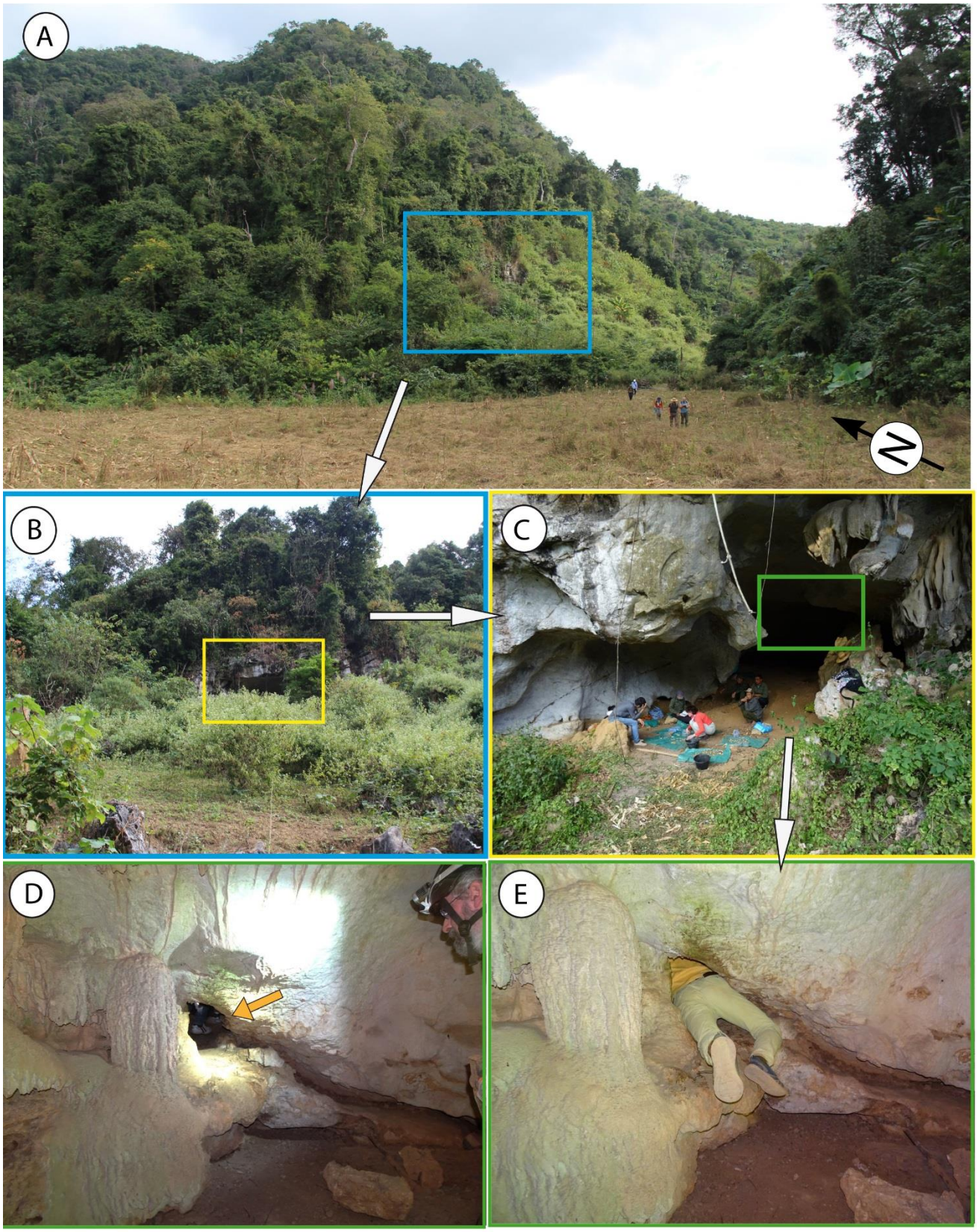

(A) Tam Hay Marklot cave at the foot of a tower karst covered by the forest, and (B, C) the first chamber at the entrance. (D, E) First passageway that leads to the gallery.

Figure S5

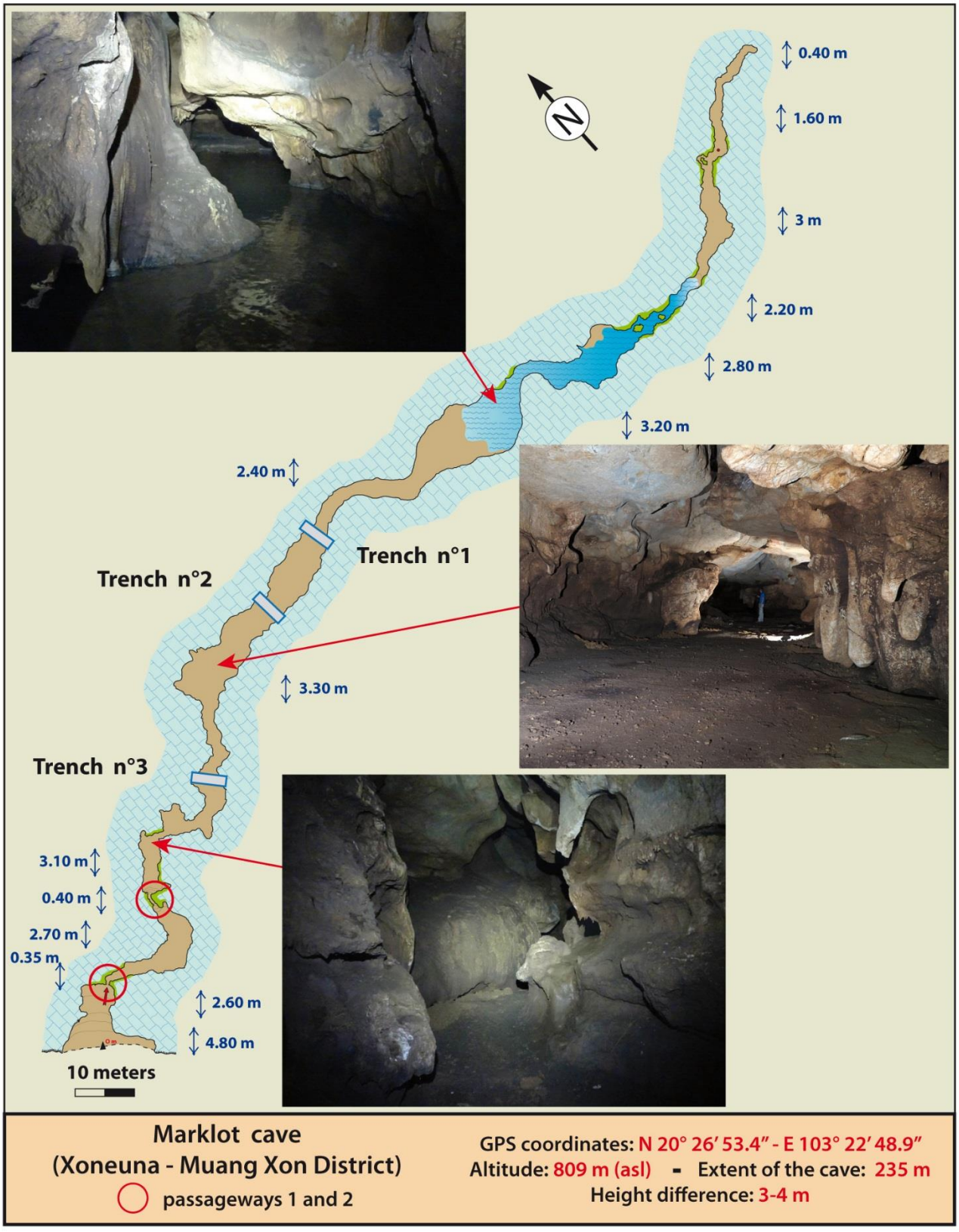

Map of the entire Tam Hay Marklot cave from the first chamber at the entrance to the dead-end after a 235 m extent, with three views of the gallery.

Figure S6

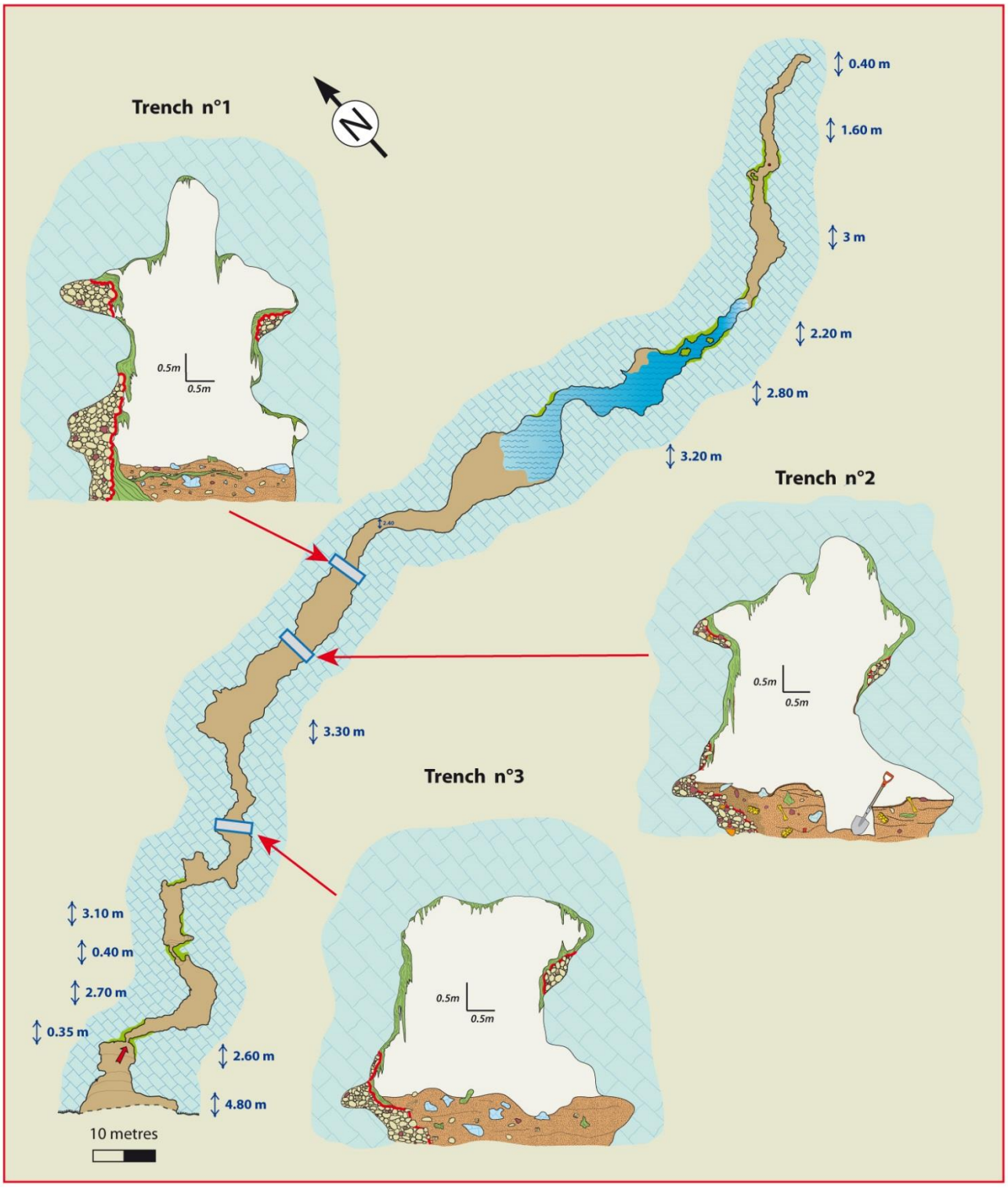

Map of the Tam Hay Marklot cave showing the three sections of the cave and their sedimentary fillings (see Figure 7 for the legend of sedimentary sections).

123 Figure S7

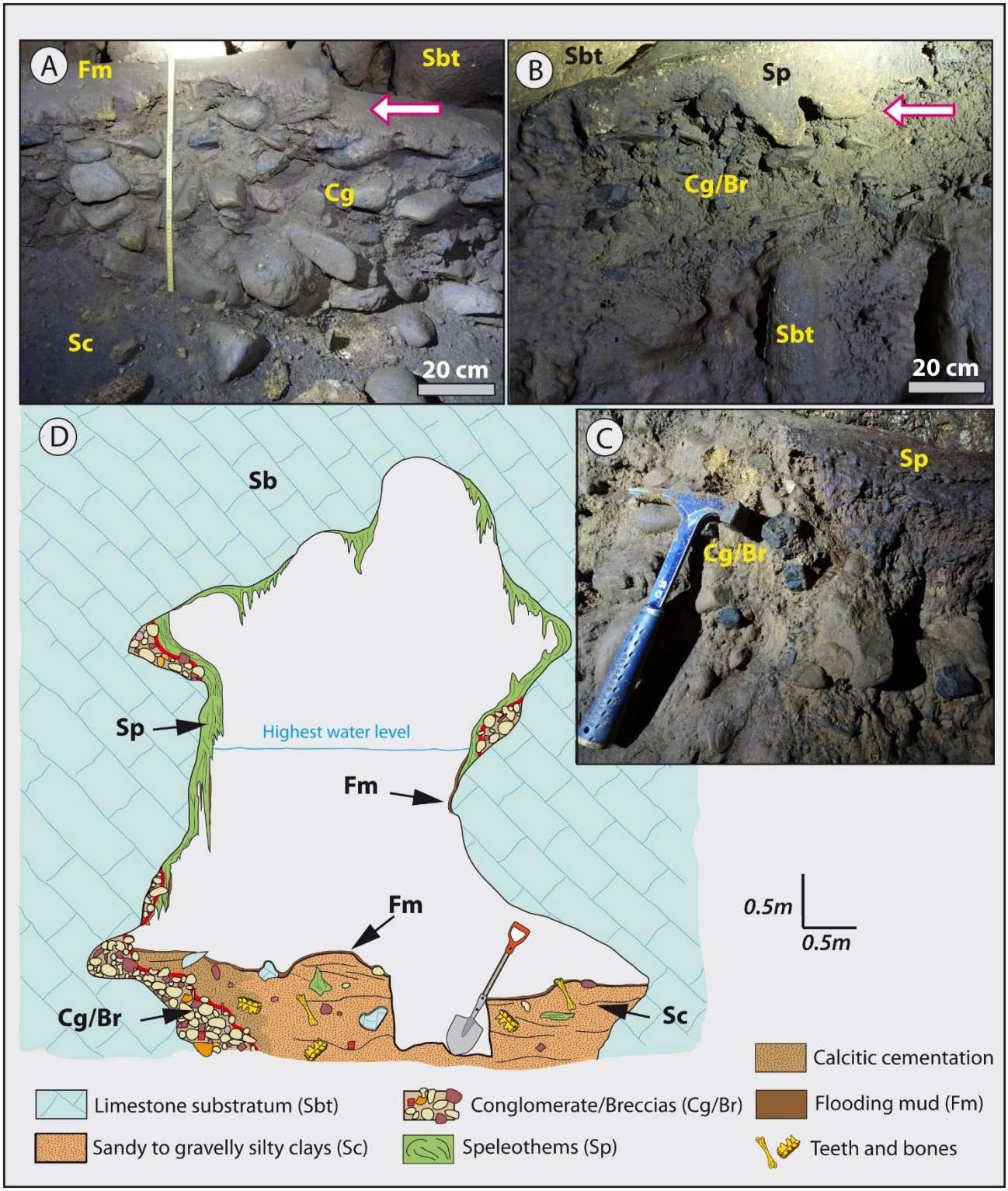

124 Detail of the section/trench 2 showing the main sedimentary facies of the cave. In A and B, the arrows
125 give the direction of the palaeocurrents from inside to outside of the cave.
126

Figure S8

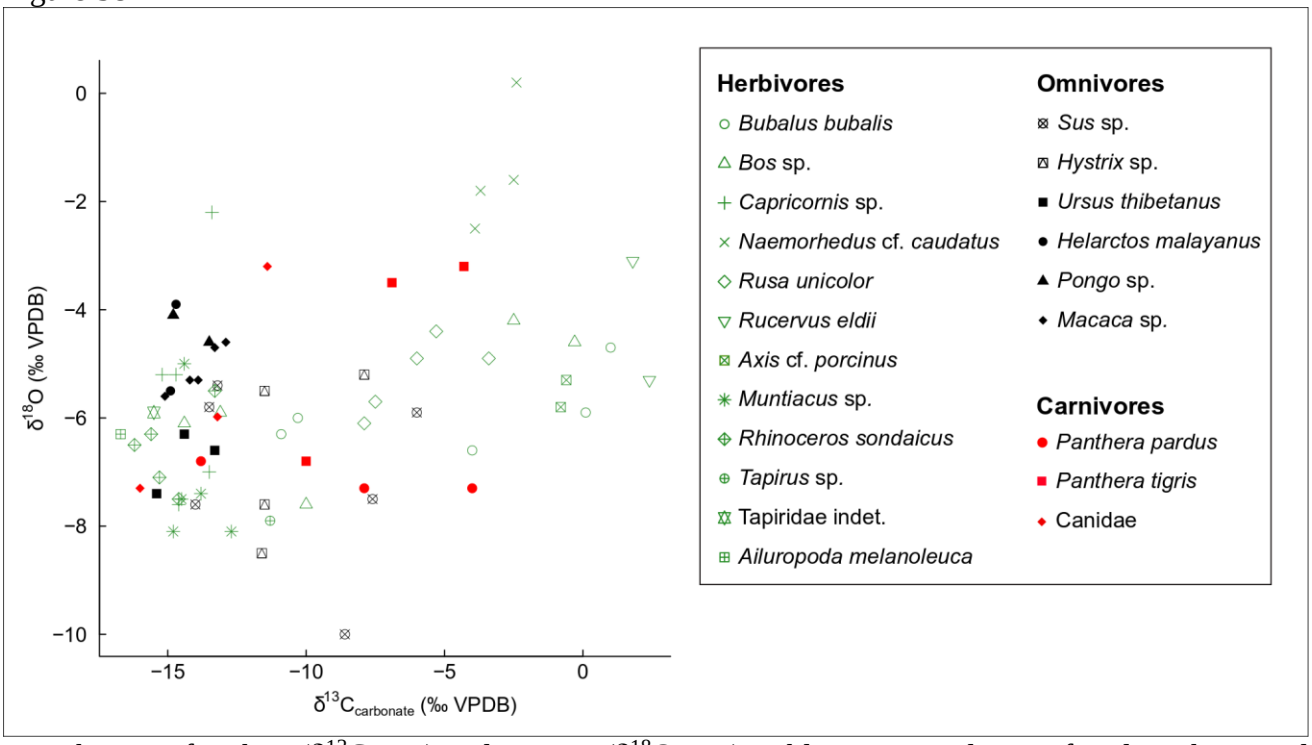

Distribution of carbon ($\delta^{13}C_{apatite}$) and oxygen ($\delta^{18}O_{apatite}$) stable isotope values in fossil tooth enamel from Tam Hay Marklot cave.

Figure S9

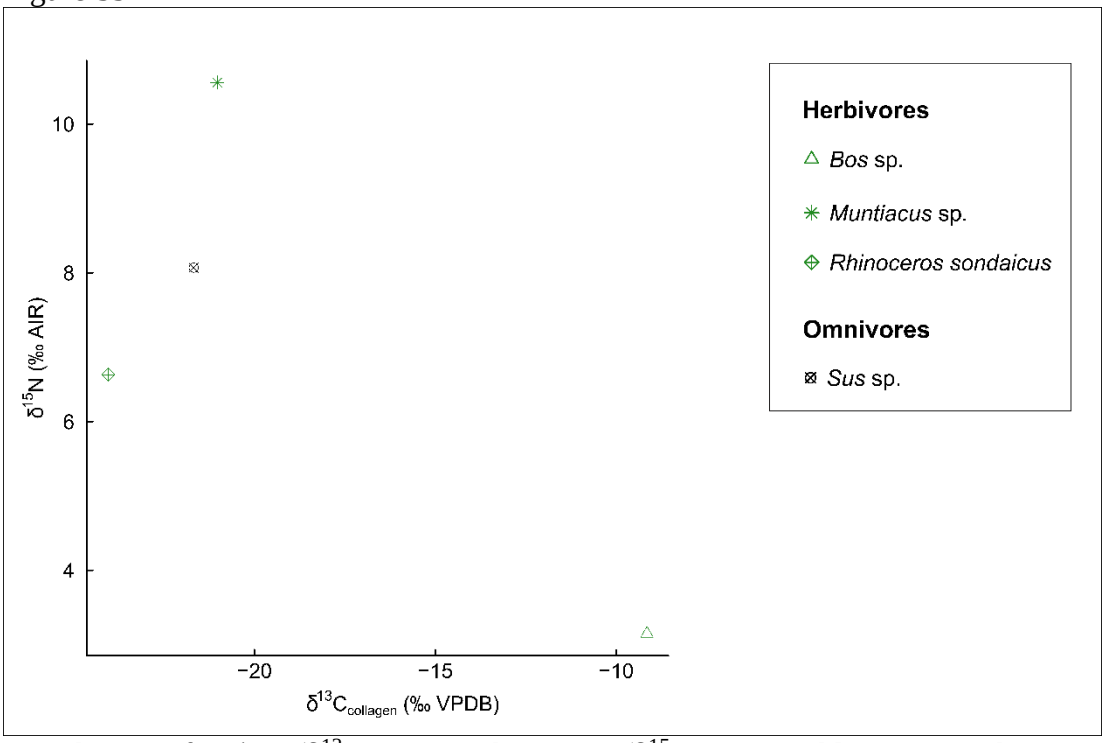

Distribution of carbon ($\delta^{13}C_{collagen}$) and nitrogen ($\delta^{15}N_{collagen}$) stable isotope values in root dentin of the few fossil teeth from Tam Hay Marklot cave with collagen preservation.

Figure S10

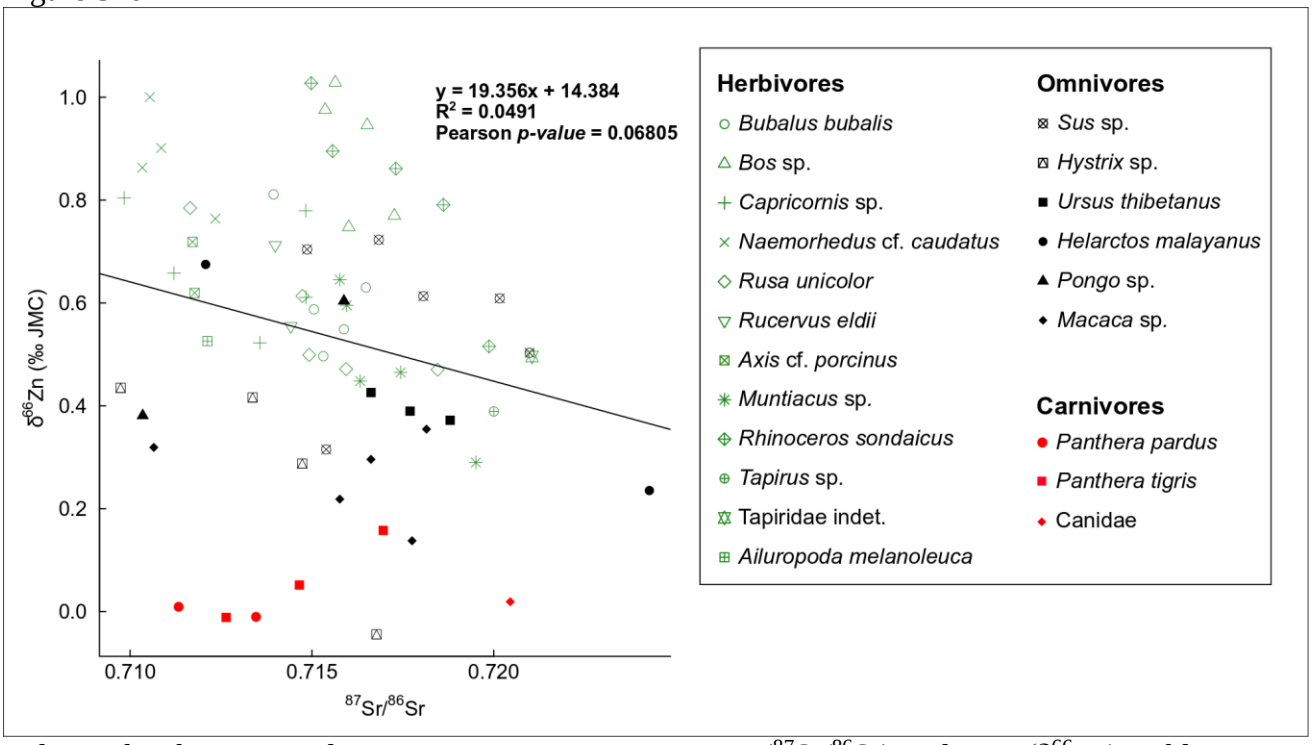

Relationship between radiogenic strontium isotope ratios ($^{87}Sr/^{86}Sr$) and zinc ($\delta^{66}Zn$) stable isotope values in enamel of fossil teeth from Tam Hay Marklot cave.

Figure S11

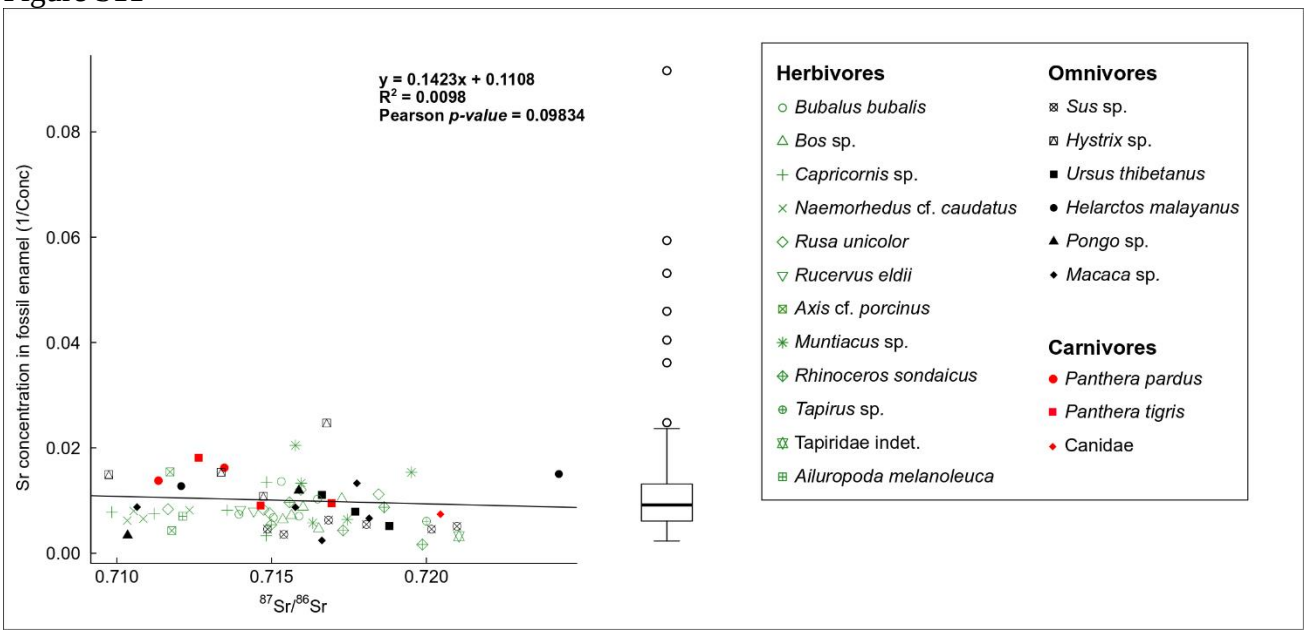

Relationship between the strontium concentration and the radiogenic strontium isotope ratios ($^{87}Sr/^{86}Sr$) in enamel of fossil teeth from Tam Hay Marklot cave. The boxes from the box and whisker plot represent the 25^{th}–75^{th} percentiles, with the median as a bold horizontal line, of Sr concentration from modern enamel of mammal teeth found elsewhere (122, 123, 158).

Figure S12

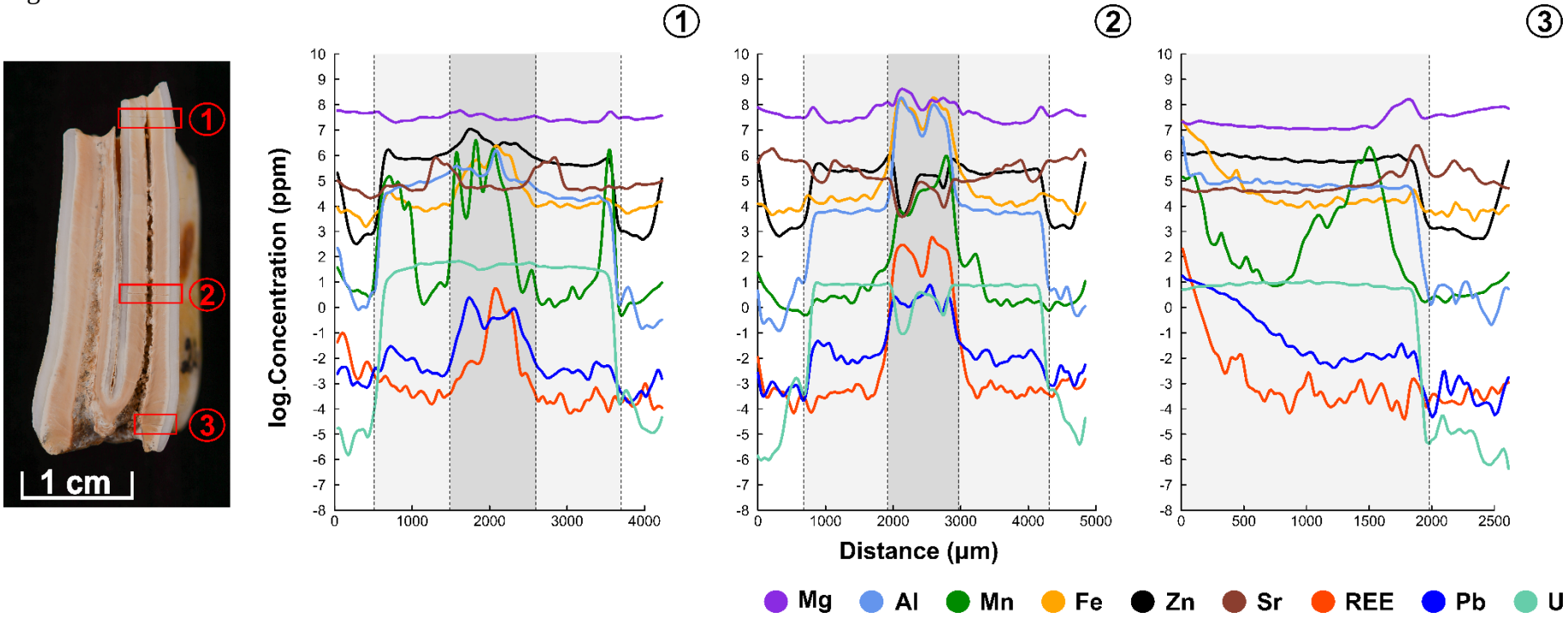

Spatial element concentration profiles for the element Zn, Fe, Mn, Al, Mg, Sr, Pb, U and rare earth elements (REE, calculated as the sum of all measured REE concentrations) of all LA-ICP-MS linescan analysis (1 to 3) of the Tam Hay Marklot cave fossil tooth (m3 right) specimen 34493 (*Capricornis* sp.). All concentration data (ppm) were log transformed. The different shaded areas, delimited by dotted lines, represent the different histological parts: white for enamel, light gray for dentin and medium gray for pulp cavity. The profiles follow a left-to-right direction as seen from the picture on the left.

Figure S13

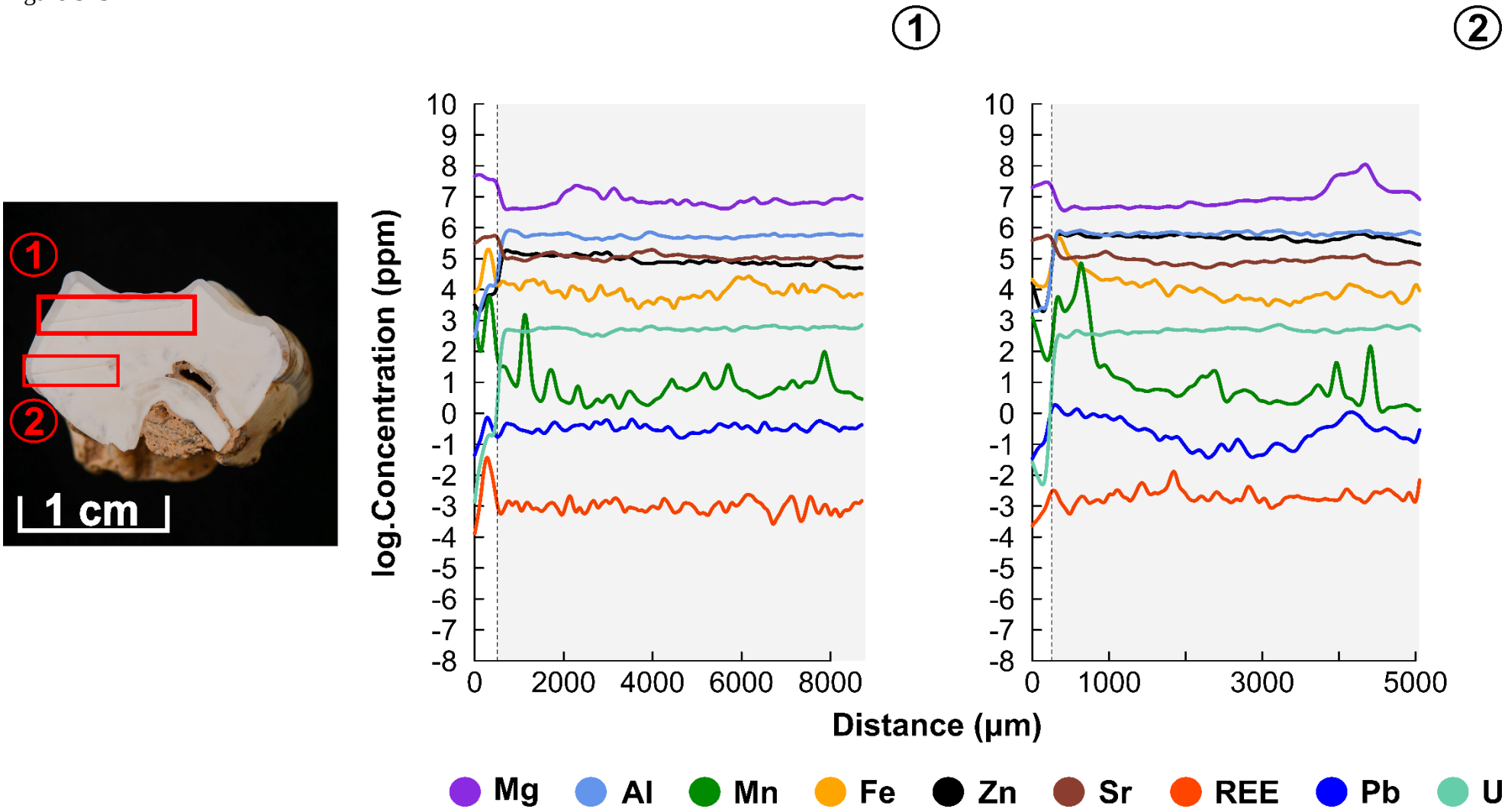

Spatial element concentration profiles for the element Zn, Fe, Mn, Al, Mg, Sr, Pb, U and rare earth elements (REE, calculated as the sum of all measured REE concentrations) of all LA-ICP-MS linescan analysis (1 and 2) of the Tam Hay Marklot cave fossil tooth (M2 left) specimen 34501 (*Ursus thibetanus*). All concentration data (ppm) were log transformed. The different shaded areas, delimited by dotted lines, represent the different histological parts: white for enamel, and light gray for dentin. The profiles follow a left-to-right direction as seen from the picture on the left.

Figure S14

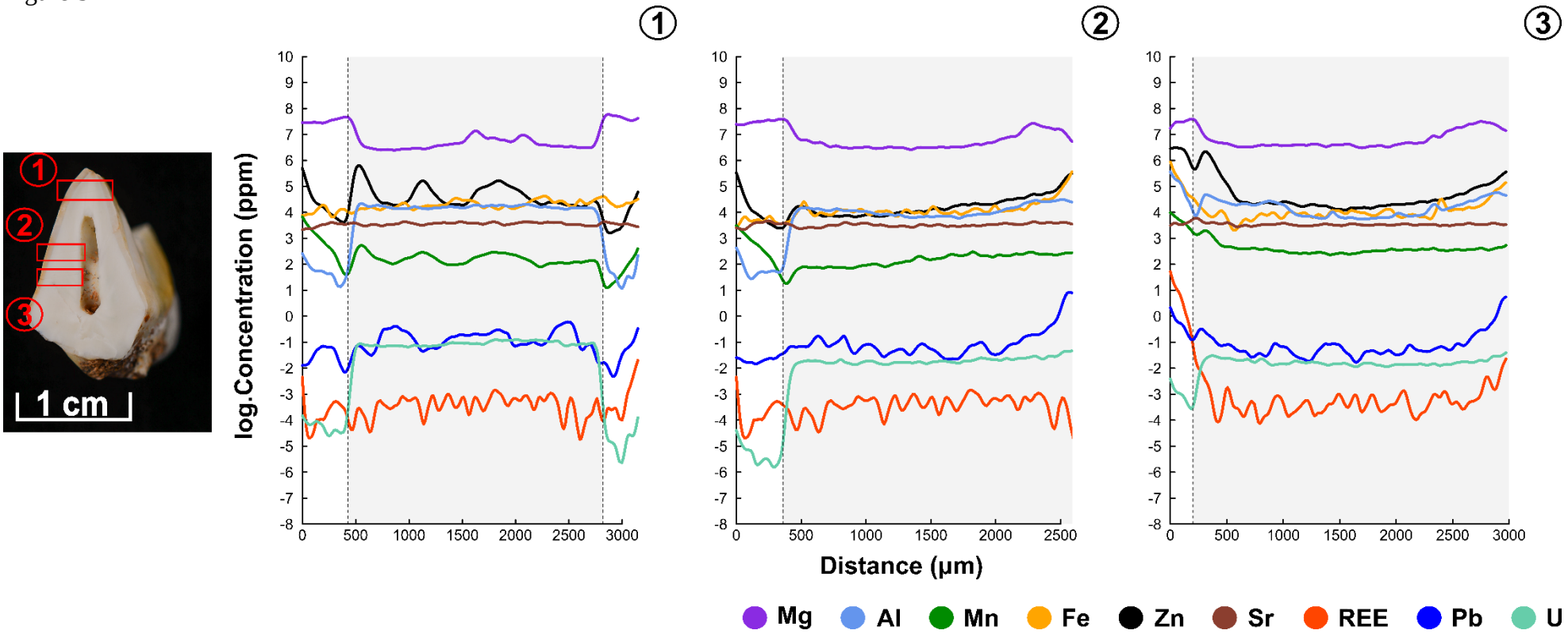

Spatial element concentration profiles for the element Zn, Fe, Mn, Al, Mg, Sr, Pb, U and rare earth elements (REE, calculated as the sum of all measured REE concentrations) of all LA-ICP-MS linescan analysis (1 to 3) of the Tam Hay Marklot cave fossil tooth (P4 left) specimen 34505 (*Panthera pardus*). All concentration data (ppm) were log transformed. The different shaded areas, delimited by dotted lines, represent the different histological parts: white for enamel, and light gray for dentin. The profiles follow a left-to-right direction as seen from the picture on the left.

Figure S15

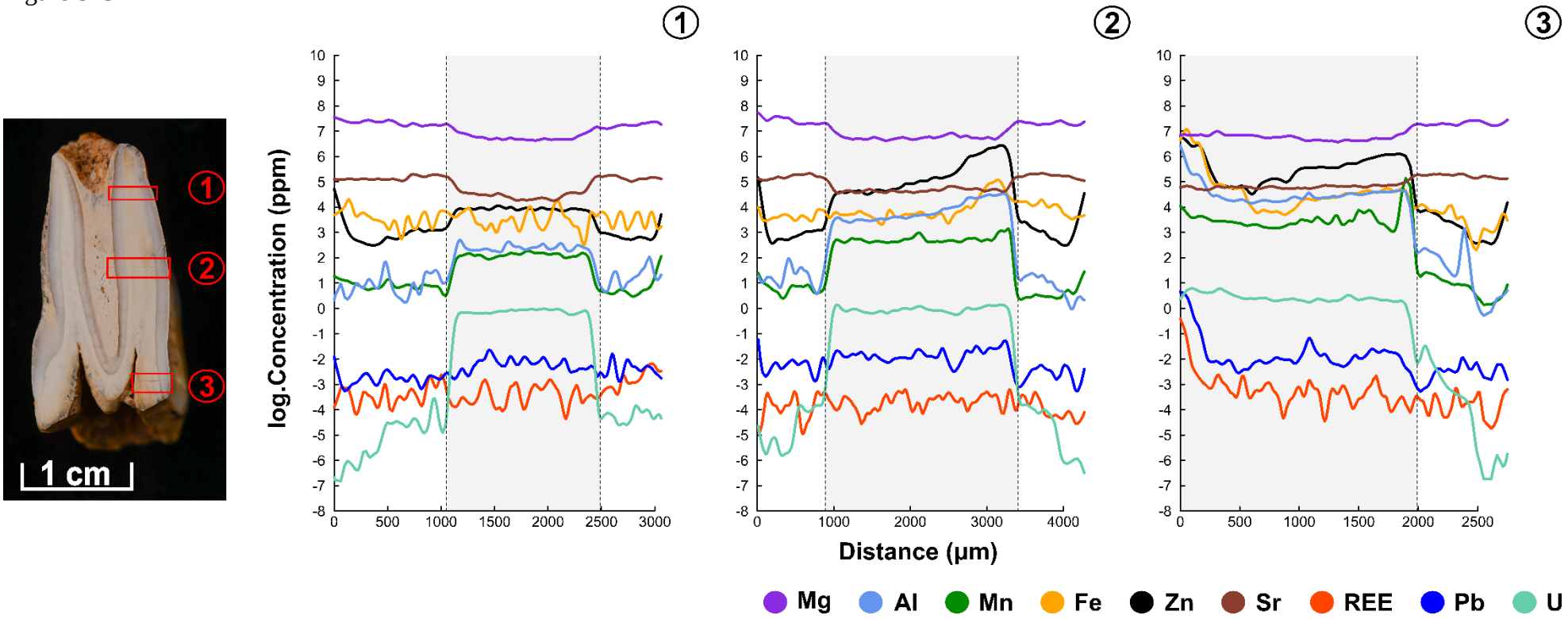

Spatial element concentration profiles for the element Zn, Fe, Mn, Al, Mg, Sr, Pb, U and rare earth elements (REE, calculated as the sum of all measured REE concentrations) of all LA-ICP-MS linescan analysis (1 to 3) of the Tam Hay Marklot cave fossil tooth (p2/p3 left) specimen 34524 (*Bubalus bubalis*). All concentration data (ppm) were log transformed. The different shaded areas, delimited by dotted lines, represent the different histological parts: white for enamel, and light gray for dentin. The profiles follow a left-to-right direction as seen from the picture on the left.

Figure S16

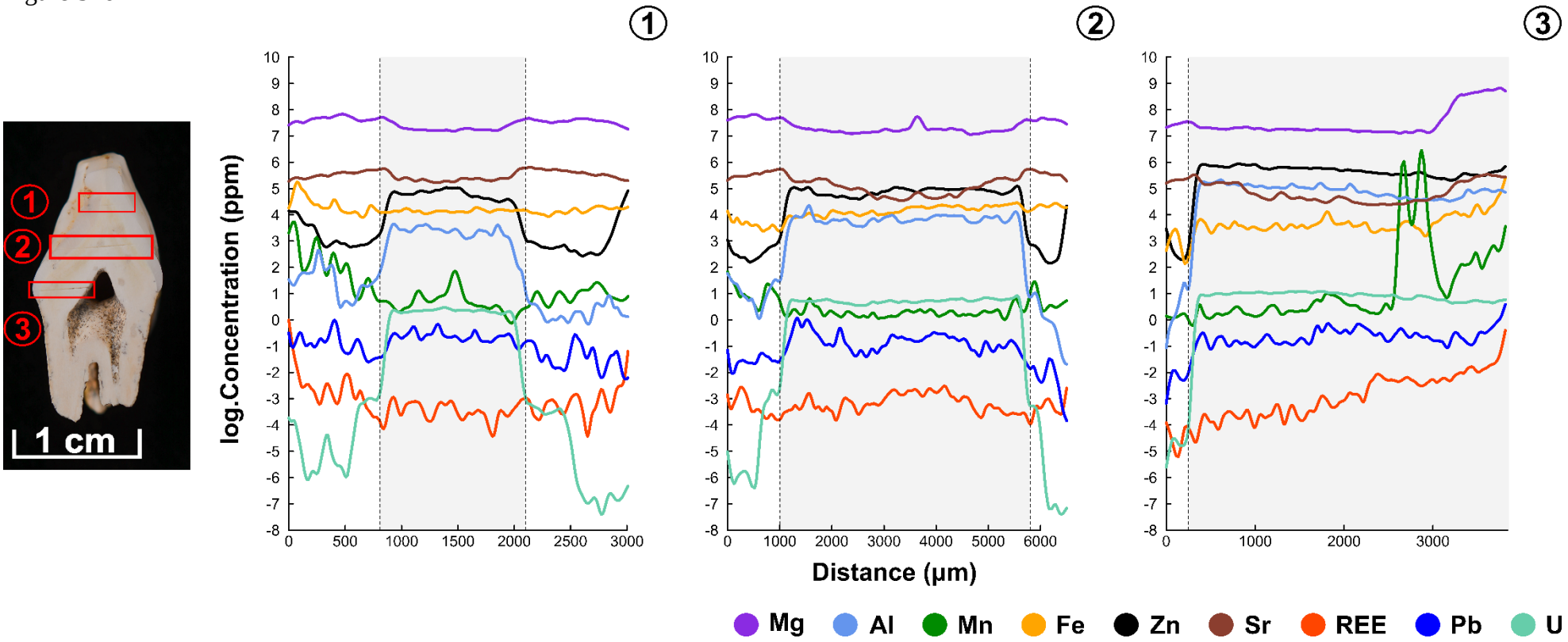

Spatial element concentration profiles for the element Zn, Fe, Mn, Al, Mg, Sr, Pb, U and rare earth elements (REE, calculated as the sum of all measured REE concentrations) of all LA-ICP-MS linescan analysis (1 to 3) of the Tam Hay Marklot cave fossil tooth (p4 left) specimen 34538 (*Sus* sp.). All concentration data (ppm) were log transformed. The different shaded areas, delimited by dotted lines, represent the different histological parts: white for enamel, and light gray for dentin. The profiles follow a left-to-right direction as seen from the picture on the left.

Figure S17

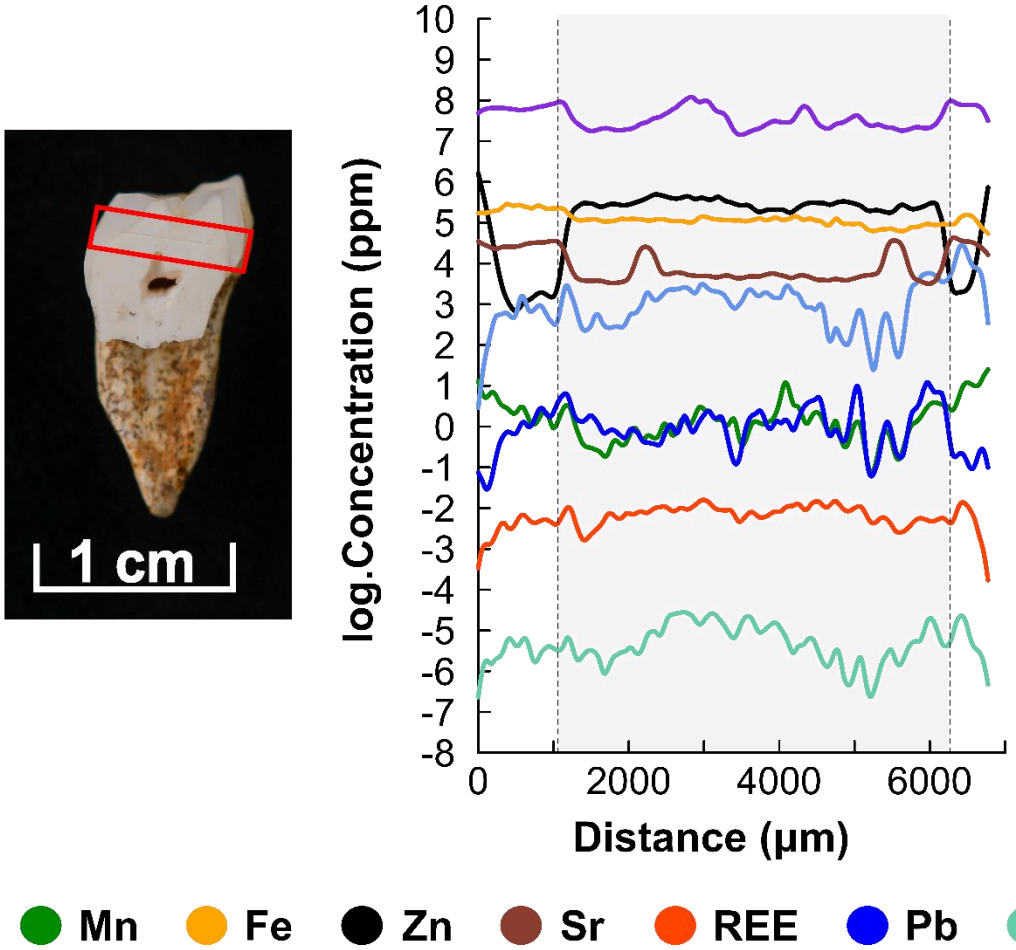

Spatial element concentration profiles for the element Zn, Fe, Mn, Al, Mg, Sr, Pb, U and rare earth elements (REE, calculated as the sum of all measured REE concentrations) of the single LA-ICP-MS linescan analysis of the Tam Hay Marklot cave fossil tooth (m1/m2 left) specimen 34548 (*Macaca* sp.). All concentration data (ppm) were log transformed. The different shaded areas, delimited by dotted lines, represent the different histological parts: white for enamel, and light gray for dentin. The profiles follow a left-to-right direction as seen from the picture on the left.

Figure S18

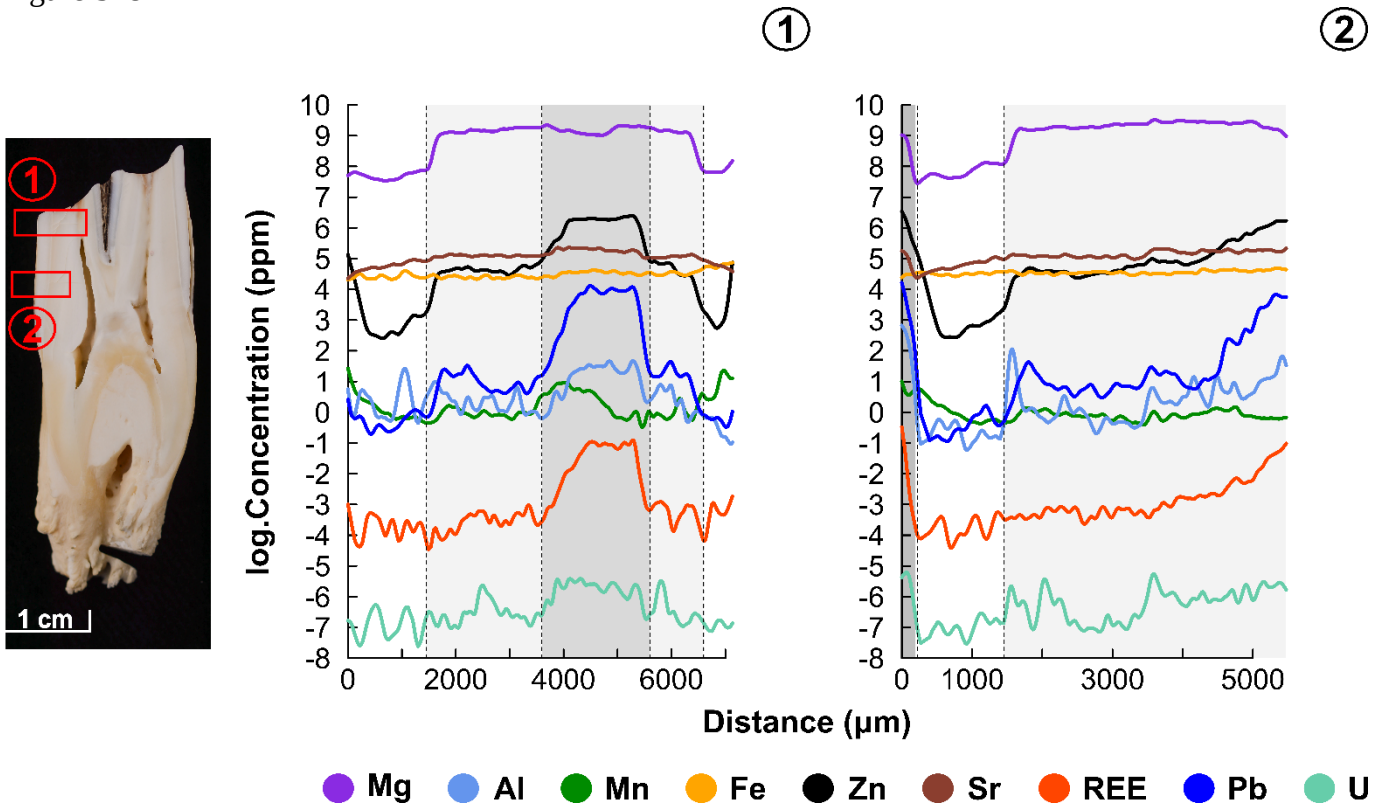

Spatial element concentration profiles for the element Zn, Fe, Mn, Al, Mg, Sr, Pb, U and rare earth elements (REE, calculated as the sum of all measured REE concentrations) of all LA-ICP-MS linescan analysis (1 and 2) of the Center of Natural History of Hamburg modern tooth (m3 right) specimen SEVA 34707 / ZMH-S-10461 (*Bison bison*). All concentration data (ppm) were log transformed. The different shaded areas, delimited by dotted lines, represent the different histological parts: white for enamel, light gray for dentin, medium gray for pulp cavity, and dark gray for calculus. The profiles follow a left-to-right direction as seen from the picture on the left.

Figure S19

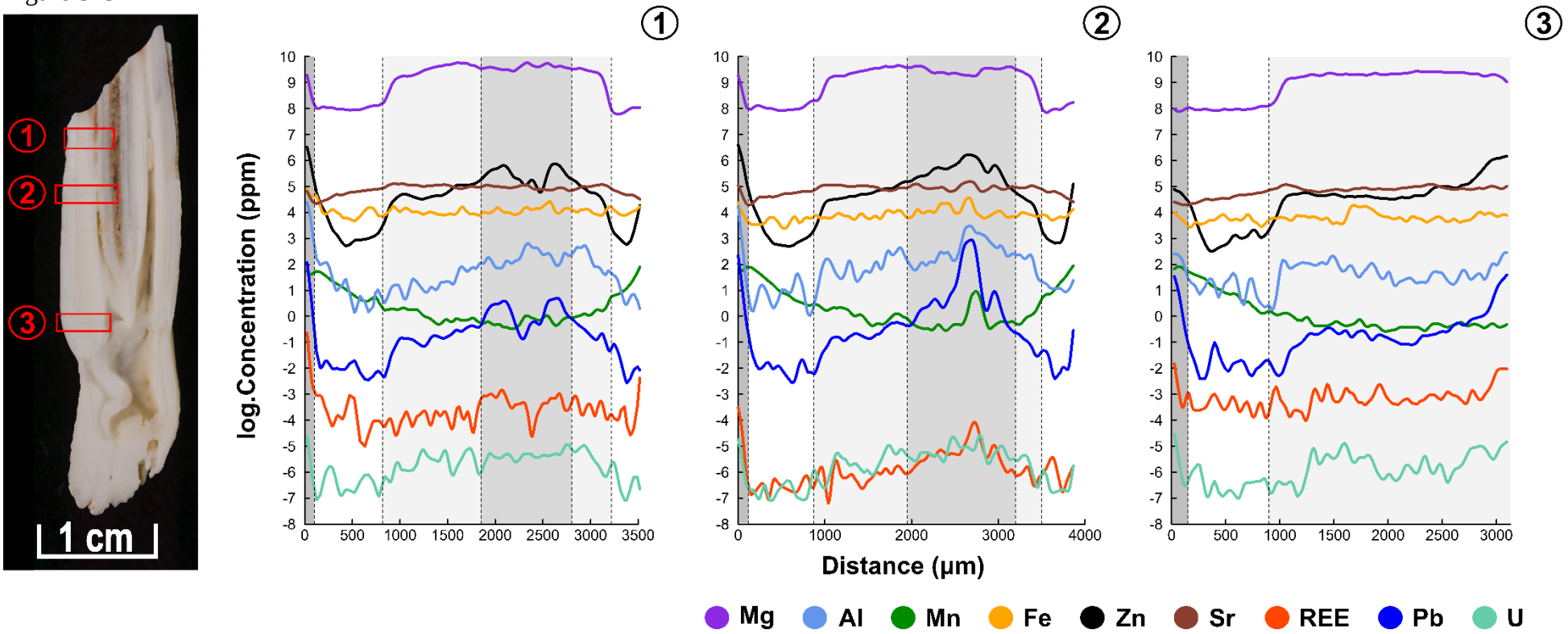

Spatial element concentration profiles for the element Zn, Fe, Mn, Al, Mg, Sr, Pb, U and rare earth elements (REE, calculated as the sum of all measured REE concentrations) of all LA-ICP-MS linescan analysis (1 to 3) of the Center of Natural History of Hamburg modern tooth (m3 left) specimen SEVA 34708 / ZMH-S-10963 (*Hemitragus jemlahicus*). All concentration data (ppm) were log transformed. The different shaded areas, delimited by dotted lines, represent the different histological parts: white for enamel, light gray for dentin, medium gray for pulp cavity, and dark gray for calculus. The profiles follow a left-to-right direction as seen from the picture on the left.

Figure S20

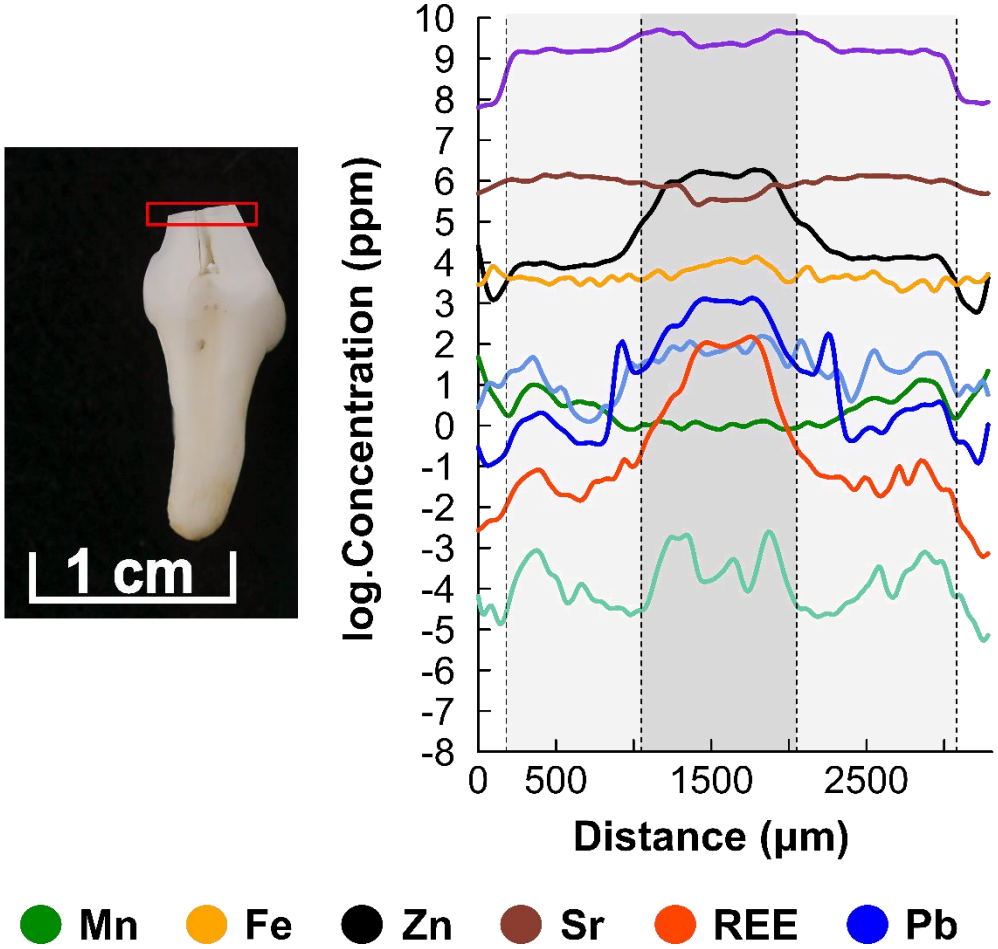

Spatial element concentration profiles for the element Zn, Fe, Mn, Al, Mg, Sr, Pb, U and rare earth elements (REE, calculated as the sum of all measured REE concentrations) of the single LA-ICP-MS linescan analysis of the Center of Natural History of Hamburg modern tooth (p3/p4) specimen SEVA 34709/ZMH-S-10612 (*Pteronura brasiliensis*). All concentration data (ppm) were log transformed. The different shaded areas, delimited by dotted lines, represent the different histological parts: white for enamel, light gray for dentin, and medium gray for pulp cavity. The profiles follow a left-to-right direction as seen from the picture on the left.

Figure S21

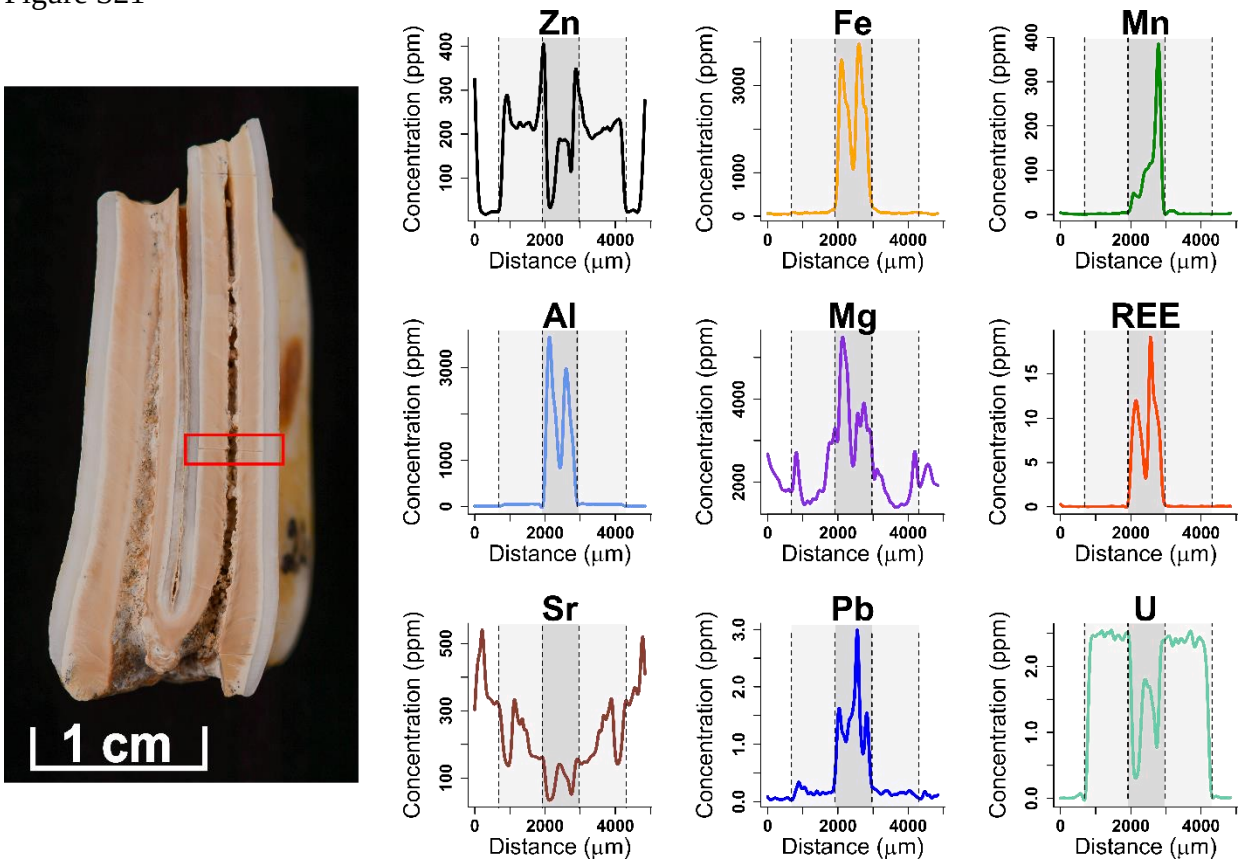

Typical concentrations (ppm) observed through spatial element concentration profiles for the element Zn, Fe, Mn, Al, Mg, Sr, Pb, U and rare earth elements (REE, calculated as the sum of all measured REE concentrations) of the Tam Hay Marklot cave fossil tooth (m3 right) specimen 34493 (*Capricornis* sp.). The different shaded areas, delimited by dotted lines, represent the different histological parts: white for enamel, light gray for dentin, and medium gray for pulp cavity. The profiles follow a left-to-right direction as seen from the picture on the left.

Figure S22

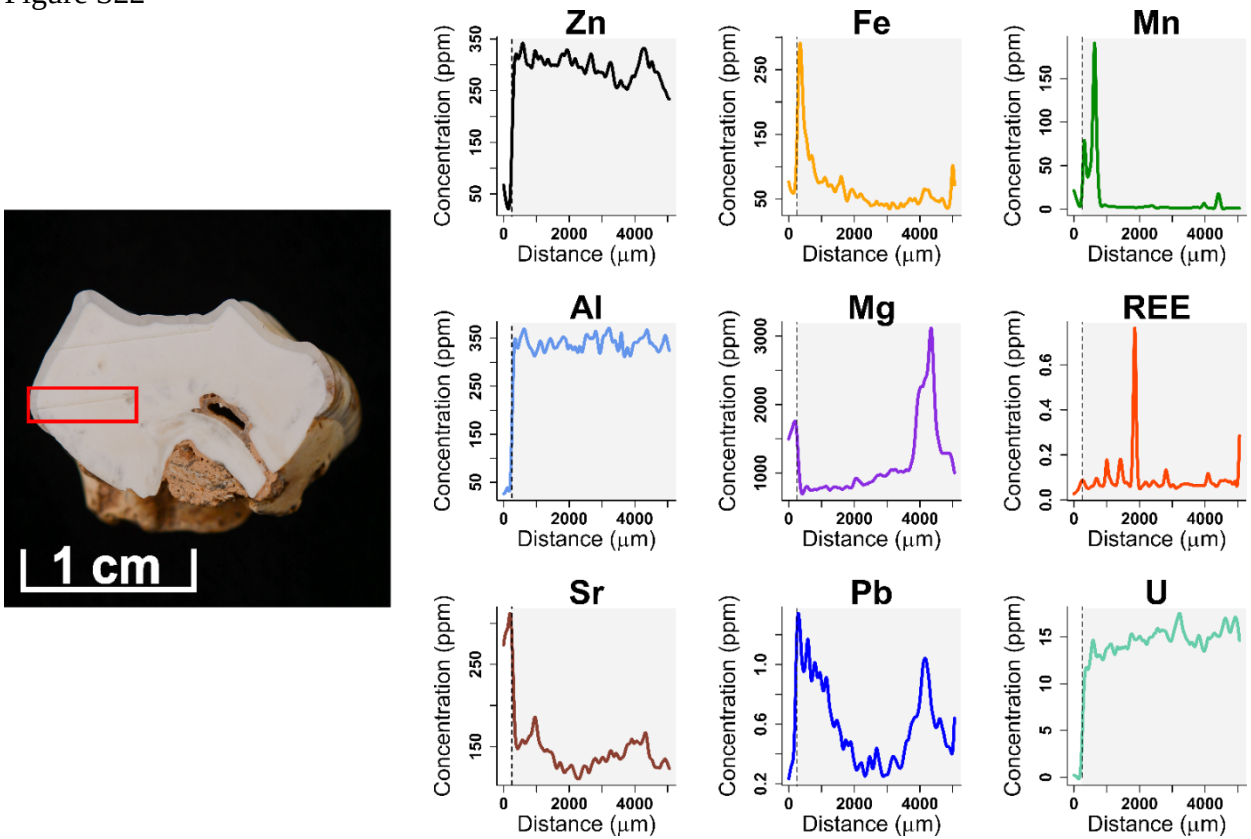

Typical concentrations (ppm) observed through spatial element concentration profiles for the element Zn, Fe, Mn, Al, Mg, Sr, Pb, U and rare earth elements (REE, calculated as the sum of all measured REE concentrations) of the Tam Hay Marklot cave fossil tooth (M2 left) specimen 34501 (*Ursus thibetanus*). All concentration (ppm) were log transformed. The different shaded areas, delimited by dotted lines, represent the different histological parts: white for enamel, and light gray for dentin. The profiles follow a left-to-right direction as seen from the picture on the left.

Figure S23

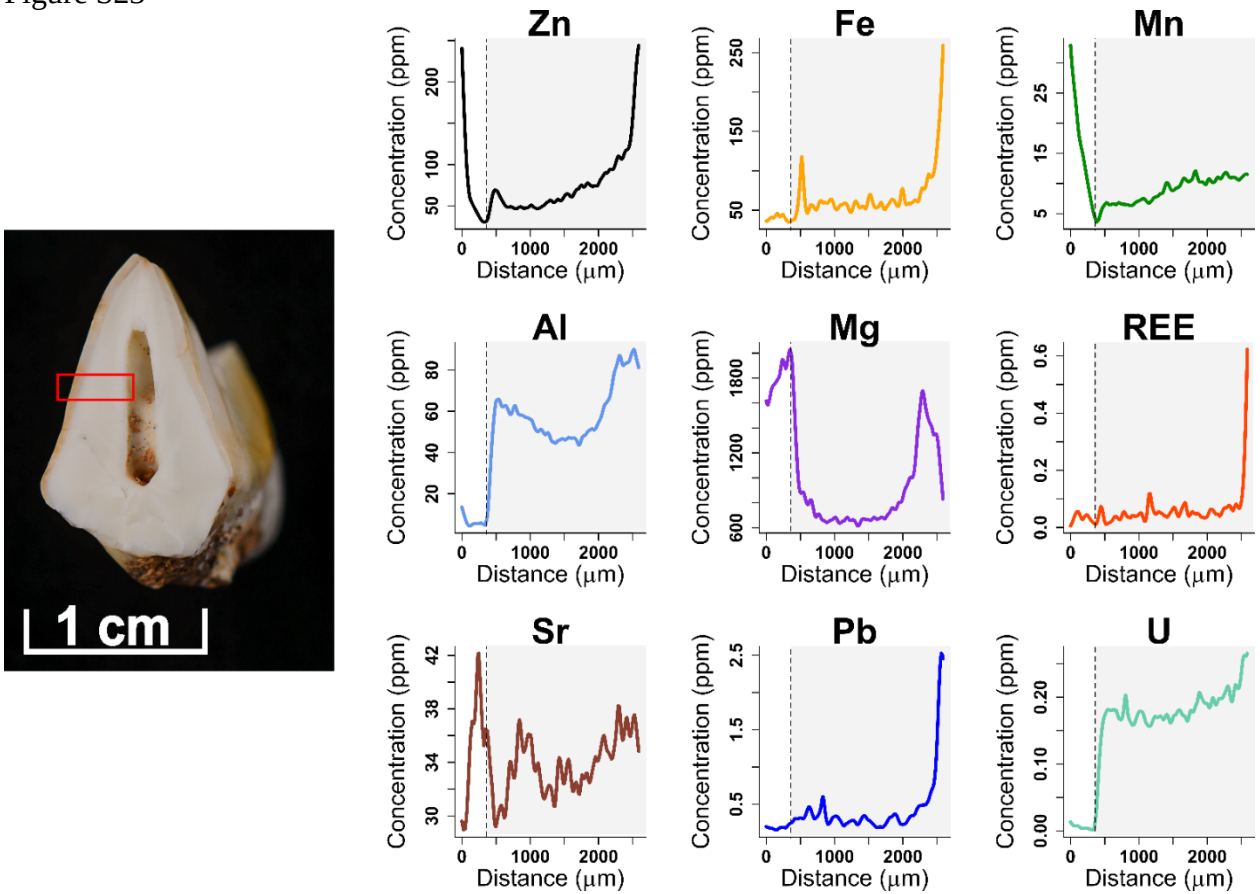

Typical concentrations (ppm) observed through spatial element concentration profiles for the element Zn, Fe, Mn, Al, Mg, Sr, Pb, U and rare earth elements (REE, calculated as the sum of all measured REE concentrations) of the Tam Hay Marklot cave fossil tooth (P4 left) specimen 34505 (*Panthera pardus*). All concentration (ppm) were log transformed. The different shaded areas, delimited by dotted lines, represent the different histological parts: white for enamel, and light gray for dentin The profiles follow a left-to-right direction as seen from the picture on the left.

Figure S24

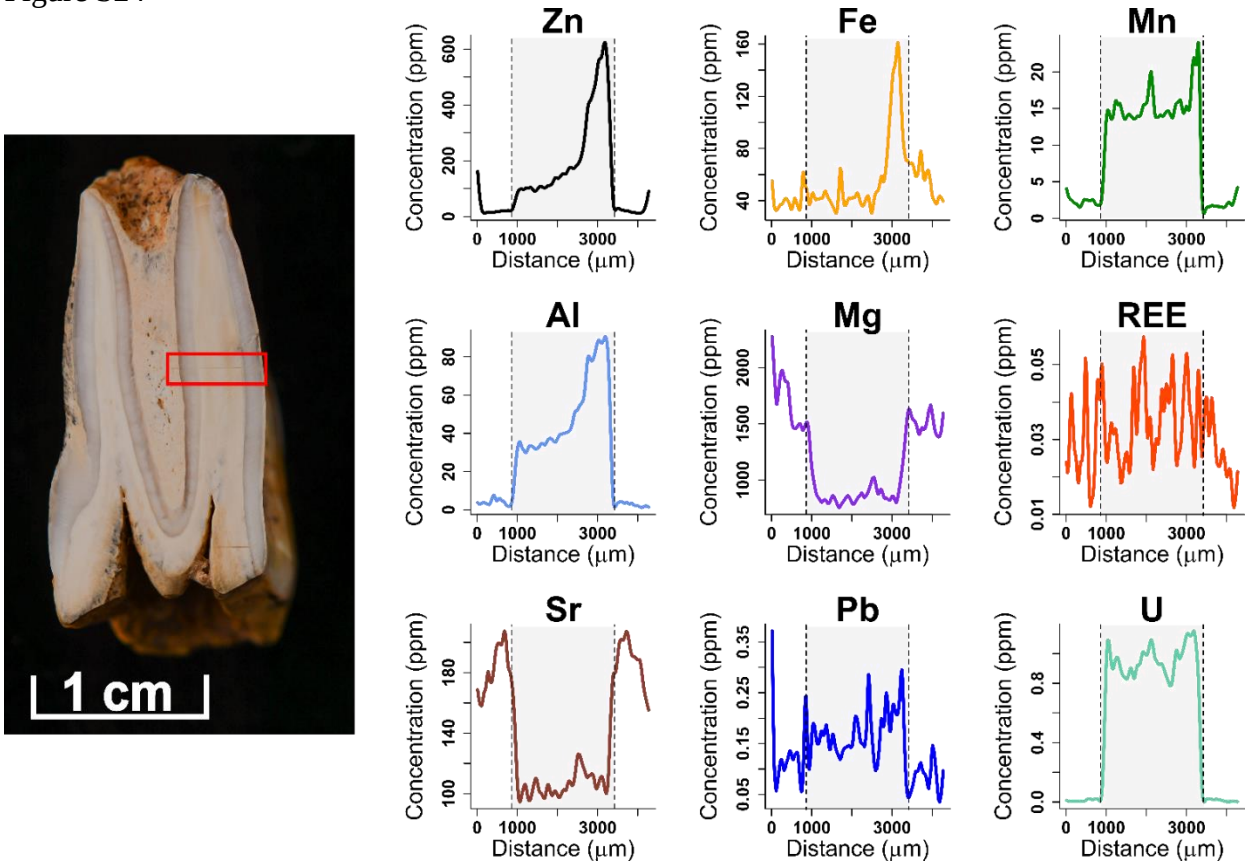

Typical concentrations (ppm) observed through spatial element concentration profiles for the element Zn, Fe, Mn, Al, Mg, Sr, Pb, U and rare earth elements (REE, calculated as the sum of all measured REE concentrations) of the Tam Hay Marklot cave fossil tooth (p2/p3 left) specimen 34524 (*Bubalus bubalis*). All concentration (ppm) were log transformed. The different shaded areas, delimited by dotted lines, represent the different histological parts: white for enamel, and light gray for dentin. The profiles follow a left-to-right direction as seen from the picture on the left.

Figure S25

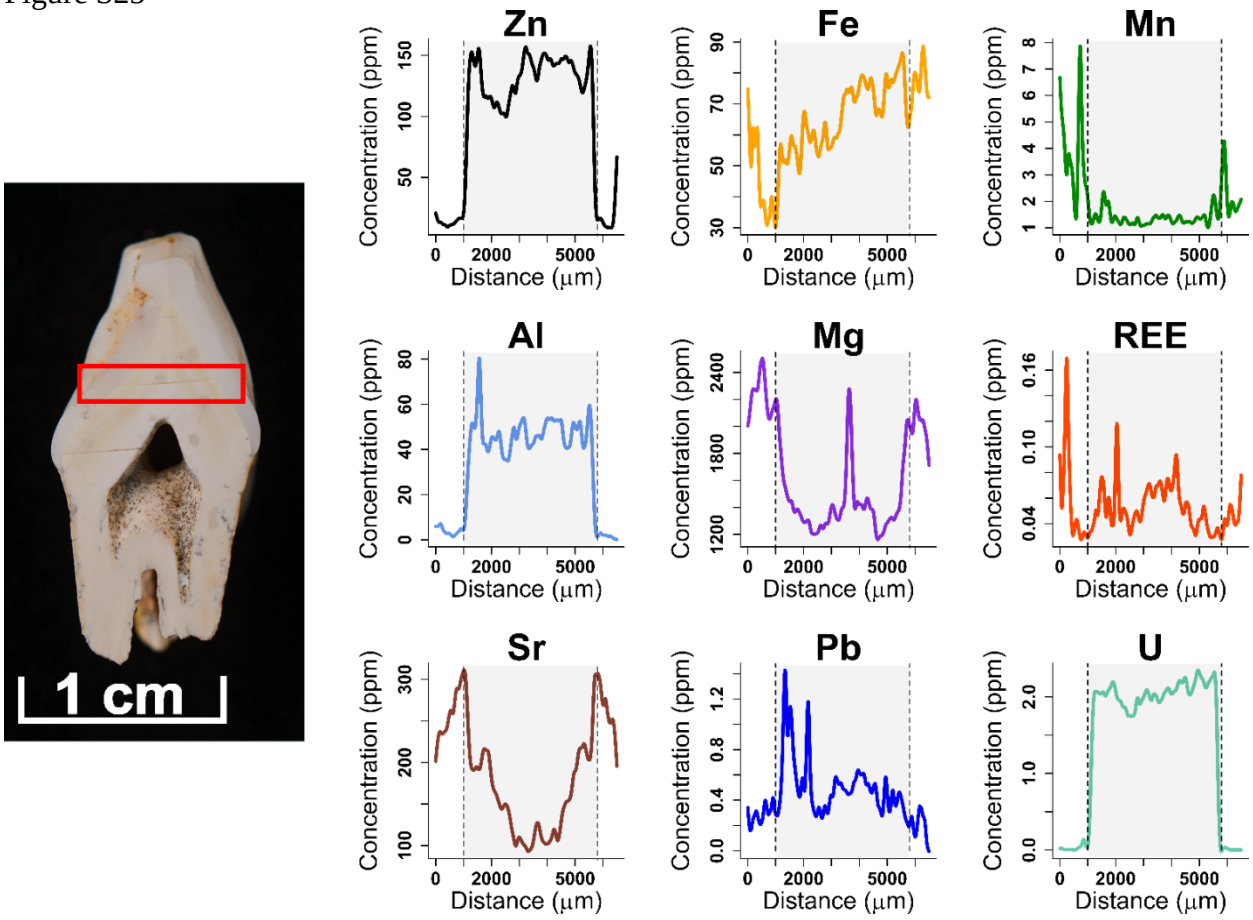

Typical concentrations (ppm) observed through spatial element concentration profiles for the element Zn, Fe, Mn, Al, Mg, Sr, Pb, U and rare earth elements (REE, calculated as the sum of all measured REE concentrations) of the Tam Hay Marklot cave fossil tooth (p4 left) specimen 34538 (*Sus* sp.). All concentration (ppm) were log transformed. The different shaded areas, delimited by dotted lines, represent the different histological parts: white for enamel, and light gray for dentin. The profiles follow a left-to-right direction as seen from the picture on the left.

Figure S26

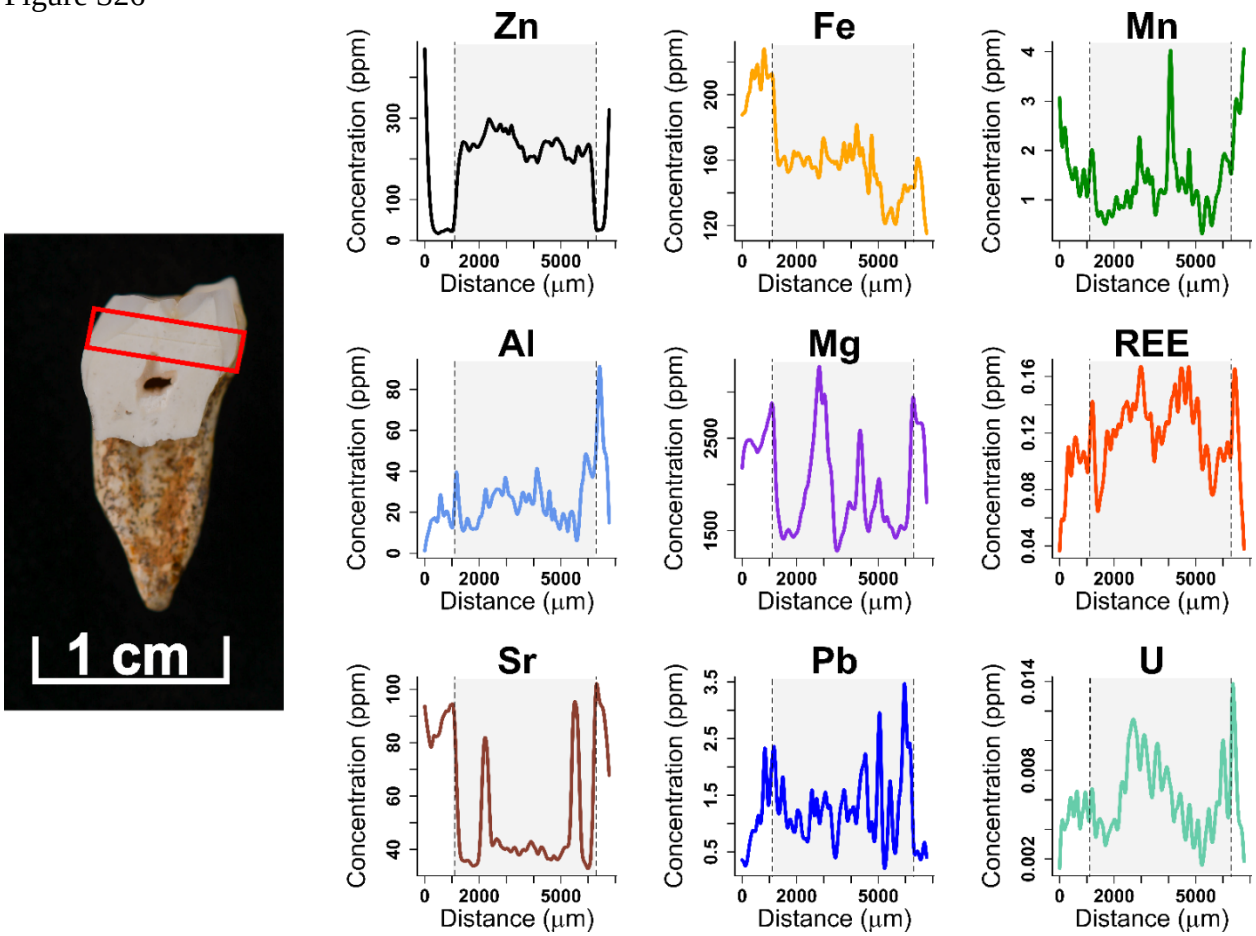

Typical concentrations (ppm) observed through spatial element concentration profiles for the element Zn, Fe, Mn, Al, Mg, Sr, Pb, U and rare earth elements (REE, calculated as the sum of all measured REE concentrations) of the Tam Hay Marklot cave fossil tooth (m1/m2 left) specimen 34548 (*Macaca* sp.). All concentration (ppm) were log transformed. The different shaded areas, delimited by dotted lines, represent the different histological parts: white for enamel, and light gray for dentin. The profiles follow a left-to-right direction as seen from the picture on the left.

Figure S27

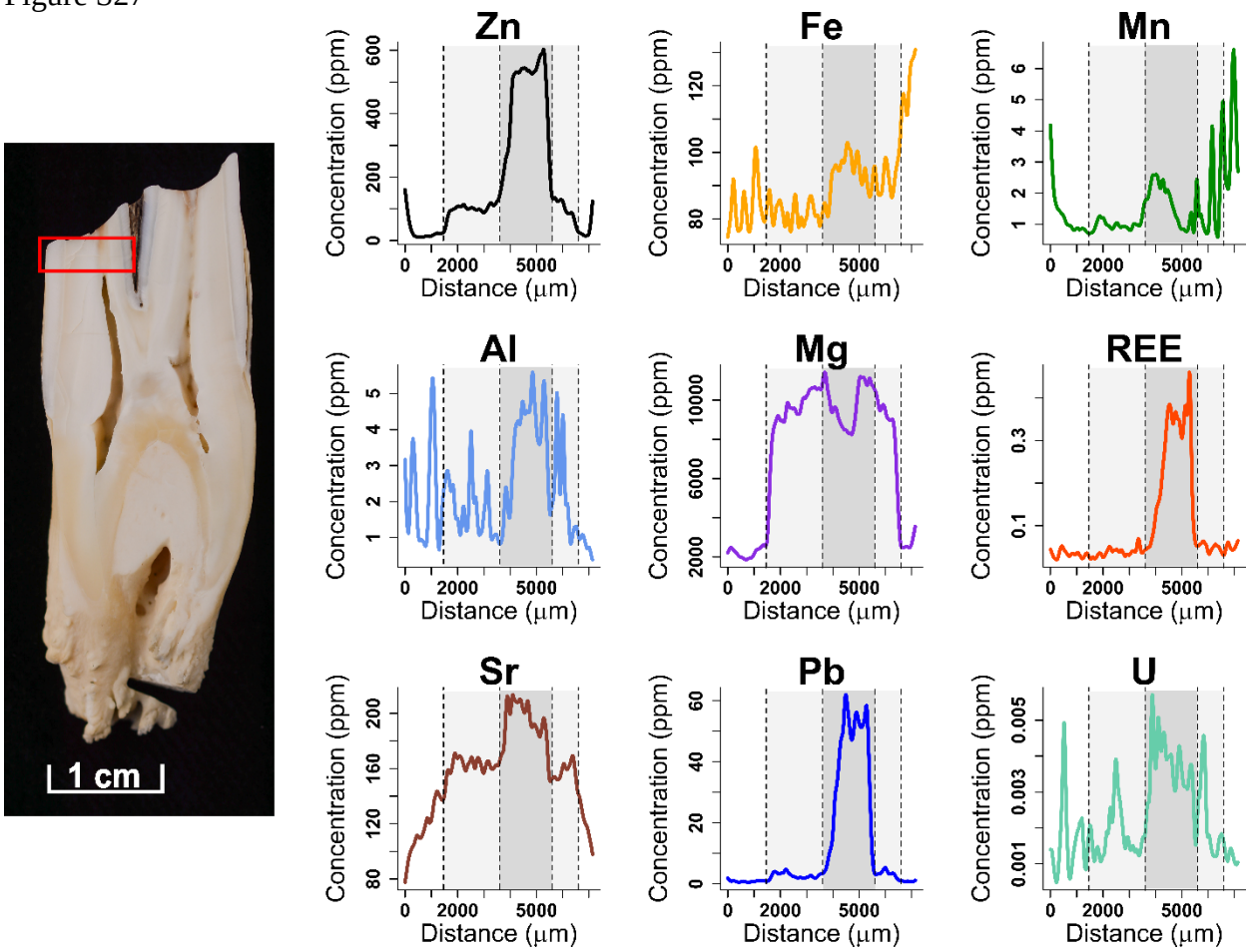

Typical concentrations (ppm) observed through spatial element concentration profiles for the element Zn, Fe, Mn, Al, Mg, Sr, Pb, U and rare earth elements (REE, calculated as the sum of all measured REE concentrations) of the Center of Natural History of Hamburg modern tooth (m3 right) specimen SEVA 34707 / ZMH-S-10461 (*Bison bison*). All concentration (ppm) were log transformed. The different shaded areas, delimited by dotted lines, represent the different histological parts: white for enamel, light gray for dentin, and medium gray for pulp cavity. The profiles follow a left-to-right direction as seen from the picture on the left.

Figure S28

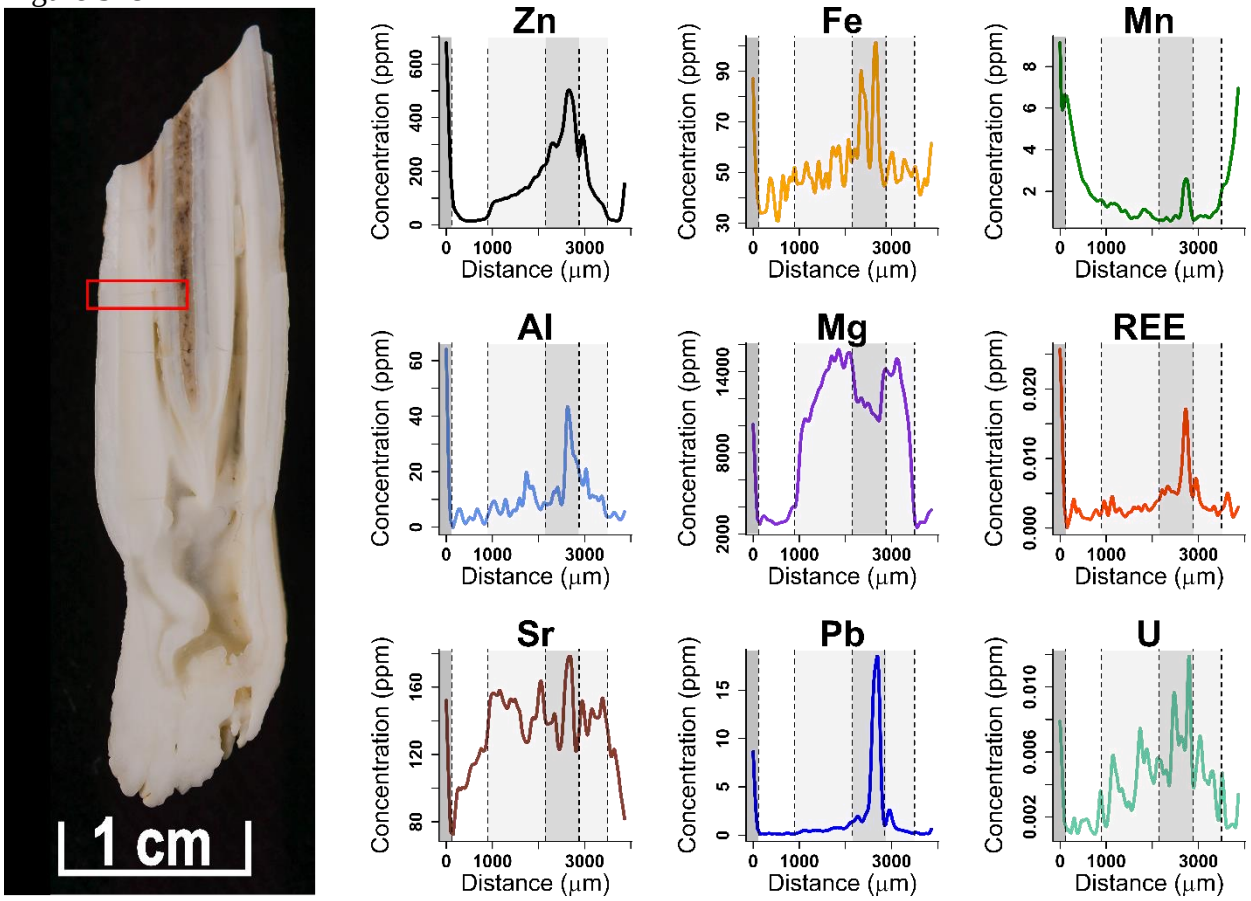

Typical concentrations (ppm) observed through spatial element concentration profiles for the element Zn, Fe, Mn, Al, Mg, Sr, Pb, U and rare earth elements (REE, calculated as the sum of all measured REE concentrations) of the Center of Natural History of Hamburg modern tooth (m3 left) specimen SEVA 34708 / ZMH-S-10963 (*Hemitragus jemlahicus*). All concentration (ppm) were log transformed. The different shaded areas, delimited by dotted lines, represent the different histological parts: white for enamel, light gray for dentin, medium gray for pulp cavity, and dark gray for calculus. The profiles follow a left-to-right direction as seen from the picture on the left.

Figure S29

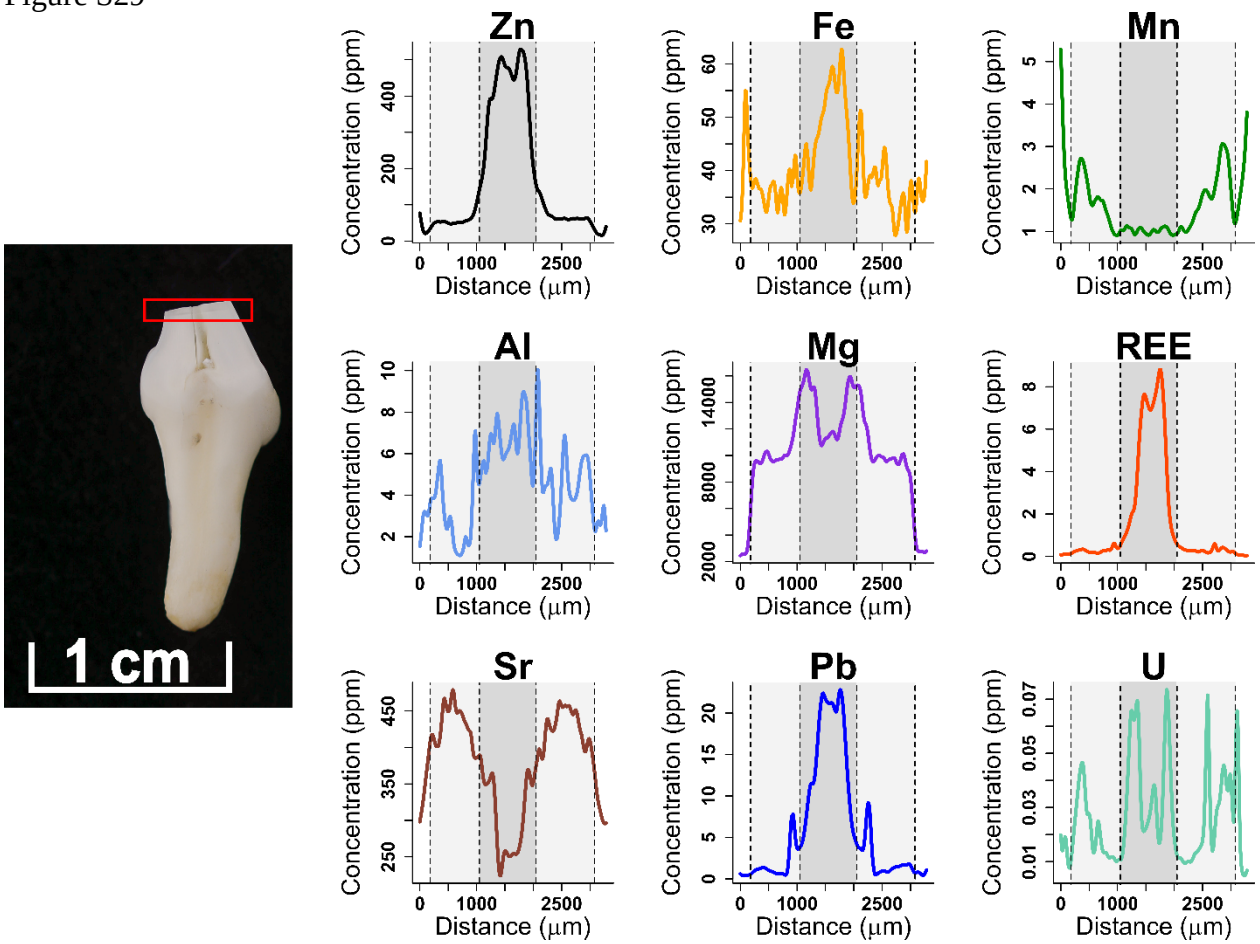

Typical concentrations (ppm) observed through spatial element concentration profiles for the element Zn, Fe, Mn, Al, Mg, Sr, Pb, U and rare earth elements (REE, calculated as the sum of all measured REE concentrations) of the Center of Natural History of Hamburg modern tooth (p3/p4) specimen SEVA 34709/ZMH-S-10612 (*Pteronura brasiliensis*). All concentration (ppm) were log transformed. The different shaded areas, delimited by dotted lines, represent the different histological parts: white for enamel, light gray for dentin, and medium gray for pulp cavity. The profiles follow a left-to-right direction as seen from the picture on the left.

Figure S30

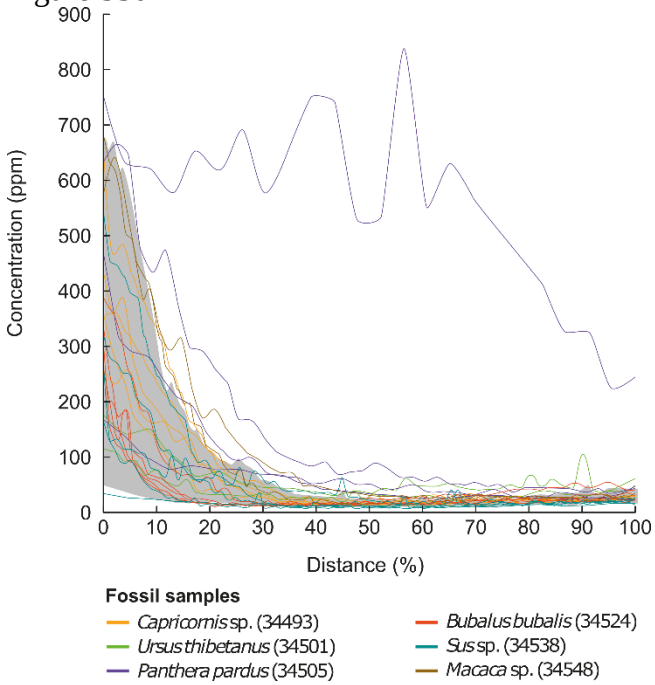

Zn concentration (ppm) distribution of every analyzed fossil enamel cross section segment, normalized to the relative enamel thickness (0% = outermost enamel layer, 100% = full thickness prior to analysis of enamel-dentin mixture). The gray area represents the concentration range observed in modern enamel cross section segments, colored lines those of the fossil enamel.

Figure S31

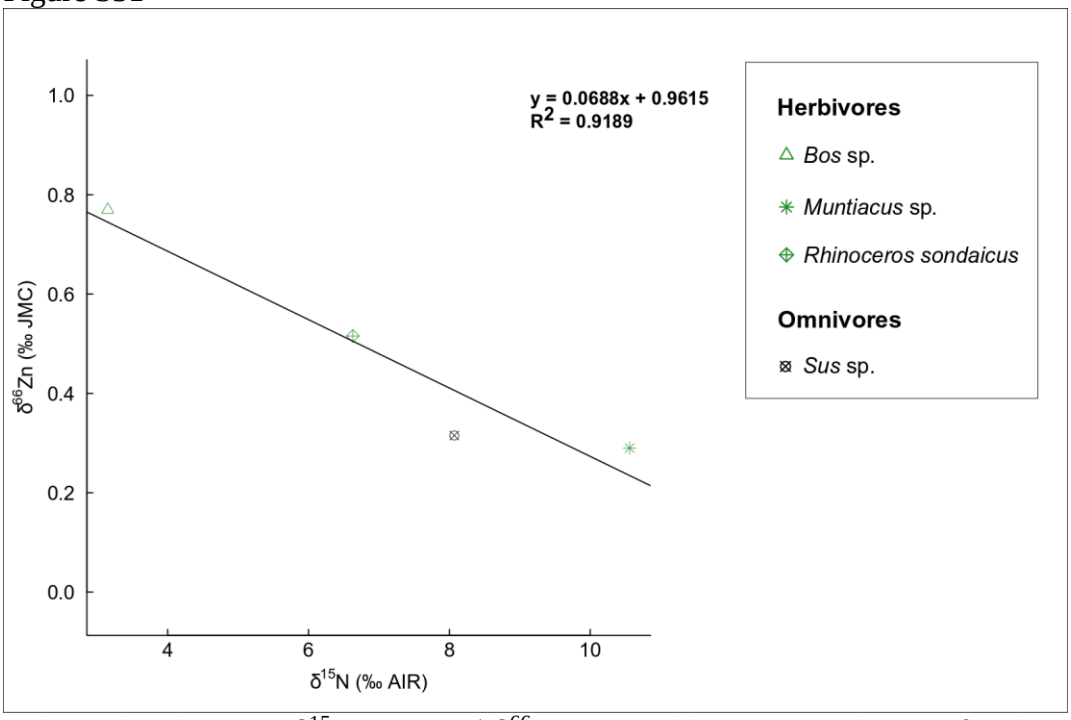

Relationship between $\delta^{15}N_{collagen}$ and $\delta^{66}Zn_{enamel}$ stable isotope values in fossil teeth from Tam Hay Marklot cave that yielded collagen from the dentin.

Figure S32

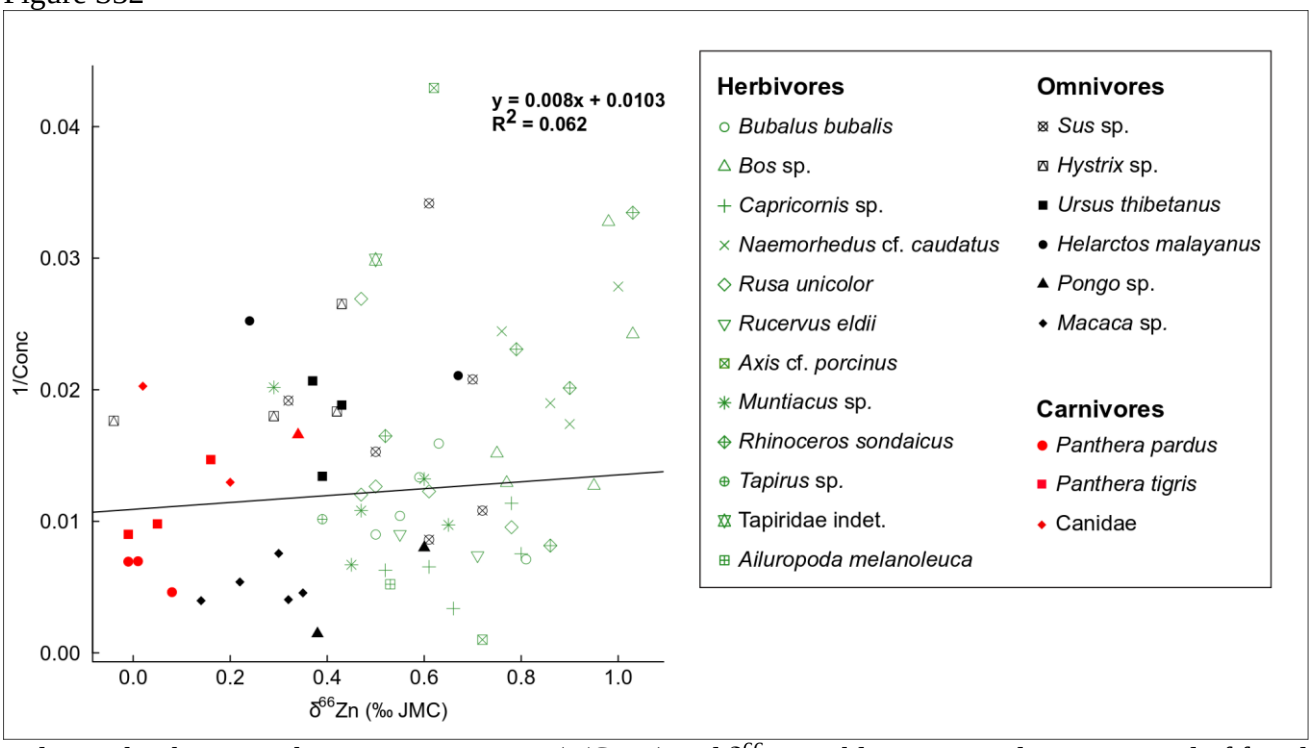

Relationship between the Zn concentration (1/Conc) and δ^{66}Zn stable isotope values in enamel of fossil teeth from Tam Hay Marklot cave.

Figure S33

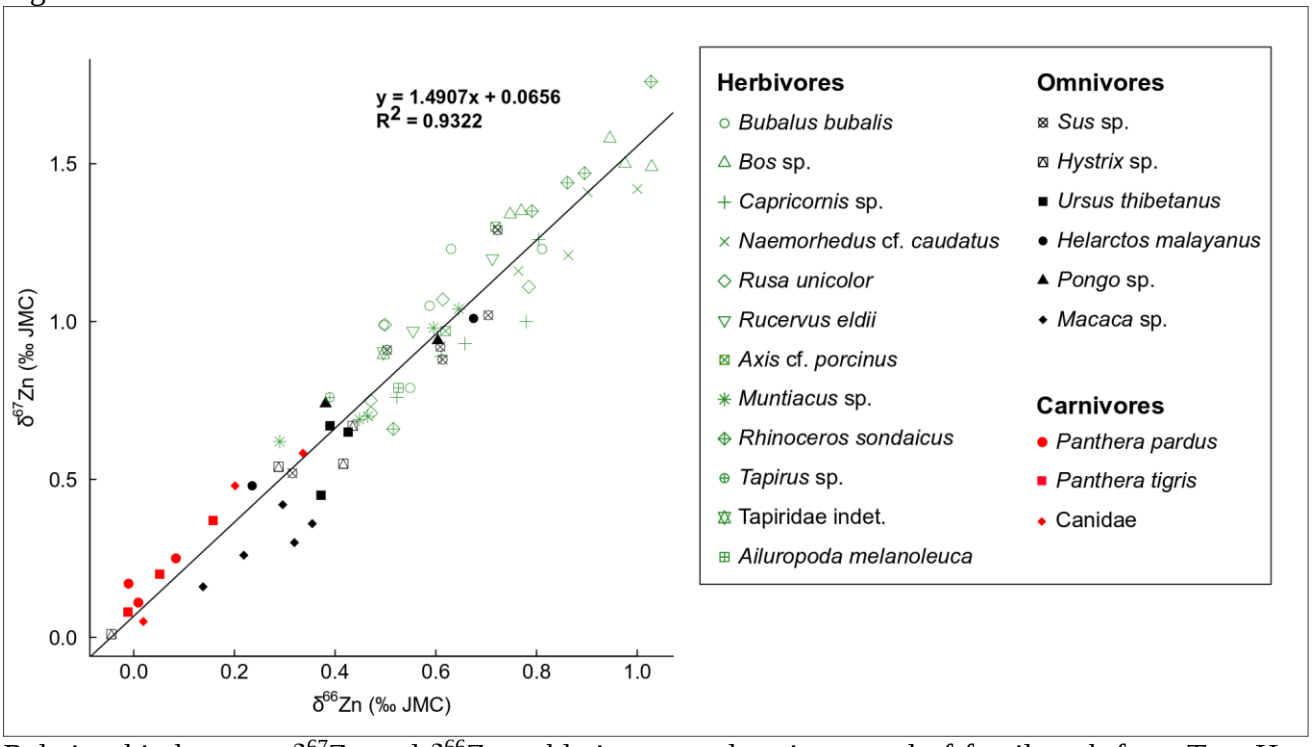

Relationship between δ^{67}Zn and δ^{66}Zn stable isotope values in enamel of fossil teeth from Tam Hay Marklot cave.

Figure S34

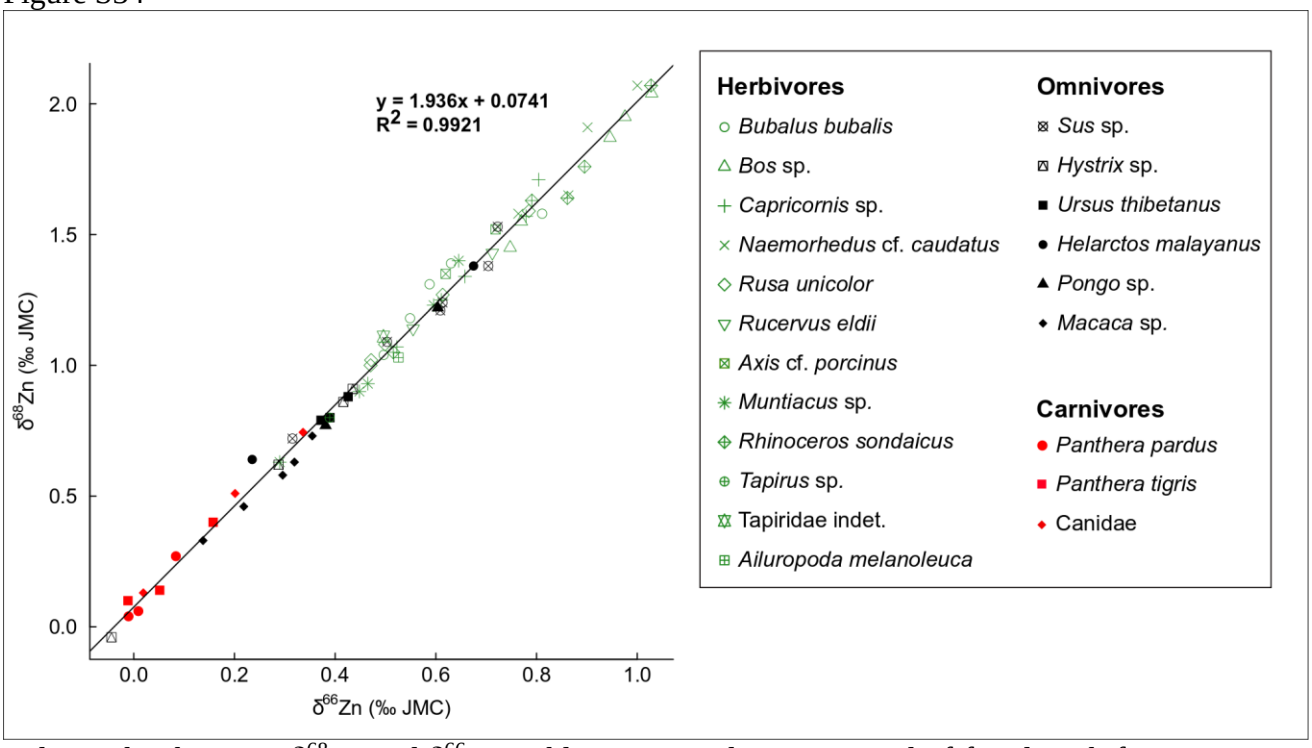

Relationship between $\delta^{68}Zn$ and $\delta^{66}Zn$ stable isotope values in enamel of fossil teeth from Tam Hay Marklot cave.

Figure S35

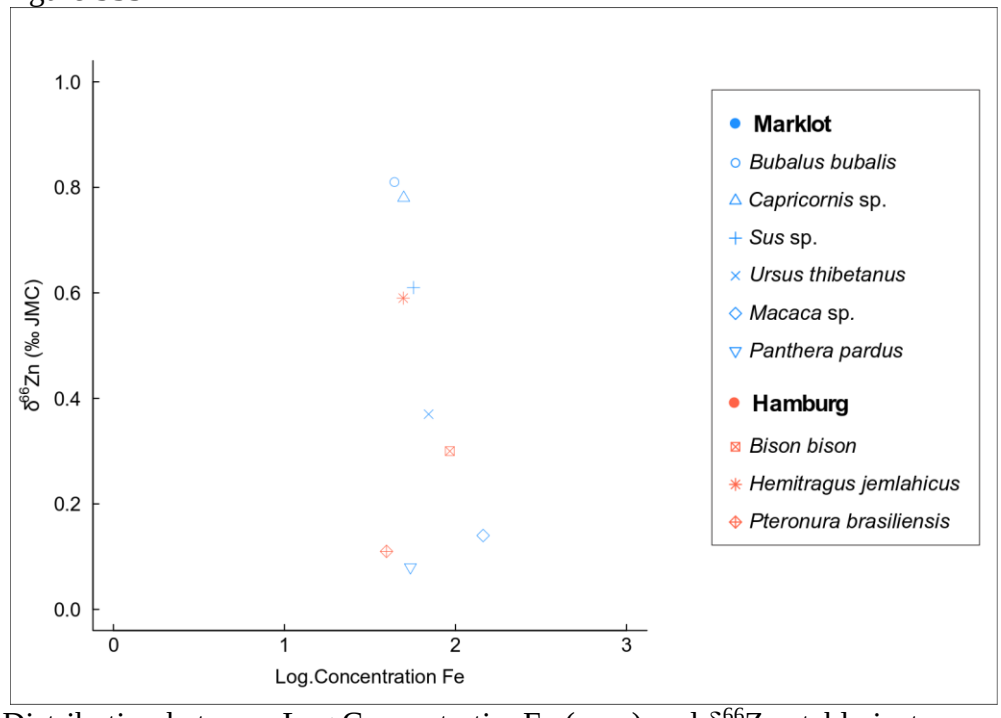

Distribution between Log.ConcentrationFe (ppm) and $\delta^{66}Zn$ stable isotope values in enamel of fossil (Marklot) and modern (Hamburg: Center of Natural History of Hamburg, originally zoo animals from Hagenbeck Tierpark in Hamburg) teeth.

Figure S36

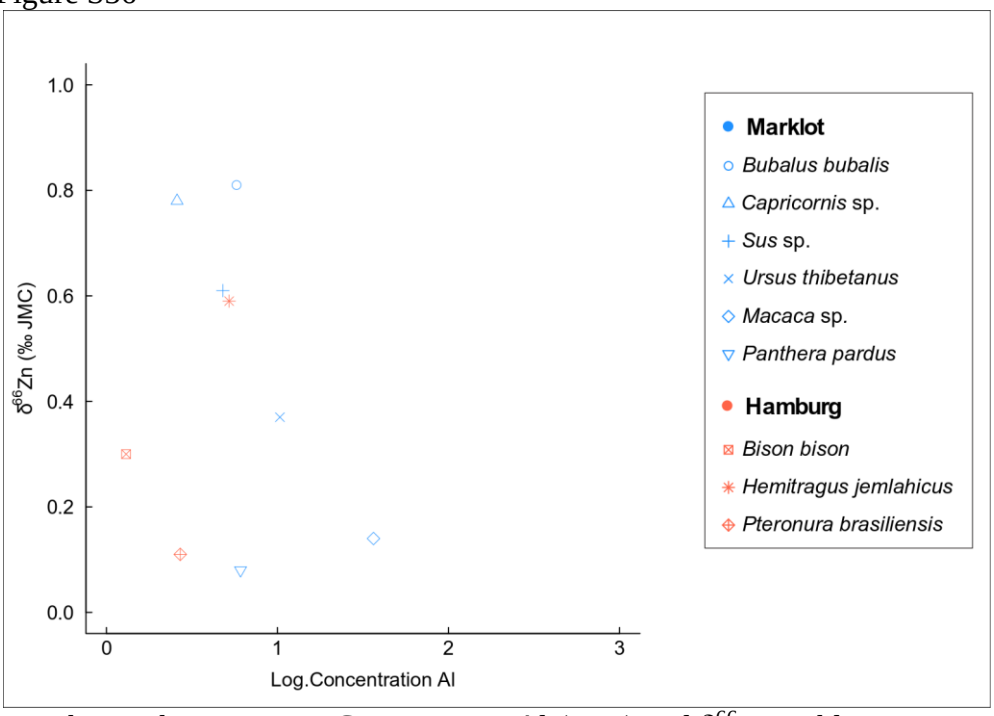

Distribution between Log.ConcentrationAl (ppm) and δ^{66}Zn stable isotope values in enamel of fossil (Marklot) and modern (Hamburg: Center of Natural History of Hamburg, originally zoo animals from Hagenbeck Tierpark in Hamburg) teeth.

Figure S37

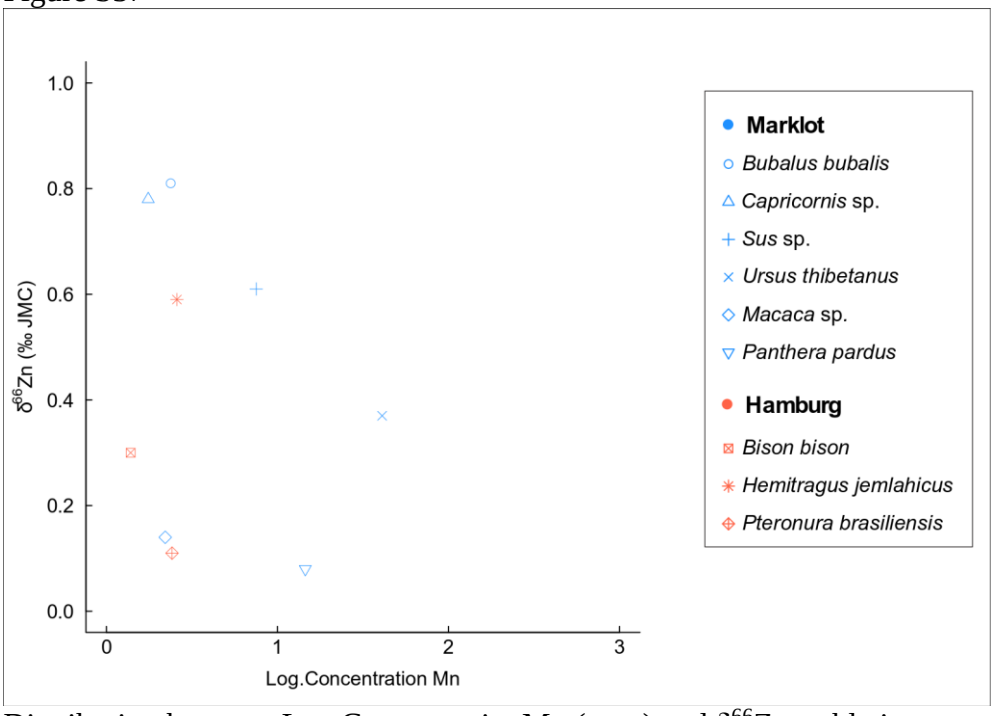

Distribution between Log.ConcentrationMn (ppm) and δ^{66}Zn stable isotope values in enamel of fossil (Marklot) and modern (Hamburg: Center of Natural History of Hamburg, originally zoo animals from Hagenbeck Tierpark in Hamburg) teeth.

Figure S38

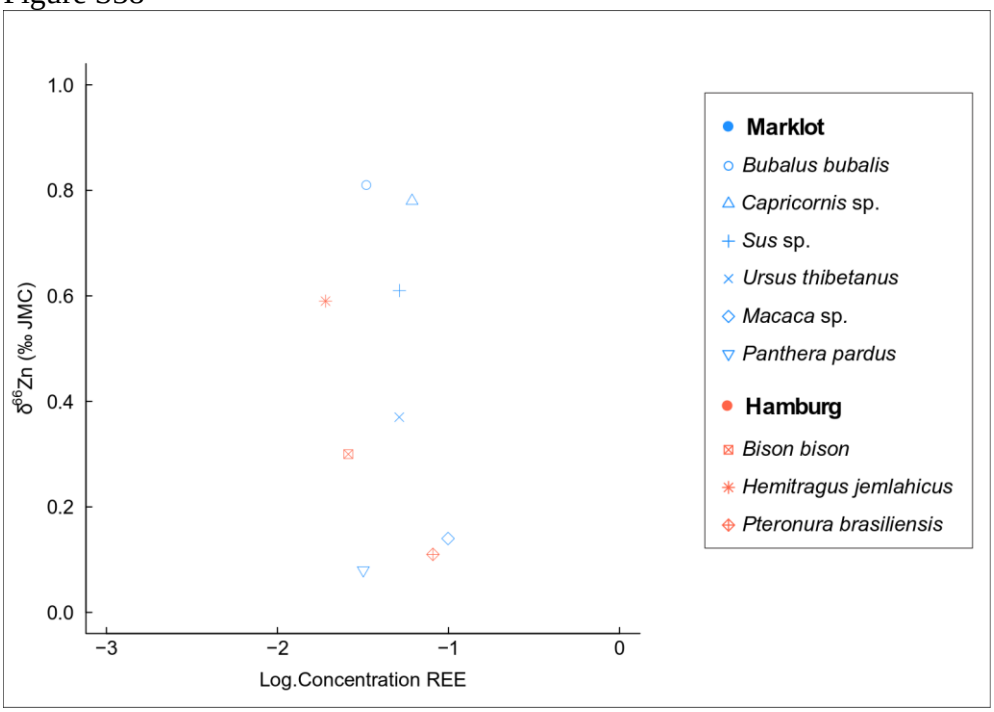

Distribution between Log.ConcentrationREE (ppm; calculated as the sum of all measured REE concentrations) and δ^{66}Zn stable isotope values in enamel of fossil (Marklot) and modern (Hamburg: Center of Natural History of Hamburg, originally zoo animals from Hagenbeck Tierpark in Hamburg) teeth.

Figure S39

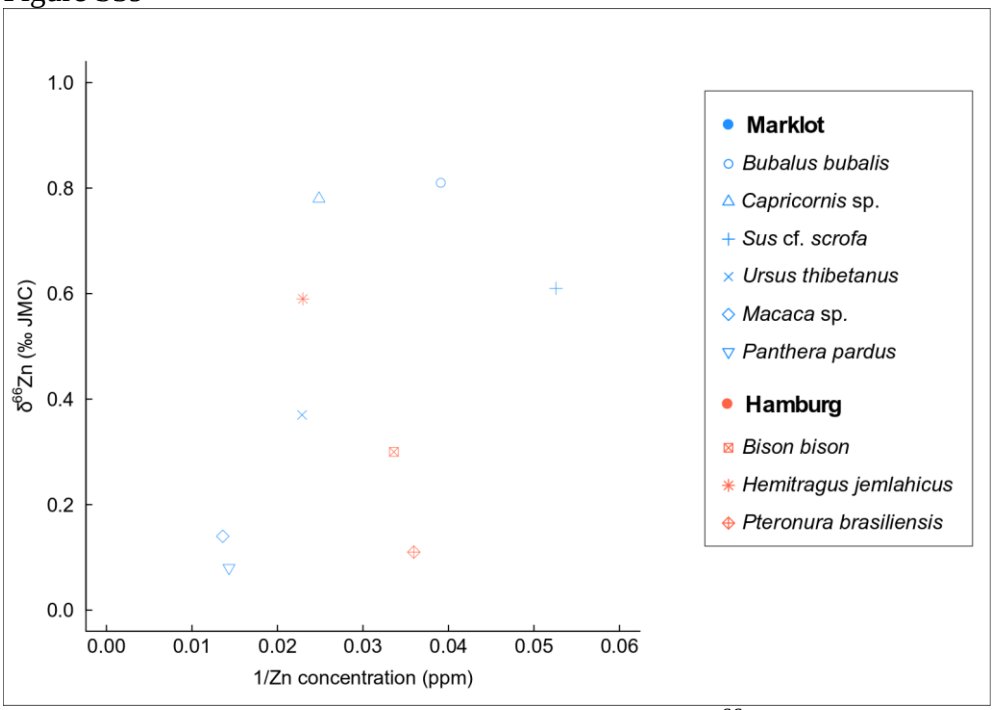

Distribution between the Zn concentration (ppm) and δ^{66}Zn stable isotope values in enamel of fossil (Marklot) and modern (Hamburg: Center of Natural History of Hamburg, originally zoo animals from Hagenbeck Tierpark in Hamburg) teeth.

Figure S40

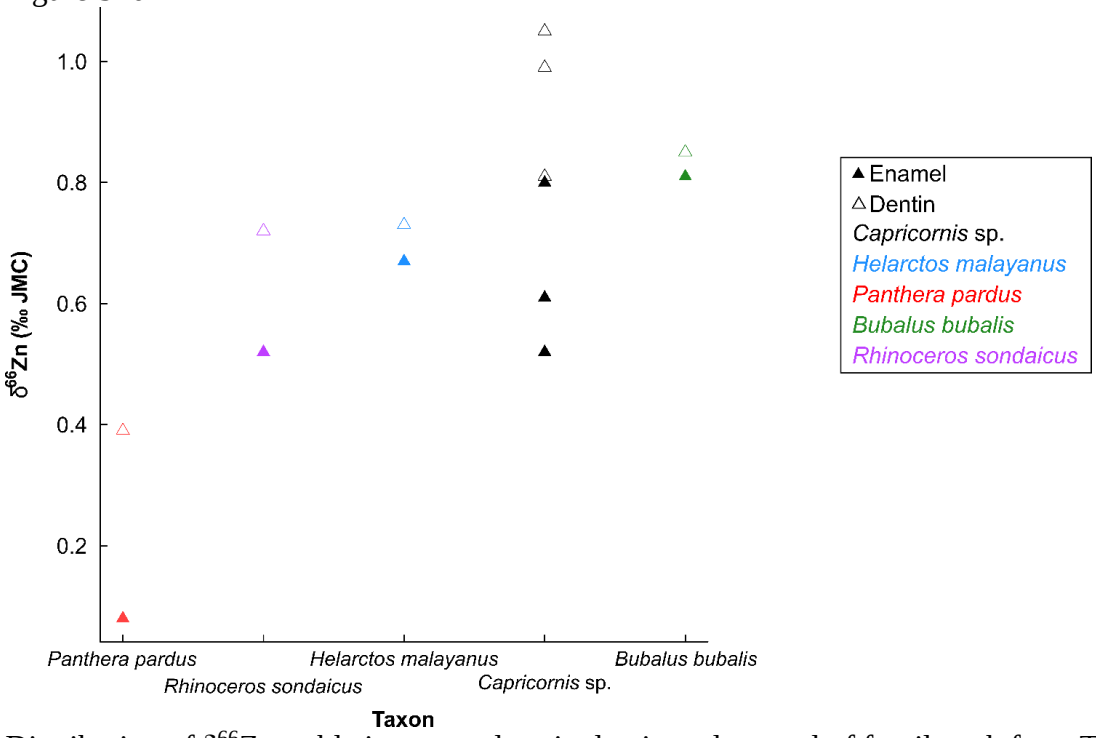

Distribution of δ^{66}Zn stable isotope values in dentin and enamel of fossil teeth from Tam Hay Marklot cave. Fossil teeth from various taxa: *Capricornis* sp. (34489, 34490 and 34492), *Helarctos malayanus* (34498), *Panthera pardus* (34505), *Bubalus bubalis* (34524) and *Rhinoceros sondaicus* (34556) were analyzed. Note that enamel has systematically lower δ^{66}Zn values compared to dentin of the same tooth.

Figure S41

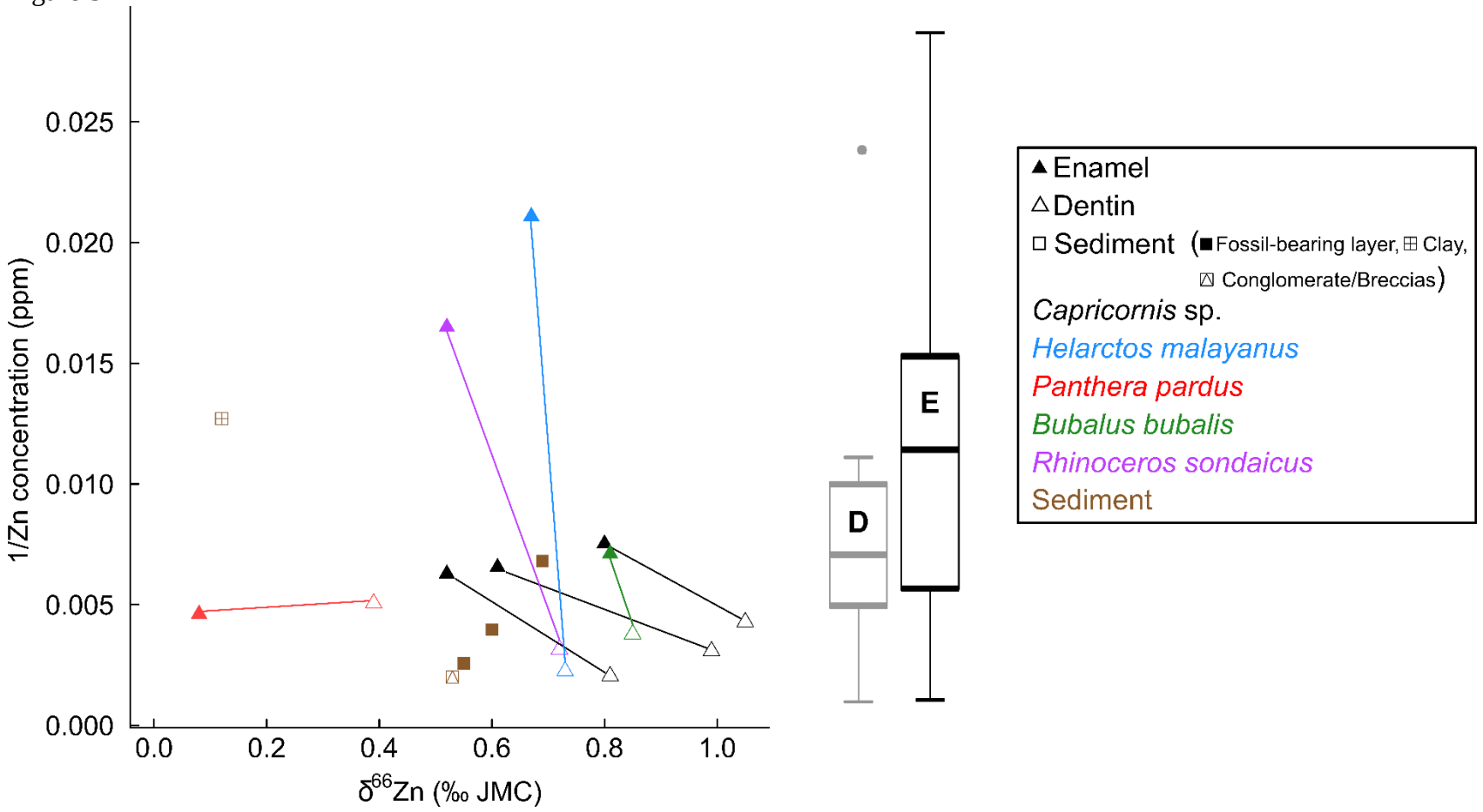

Distribution of Zn concentration (1/Zn concentration (ppm)) and δ^{66}Zn stable isotope values in dentin and enamel of fossil teeth, and sediment from Tam Hay Marklot cave. The line between samples indicate they are from the same specimen. Samples of fossil teeth include specimens from various taxa: *Capricornis* sp. (34489, 34490 and 34492), *Helarctos malayanus* (34498), *Panthera pardus* (34505), *Bubalus bubalis* (34524) and *Rhinoceros sondaicus* (34556). Sediment samples include fossiliferous layer (sandy to gravelly silty clay, with calcitic cementation), conglomerate/breccias from adjacent layer, and clay from the conglomerate). The boxes from the box and whisker plots represent the 25th–75th percentiles, with the median as a bold horizontal line, of Zn concentration from modern dentin (D) and enamel (E) found elsewhere (57, 158–161).

Figure S42

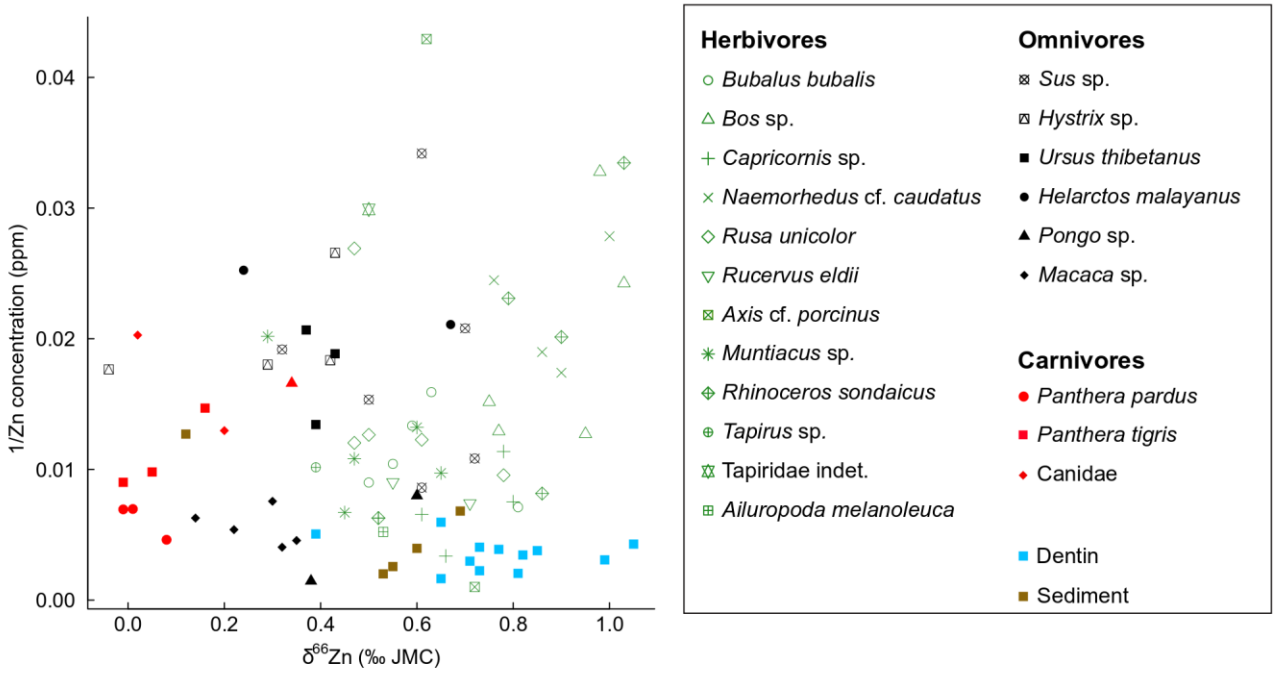

Distribution between the Zn concentration (1/Conc) and δ^{66}Zn stable isotope values in enamel and dentin of fossil teeth and sediment from Tam Hay Marklot cave.

Figure S43

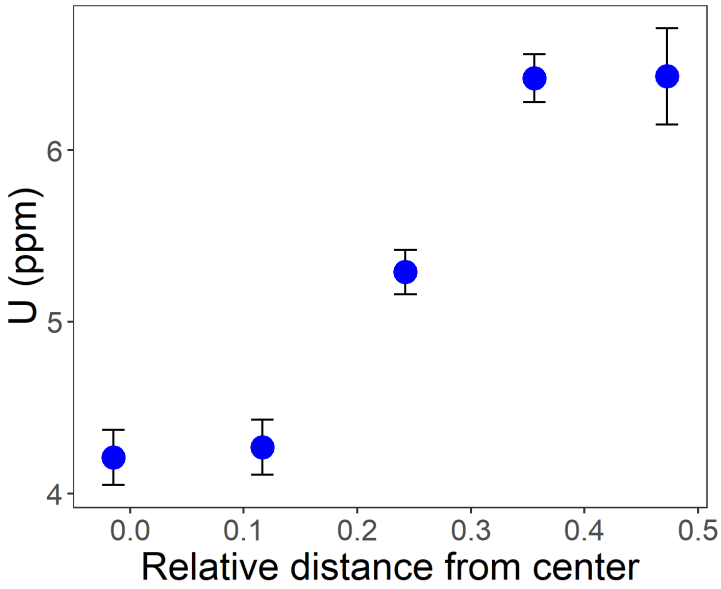

DAD model for the Tam Hay Marklot tooth specimen SCUMK-R1 (*Dicerorhinus sumatrensis*) that was prepared and analyzed for U/Th series dating. Relative distance is calculated from the EDJ to the extremity of the dental tissues between [-1;1], being respectively the enamel tip in contact with the sediment and the pulp cavity.

Figure S44

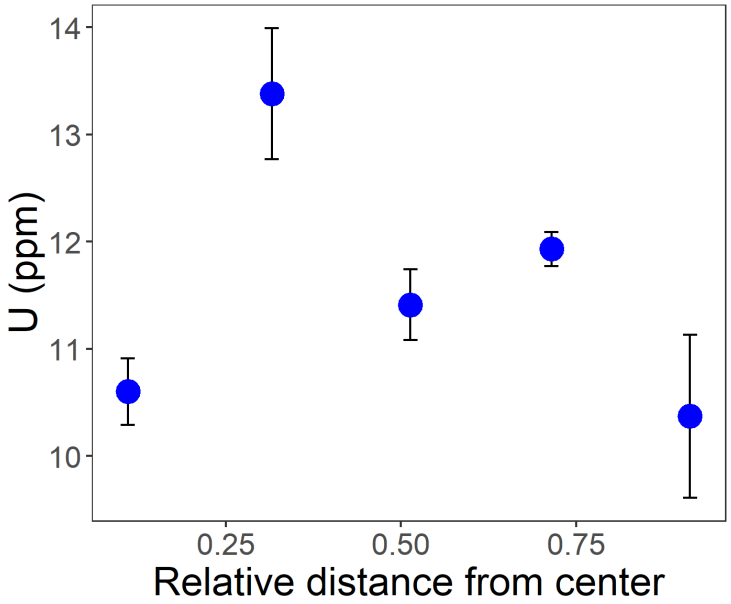

DAD model for the Tam Hay Marklot tooth specimen SCUMK-01 (large Bovid) that was prepared and analyzed for U/Th series dating. Relative distance is calculated from the EDJ to the extremity of the dental tissues between [-1;1], being respectively the enamel tip in contact with the sediment and the pulp cavity.

Figure S45

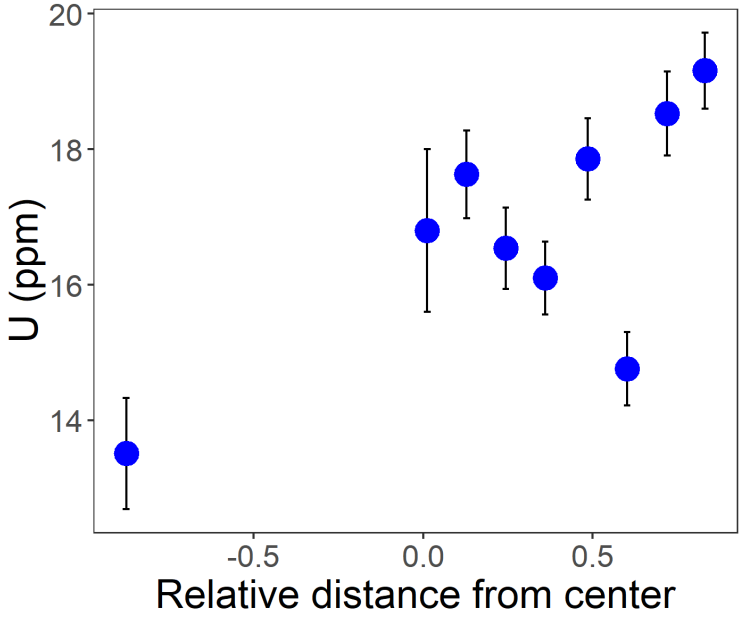

DAD model for the Tam Hay Marklot tooth specimen SCUMK-02 (*Pongo* sp.) that was prepared and analyzed for U/Th series dating. Relative distance is calculated from the EDJ to the extremity of the dental tissues between [-1;1], being respectively the enamel tip in contact with the sediment and the pulp cavity.

Figure S46

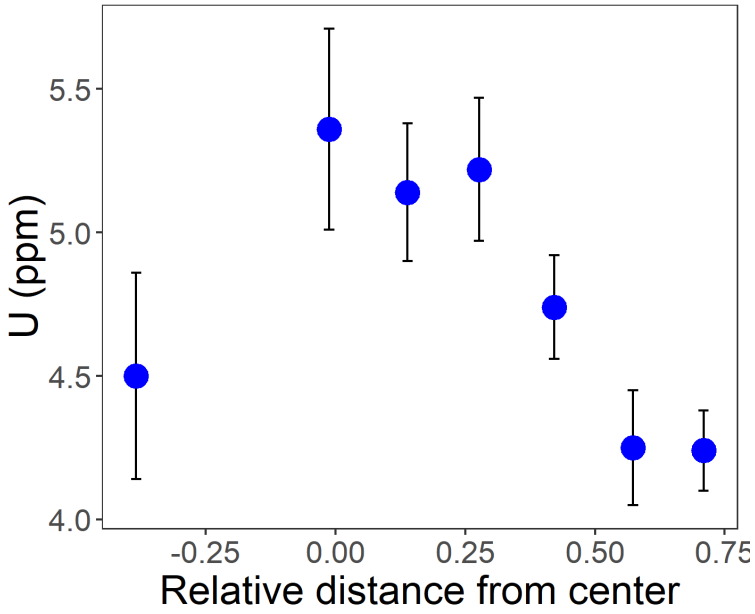

DAD model for the Tam Hay Marklot tooth specimen SCUMK-03A (*Bos* sp. (*Bos* cf. *frontalis*)) that was prepared and analyzed for U/Th series dating. Relative distance is calculated from the EDJ to the extremity of the dental tissues between [-1;1], being respectively the enamel tip in contact with the sediment and the pulp cavity.

Captions

Supplementary table captions

Table S1: Full list of fossil tooth specimens from Tam Hay Marklot cave (Laos) analyzed in this study, with corresponding S-EVA number, original number, broad dietary category and anatomical element. The dietary category assigned to each taxon was taken from [(1)]Nowak 1999, [(2)]Macdonals 2009 and [(3-4)]Johnsingh and Manjrekar 2013, 2015 (116–119).

Table S2: Sediment and dentin $\delta^{66}Zn$ isotope values from Tam Hay Marklot cave (Laos) used to assess the impact of diagenesis on $\delta^{66}Zn$ values.

Table S3: Enamel stable isotope results of $\delta^{13}C_{apatite}$, $\delta^{18}O_{apatite}$, $^{87}Sr/^{86}Sr$ and $\delta^{66}Zn$ from the 72 fossil tooth specimens from Tam Hay Marklot cave (Laos).

Table S4: Dentin $\delta^{13}C$ and $\delta^{15}N$ values from collagen extraction for the four of the 23 of the dentin sub sample, for which collagen extraction was attempted.

Table S5: List of reference materials with their respective measured and expected values for different isotopes.

Table S6: Results of the Linear Mixed Model modelling $\delta^{66}Zn$ values as a function of several predictors (estimates and standard errors, confidence limits of the model, results of likelihood ratio tests, and the range of estimates obtained for the model when dropping levels of random effects one at a time).

Table S7: Inventory of specimens (isolated teeth) of mammals recovered at the Marklot site. N: Total number of specimens.

Table S8: Sample description from fossil teeth of the Tam Hay Marklot assemblage prepared for U-series dating.

Table S9: U-series results for the Tam Hay Marklot tooth specimen SCUMKR1 (*Dicerorhinus sumatrensis*).

Table S10: U-series results for the Tam Hay Marklot tooth specimen SCUMK01 (large Bovid).

Table S11: U-series results for the Tam Hay Marklot tooth specimen SCUMK02 (*Pongo* sp.).

Table S12: U-series results for the Tam Hay Marklot tooth specimen SCUMK03 (*Bos* sp. (*Bos* cf. *frontalis*)).

Table S13: DAD model results for each fossil tooth sample from the Tam Hay Marklot assemblage prepared for U-series dating

Supplementary figure captions

Figure S1: Map of the Indochinese Peninsula with the location of the studied area in northeast Laos.

Figure S2: Map of Laos showing the studied area in the Hua Pan Province, 130 km NNE from Luang Prabang.

Figure S3: Satellite view of the studied area with the location of the cave 6 km SE from the city of Xoneuna (Muang Xon).

Figure S4: (A) Tam Hay Marklot cave at the foot of a tower karst covered by the forest, and (B, C) the first chamber at the entrance. (D, E) First passageway that leads to the gallery.

Figure S5: Map of the entire Tam Hay Marklot cave from the first chamber at the entrance to the dead-end after a 235 m extent, with three views of the gallery.

Figure S6: Map of the Tam Hay Marklot cave showing the three sections of the cave and their sedimentary fillings (see Figure 7 for the legend of sedimentary sections).

Figure S7: Detail of the section/trench 2 showing the main sedimentary facies of the cave. In A and B, the arrows give the direction of the palaeocurrents from inside to outside of the cave.

Figure S8: Distribution of carbon ($\delta^{13}C_{apatite}$) and oxygen ($\delta^{18}O_{apatite}$) stable isotope values in fossil tooth enamel from Tam Hay Marklot cave.

Figure 9: Distribution of carbon ($\delta^{13}C_{collagen}$) and nitrogen ($\delta^{15}N_{collagen}$) stable isotope values in root dentin of the few fossil teeth from Tam Hay Marklot cave with collagen preservation.

Figure S10: Relationship between radiogenic strontium ratios ($^{87}Sr/^{86}Sr$) and zinc ($\delta^{66}Zn$) stable isotope values in enamel of fossil teeth from Tam Hay Marklot cave.

Figure S11: Relationship between the strontium concentration and the radiogenic strontium isotope ratios ($^{87}Sr/^{86}Sr$) in enamel of fossil teeth from Tam Hay Marklot cave. The boxes from the box and whisker plot represent the 25^{th}–75^{th} percentiles, with the median as a bold horizontal line, of Sr concentration from modern enamel of mammal teeth found elsewhere (122, 123, 158).

Figure S12: Spatial element concentration profiles for the element Zn, Fe, Mn, Al, Mg, Sr, Pb, U and rare earth elements (REE, calculated as the sum of all measured REE concentrations) of all LA-ICP-MS linescan analysis (1 to 3) of the Tam Hay Marklot cave fossil tooth (m3 right) specimen 34493 (*Capricornis* sp.). All concentration data (ppm) were log transformed. The different shaded areas, delimited by dotted lines, represent the different histological parts: white for enamel, light gray for dentin and medium gray for pulp cavity. The profiles follow a left-to-right direction as seen from the picture on the left.

Figure S13: Spatial element concentration profiles for the element Zn, Fe, Mn, Al, Mg, Sr, Pb, U and rare earth elements (REE, calculated as the sum of all measured REE concentrations) of all LA-ICP-MS linescan analysis (1 and 2) of the Tam Hay Marklot cave fossil tooth (M2 left) specimen 34501 (*Ursus thibetanus*). All concentration data (ppm) were log transformed. The different shaded areas, delimited by dotted lines, represent the different histological parts: white for enamel, and light gray for dentin. The profiles follow a left-to-right direction as seen from the picture on the left.

Figure S14: Spatial element concentration profiles for the element Zn, Fe, Mn, Al, Mg, Sr, Pb, U and rare earth elements (REE, calculated as the sum of all measured REE concentrations) of all LA-ICP-MS linescan analysis (1 to 3) of the Tam Hay Marklot cave fossil tooth (P4 left) specimen 34505 (*Panthera pardus*). All concentration data (ppm) were log transformed. The different shaded areas, delimited by dotted lines, represent the different histological parts: white for enamel, and light gray for dentin. The profiles follow a left-to-right direction as seen from the picture on the left.

Figure S15: Spatial element concentration profiles for the element Zn, Fe, Mn, Al, Mg, Sr, Pb, U and rare earth elements (REE, calculated as the sum of all measured REE concentrations) of all LA-ICP-MS linescan analysis (1 to 3) of the Tam Hay Marklot cave fossil tooth (p2/p3 left) specimen 34524 (*Bubalus bubalis*). All concentration data (ppm) were log transformed. The different shaded areas, delimited by dotted lines, represent the different histological parts: white for enamel, and light gray for dentin. The profiles follow a left-to-right direction as seen from the picture on the left.

Figure S16 Spatial element concentration profiles for the element Zn, Fe, Mn, Al, Mg, Sr, Pb, U and rare earth elements (REE, calculated as the sum of all measured REE concentrations) of all LA-ICP-MS linescan analysis (1 to 3) of the Tam Hay Marklot cave fossil tooth (p4 left) specimen 34538 (*Sus* sp.). All concentration data (ppm) were log transformed. The different shaded areas, delimited by dotted lines, represent the different histological parts: white for enamel, and light gray for dentin. The profiles follow a left-to-right direction as seen from the picture on the left.

Figure S17: Spatial element concentration profiles for the element Zn, Fe, Mn, Al, Mg, Sr, Pb, U and rare earth elements (REE, calculated as the sum of all measured REE concentrations) of the single LA-

ICP-MS linescan analysis of the Tam Hay Marklot cave fossil tooth (m1/m2 left) specimen 34548 (*Macaca* sp.). All concentration data (ppm) were log transformed. The different shaded areas, delimited by dotted lines, represent the different histological parts: white for enamel, and light gray for dentin. The profiles follow a left-to-right direction as seen from the picture on the left.

Figure S18: Spatial element concentration profiles for the element Zn, Fe, Mn, Al, Mg, Sr, Pb, U and rare earth elements (REE, calculated as the sum of all measured REE concentrations) of all LA-ICP-MS linescan analysis (1 and 2) of the Center of Natural History of Hamburg modern tooth (m3 right) specimen SEVA 34707 / ZMH-S-10461 (*Bison bison*). All concentration data (ppm) were log transformed. The different shaded areas, delimited by dotted lines, represent the different histological parts: white for enamel, light gray for dentin, medium gray for pulp cavity, and dark gray for calculus. The profiles follow a left-to-right direction as seen from the picture on the left.

Figure S19: Spatial element concentration profiles for the element Zn, Fe, Mn, Al, Mg, Sr, Pb, U and rare earth elements (REE, calculated as the sum of all measured REE concentrations) of all LA-ICP-MS linescan analysis (1 to 3) of the Center of Natural History of Hamburg modern tooth (m3 left) specimen SEVA 34708 / ZMH-S-10963 (*Hemitragus jemlahicus*). All concentration data (ppm) were log transformed. The different shaded areas, delimited by dotted lines, represent the different histological parts: white for enamel, light gray for dentin, medium gray for pulp cavity, and dark gray for calculus. The profiles follow a left-to-right direction as seen from the picture on the left.

Figure S20: Spatial element concentration profiles for the element Zn, Fe, Mn, Al, Mg, Sr, Pb, U and rare earth elements (REE, calculated as the sum of all measured REE concentrations) of the single LA-ICP-MS linescan analysis of the Center of Natural History of Hamburg modern tooth (p3/p4) specimen SEVA 34709/ZMH-S-10612 (*Pteronura brasiliensis*). All concentration data (ppm) were log transformed. The different shaded areas, delimited by dotted lines, represent the different histological parts: white for enamel, light gray for dentin, and medium gray for pulp cavity. The profiles follow a left-to-right direction as seen from the picture on the left.

Figure S21: Typical concentrations (ppm) observed through spatial element concentration profiles for the element Zn, Fe, Mn, Al, Mg, Sr, Pb, U and rare earth elements (REE, calculated as the sum of all measured REE concentrations) of the Tam Hay Marklot cave fossil tooth (m3 right) specimen 34493 (*Capricornis* sp.). The different shaded areas, delimited by dotted lines, represent the different histological parts: white for enamel, light gray for dentin, and medium gray for pulp cavity. The profiles follow a left-to-right direction as seen from the picture on the left.

Figure S22: Typical concentrations (ppm) observed through spatial element concentration profiles for the element Zn, Fe, Mn, Al, Mg, Sr, Pb, U and rare earth elements (REE, calculated as the sum of all measured REE concentrations) of the Tam Hay Marklot cave fossil tooth (M2 left) specimen 34501 (*Ursus thibetanus*). All concentration (ppm) were log transformed. The different shaded areas, delimited by dotted lines, represent the different histological parts: white for enamel, and light gray for dentin. The profiles follow a left-to-right direction as seen from the picture on the left.

Figure S23: Typical concentrations (ppm) observed through spatial element concentration profiles for the element Zn, Fe, Mn, Al, Mg, Sr, Pb, U and rare earth elements (REE, calculated as the sum of all measured REE concentrations) of the Tam Hay Marklot cave fossil tooth (P4 left) specimen 34505 (*Panthera pardus*). All concentration (ppm) were log transformed. The different shaded areas, delimited by dotted lines, represent the different histological parts: white for enamel, and light gray for dentin. The profiles follow a left-to-right direction as seen from the picture on the left.

Figure S24: Typical concentrations (ppm) observed through spatial element concentration profiles for the element Zn, Fe, Mn, Al, Mg, Sr, Pb, U and rare earth elements (REE, calculated as the sum of all measured REE concentrations) of the Tam Hay Marklot cave fossil tooth (p2/p3 left) specimen 34524 (*Bubalus bubalis*). All concentration (ppm) were log transformed. The different shaded areas, delimited by dotted lines, represent the different histological parts: white for enamel, and light gray for dentin. The profiles follow a left-to-right direction as seen from the picture on the left.

Figure S25: Typical concentrations (ppm) observed through spatial element concentration profiles for the element Zn, Fe, Mn, Al, Mg, Sr, Pb, U and rare earth elements (REE, calculated as the sum of all measured REE concentrations) of the Tam Hay Marklot cave fossil tooth (p4 left) specimen 34538 (*Sus* sp.). All concentration (ppm) were log transformed. The different shaded areas, delimited by dotted lines, represent the different histological parts: white for enamel, and light gray for dentin. The profiles follow a left-to-right direction as seen from the picture on the left.

Figure S26: Typical concentrations (ppm) observed through spatial element concentration profiles for the element Zn, Fe, Mn, Al, Mg, Sr, Pb, U and rare earth elements (REE, calculated as the sum of all measured REE concentrations) of the Tam Hay Marklot cave fossil tooth (m1/m2 left) specimen 34548 (*Macaca* sp.). All concentration (ppm) were log transformed. The different shaded areas, delimited by dotted lines, represent the different histological parts: white for enamel, and light gray for dentin. The profiles follow a left-to-right direction as seen from the picture on the left.

Figure S27: Typical concentrations (ppm) observed through spatial element concentration profiles for the element Zn, Fe, Mn, Al, Mg, Sr, Pb, U and rare earth elements (REE, calculated as the sum of all measured REE concentrations) of the Center of Natural History of Hamburg modern tooth (m3 right) specimen SEVA 34707 / ZMH-S-10461 (*Bison bison*). All concentration (ppm) were log transformed. The different shaded areas, delimited by dotted lines, represent the different histological parts: white for enamel, light gray for dentin, and medium gray for pulp cavity. The profiles follow a left-to-right direction as seen from the picture on the left.

Figure S28: Typical concentrations (ppm) observed through spatial element concentration profiles for the element Zn, Fe, Mn, Al, Mg, Sr, Pb, U and rare earth elements (REE, calculated as the sum of all measured REE concentrations) of the Center of Natural History of Hamburg modern tooth (m3 left) specimen SEVA 34708 / ZMH-S-10963 (*Hemitragus jemlahicus*). All concentration (ppm) were log transformed. The different shaded areas, delimited by dotted lines, represent the different histological parts: white for enamel, light gray for dentin, medium gray for pulp cavity, and dark gray for calculus. The profiles follow a left-to-right direction as seen from the picture on the left.

Figure S29: Typical concentrations (ppm) observed through spatial element concentration profiles for the element Zn, Fe, Mn, Al, Mg, Sr, Pb, U and rare earth elements (REE, calculated as the sum of all measured REE concentrations) of the Center of Natural History of Hamburg modern tooth (p3/p4) specimen SEVA 34709/ZMH-S-10612 (*Pteronura brasiliensis*). All concentration (ppm) were log transformed. The different shaded areas, delimited by dotted lines, represent the different histological parts: white for enamel, light gray for dentin, and medium gray for pulp cavity. The profiles follow a left-to-right direction as seen from the picture on the left.

Figure 30: Zn concentration (ppm) distribution of every analyzed fossil enamel cross section segment, normalized to the relative enamel thickness (0% = outermost enamel layer, 100% = full thickness prior to analysis of enamel-dentin mixture). The gray area represents the concentration range observed in modern enamel cross section segments, colored lines those of the fossil enamel.

Figure S31: Relationship between $\delta^{15}N_{collagen}$ and $\delta^{66}Zn_{enamel}$ stable isotope values in fossil teeth from Tam Hay Marklot cave that yielded collagen from the dentin.

Figure S32: Relationship between the Zn concentration (1/Conc) and $\delta^{66}Zn$ stable isotope values in enamel of fossil teeth from Tam Hay Marklot cave.

Figure S33: Relationship between $\delta^{67}Zn$ and $\delta^{66}Zn$ stable isotope values in enamel of fossil teeth from Tam Hay Marklot cave.

Figure S34: Relationship between $\delta^{68}Zn$ and $\delta^{66}Zn$ stable isotope values in enamel of fossil teeth from Tam Hay Marklot cave.

Figure S35: Distribution between Log.ConcentrationFe (ppm) and $\delta^{66}Zn$ stable isotope values in enamel of fossil (Marklot) and modern (Hamburg: Center of Natural History of Hamburg, originally zoo animals from Hagenbeck Tierpark in Hamburg) teeth.

Figure S36: Distribution between Log.ConcentrationAl (ppm) and $\delta^{66}Zn$ stable isotope values in enamel of fossil (Marklot) and modern (Hamburg: Center of Natural History of Hamburg, originally zoo animals from Hagenbeck Tierpark in Hamburg) teeth.

Figure S37: Distribution between Log.ConcentrationMn (ppm) and $\delta^{66}Zn$ stable isotope values in enamel of fossil (Marklot) and modern (Hamburg: Center of Natural History of Hamburg, originally zoo animals from Hagenbeck Tierpark in Hamburg) teeth.

Figure S38: Distribution between Log.ConcentrationREE (ppm) and $\delta^{66}Zn$ stable isotope values in enamel of fossil (Marklot) and modern (Hamburg: Center of Natural History of Hamburg, originally zoo animals from Hagenbeck Tierpark in Hamburg) teeth.

Figure S39: Distribution between the Zn concentration (ppm) and $\delta^{66}Zn$ stable isotope values in enamel of fossil (Marklot) and modern (Hamburg: Center of Natural History of Hamburg, originally zoo animals from Hagenbeck Tierpark in Hamburg) teeth.

Figure S40: Distribution of $\delta^{66}Zn$ stable isotope values in dentin and enamel of fossil teeth from Tam Hay Marklot cave. Fossil teeth from various taxa: *Capricornis* sp. (34489, 34490 and 34492), *Helarctos malayanus* (34498), *Panthera pardus* (34505), *Bubalus bubalis* (34524) and *Rhinoceros sondaicus* (34556) were analyzed. Note that enamel has systematically lower $\delta^{66}Zn$ values compared to dentin of the same tooth.

Figure S41: Distribution of Zn concentration (1/Zn concentration (ppm)) and $\delta^{66}Zn$ stable isotope values in dentin and enamel of fossil teeth, and sediment from Tam Hay Marklot cave. The line between samples indicate they are from the same specimen. Samples of fossil teeth include specimens from various taxa: *Capricornis* sp. (34489, 34490 and 34492), *Helarctos malayanus* (34498), *Panthera pardus* (34505), *Bubalus bubalis* (34524) and *Rhinoceros sondaicus* (34556). Sediment samples include fossiliferous layer (sandy to gravelly silty clay, with calcitic cementation), conglomerate/breccias from adjacent layer, and clay from the conglomerate). The boxes from the box and whisker plots represent the 25^{th}–75^{th} percentiles, with the median as a bold horizontal line, of Zn concentration from modern dentin (D) and enamel (E) found elsewhere (2–6).

Figure S42: Distribution between the Zn concentration (1/Conc) and $\delta^{66}Zn$ stable isotope values in enamel and dentin of fossil teeth and sediment from Tam Hay Marklot cave.

Figure S43: DAD model for the Tam Hay Marklot specimen SCUMK-R1 (*Dicerorhinus sumatrensis*) that was prepared and analyzed for U/Th series dating. Relative distance is calculated from the EDJ to the extremity of the dental tissues between [-1;1], being respectively the enamel tip in contact with the sediment and the pulp cavity.

Figure S44: DAD model for the Tam Hay Marklot specimen SCUMK-01 (large Bovid) that was prepared and analyzed for U/Th series dating. Relative distance is calculated from the EDJ to the extremity of the dental tissues between [-1;1], being respectively the enamel tip in contact with the sediment and the pulp cavity.

Figure S45: DAD model for the Tam Hay Marklot specimen SCUMK-02 (*Pongo* sp.) that was prepared and analyzed for U/Th series dating. Relative distance is calculated from the EDJ to the extremity of the dental tissues between [-1;1], being respectively the enamel tip in contact with the sediment and the pulp cavity.

Figure S46: DAD model for the Tam Hay Marklot specimen SCUMK-03A (*Bos* sp. (*Bos* cf. *frontalis*)) that was prepared and analyzed for U/Th series dating. Relative distance is calculated from the EDJ to the extremity of the dental tissues between [-1;1], being respectively the enamel tip in contact with the sediment and the pulp cavity.

Supplementary information references

1. E. Saurin, Carte géologique du Laos, feuille Luang Prabang Est (1961).
2. P. Duringer, A.-M. Bacon, T. Sayavongkhamdy, T. K. T. Nguyen, Karst development, breccias history, and mammalian assemblages in Southeast Asia: A brief review. *Comptes Rendus Palevol* **11**, 133–157 (2012).
3. K. Suraprasit, *et al.*, The Middle Pleistocene vertebrate fauna from Khok Sung (Nakhon Ratchasima, Thailand): biochronological and paleobiogeographical implications. *Zookeys*, 1–157 (2016).
4. C. Tougard, "Les faunes de grands mammifères du Pléistocène moyen terminal de Thaïlande dans leur cadre phylogénétique, paléoécologique et biochronologique.," Université de Montpellier II. (1998).
5. A. Filoux, A. Wattanapituksakul, C. Lespes, C. Thongcharoenchaikit, A Pleistocene mammal assemblage containing Ailuropoda and Pongo from Tham Prakai Phet cave, Chaiyaphum Province, Thailand. *Geobios* **48**, 341–349 (2015).
6. A.-M. Bacon, *et al.*, The Late Pleistocene Duoi U'Oi cave in northern Vietnam: palaeontology, sedimentology, taphonomy and palaeoenvironments. *Quaternary Science Reviews* **27**, 1627–1654 (2008).
7. A.-M. Bacon, *et al.*, The Middle Pleistocene mammalian fauna from Tam Hang karstic deposit, northern Laos: New data and evolutionary hypothesis. *Quaternary International* **245**, 315–332 (2011).
8. A.-M. Bacon, *et al.*, A rhinocerotid-dominated megafauna at the MIS6-5 transition: The late Middle Pleistocene Coc Muoi assemblage, Lang Son province, Vietnam. *Quaternary Science Reviews* **186**, 123–141 (2018).
9. A.-M. Bacon, *et al.*, Testing the savannah corridor hypothesis during MIS2: The Boh Dambang hyena site in southern Cambodia. *Quaternary International* **464**, 417–439 (2018).
10. D. M. Badoux, "Fossil mammals from two deposits at Punung (Java)," Utrecht University (Kemink en Zoon, N.V). (1959).
11. Heintz, Les Cervidés villafranchiens de France et d'Espagne. *Mémoires du Muséum National d'Histoire Naturelle*, 1–206 (1970).
12. E. H. Colbert, D. A. Hooijer, Pleistocene mammals from the limestone fissures of Szechwan, China. *Bulletin of the American Museum of Natural History*, 7–134 (1953).
13. J. de Vos, V. T. Long, "Systematic discussion of the Lang Trang fauna" (Unpublished report, 1993).
14. M. Takai, Y. Zhang, R. T. Kono, C. Jin, Changes in the composition of the Pleistocene primate fauna in southern China. *Quaternary International* **354**, 75–85 (2014).
15. T. Harrison, C. Jin, Y. Zhang, Y. Wang, M. Zhu, Fossil Pongo from the Early Pleistocene Gigantopithecus fauna of Chongzuo, Guangxi, southern China. *Quaternary International* **354**, 59–67 (2014).
16. D. J. van Weers, A taxonomic revision of the Pleistocene Hystrix (Hystricidae, Rodentia) from Eurasia with notes on the evolution of the family. *Contributions to Zoology* **74**, 301–312 (2005).
17. R. Grün, S. Eggins, L. Kinsley, H. Moseley, M. Sambridge, Laser ablation U-series analysis of fossil bones and teeth. *Palaeogeography, Palaeoclimatology, Palaeoecology* **416**, 150–167 (2014).
18. C. D. Woodroffe, S. A. Short, D. R. Stoddart, T. Spencer, R. S. Harmon, Stratigraphy and Chronology of Late Pleistocene Reefs in the Southern Cook Islands, South Pacific. *Quaternary Research* **35**, 246–263 (1991).
19. S. Eggins, R. Grün, A. W. G. Pike, M. Shelley, L. Taylor, ^{238}U, ^{232}Th profiling and U-series isotope analysis of fossil teeth by laser ablation-ICPMS. *Quaternary Science Reviews* **22**, 1373–1382 (2003).

20. M. J. DeNiro, S. Epstein, Influence of diet on the distribution of carbon isotopes in animals. *Geochimica et Cosmochimica Acta* **42**, 495–506 (1978).
21. T. McConnaughey, C. P. McRoy, Food-web structure and the fractionation of carbon isotopes in the bering sea. *Mar. Biol.* **53**, 257–262 (1979).
22. M. J. Deniro, S. Epstein, Influence of diet on the distribution of nitrogen isotopes in animals. *Geochimica et Cosmochimica Acta* **45**, 341–351 (1981).
23. M. J. Schoeninger, M. J. DeNiro, Nitrogen and carbon isotopic composition of bone collagen from marine and terrestrial animals. *Geochimica et Cosmochimica Acta* **48**, 625–639 (1984).
24. J. F. Kelly, Stable isotopes of carbon and nitrogen in the study of avian and mammalian trophic ecology. *Can. J. Zool.* **78**, 1–27 (2000).
25. M. P. Richards, P. B. Pettitt, M. C. Stiner, E. Trinkaus, Stable isotope evidence for increasing dietary breadth in the European mid-Upper Paleolithic. *PNAS* **98**, 6528–6532 (2001).
26. J. A. Lee-Thorp, J. C. Sealy, N. J. van der Merwe, Stable carbon isotope ratio differences between bone collagen and bone apatite, and their relationship to diet. *Journal of Archaeological Science* **16**, 585–599 (1989).
27. Y. Wang, T. E. Cerling, A model of fossil tooth and bone diagenesis: implications for paleodiet reconstruction from stable isotopes. *Palaeogeography, Palaeoclimatology, Palaeoecology* **107**, 281–289 (1994).
28. M. J. Kohn, M. J. Schoeninger, W. W. Barker, Altered states: effects of diagenesis on fossil tooth chemistry. *Geochimica et Cosmochimica Acta* **63**, 2737–2747 (1999).
29. J. A. Lee- Thorp, On Isotopes and Old Bones. *Archaeometry* **50**, 925–950 (2008).
30. M. Sponheimer, J. A. Lee-Thorp, Oxygen isotopes in enamel carbonate and their ecological significance. *Journal of Archaeological Science* **26**, 723–728 (1999).
31. T. E. Cerling, J. M. Harris, Carbon isotope fractionation between diet and bioapatite in ungulate mammals and implications for ecological and paleoecological studies. *Oecologia* **120**, 347–363 (1999).
32. M. J. Kohn, T. E. Cerling, Stable isotope compositions of biological apatite. *Reviews in Mineralogy and Geochemistry* **48**, 455–488 (2002).
33. S. Hillson, *Dental Anthropology* (Cambridge University Press, 1996).
34. A. Nanci, *Ten Cate's Oral Histology: Development, Structure, and Function* (Elsevier Health Sciences, 2017).
35. K. J. R. Rosman, P. D. P. Taylor, Isotopic compositions of the elements 1997 (Technical Report). *Pure and Applied Chemistry* **70**, 217–235 (1998).
36. E. Ponzevera, *et al.*, Mass discrimination during MC-ICPMS isotopic ratio measurements: Investigation by means of synthetic isotopic mixtures (IRMM-007 series) and application to the calibration of natural-like zinc materials (including IRMM-3702 and IRMM-651). *The official journal of The American Society for Mass Spectrometry* **17**, 1413–1427 (2006).
37. B. L. Vallee, K. H. Falchuk, The biochemical basis of zinc physiology. *Physiological Reviews* **73**, 79–118 (1993).
38. J. M. Berg, Y. Shi, The galvanization of biology: A growing appreciation for the roles of zinc. *Science* **271**, 1081–1085 (1996).
39. J. Viers, *et al.*, Evidence of Zn isotopic fractionation in a soil–plant system of a pristine tropical watershed (Nsimi, Cameroon). *Chemical Geology* **239**, 124–137 (2007).
40. Z. Fekiacova, S. Cornu, S. Pichat, Tracing contamination sources in soils with Cu and Zn isotopic ratios. *Science of The Total Environment* **517**, 96–105 (2015).
41. D. J. Weiss, *et al.*, Isotopic discrimination of zinc in higher plants. *New Phytologist* **165**, 703–710 (2005).
42. F. Moynier, *et al.*, Isotopic fractionation and transport mechanisms of Zn in plants. *Chemical Geology* **267**, 125–130 (2009).

43. A. M. Aucour, S. Pichat, M. R. Macnair, P. Oger, Fractionation of stable zinc isotopes in the zinc hyperaccumulator Arabidopsis halleri and nonaccumulator Arabidopsis petraea. *Environ. Sci. Technol.* **45**, 9212–9217 (2011).
44. J. Viers, *et al.*, Zn isotope fractionation in a pristine larch forest on permafrost-dominated soils in Central Siberia. *Geochemical Transactions* **16**, 3 (2015).
45. F. Moynier, D. Vance, T. Fujii, P. Savage, The Isotope geochemistry of zinc and copper. *Reviews in Mineralogy and Geochemistry* **82**, 543–600 (2017).
46. C. N. Maréchal, E. Nicolas, C. Douchet, F. Albarède, Abundance of zinc isotopes as a marine biogeochemical tracer. *Geochemistry, Geophysics, Geosystems* **1** (2000).
47. C. Cloquet, J. Carignan, M. F. Lehmann, F. Vanhaecke, Variation in the isotopic composition of zinc in the natural environment and the use of zinc isotopes in biogeosciences: a review. *Anal Bioanal Chem* **390**, 451–463 (2008).
48. J.-M. Luck, D. Ben Othman, F. Albarède, P. Telouk, "Pb, Zn and Cu isotopic variations and trace elements in rain." in *Geochemistry of the Earth's Surface*, (CRC Press, 1999), pp. 199–203.
49. S. Pichat, C. Douchet, F. Albarède, Zinc isotope variations in deep-sea carbonates from the eastern equatorial Pacific over the last 175 ka. *Earth and Planetary Science Letters* **210**, 167–178 (2003).
50. K. Jaouen, M.-L. Pons, V. Balter, Iron, copper and zinc isotopic fractionation up mammal trophic chains. *Earth and Planetary Science Letters* **374**, 164–172 (2013).
51. K. Jaouen, E. Herrscher, V. Balter, Copper and zinc isotope ratios in human bone and enamel. *Am. J. Phys. Anthropol.* **162**, 491–500 (2017).
52. F. Moynier, T. Fujii, A. S. Shaw, M. L. Borgne, Heterogeneous distribution of natural zinc isotopes in mice. *Metallomics* **5**, 693–699 (2013).
53. V. Balter, *et al.*, Bodily variability of zinc natural isotope abundances in sheep. *Rapid Communications in Mass Spectrometry* **24**, 605–612 (2010).
54. R. J. Cousins, Absorption, transport, and hepatic metabolism of copper and zinc: special reference to metallothionein and ceruloplasmin. *Physiological Reviews* **65**, 238–309 (1985).
55. J. R. Turnlund, J. C. King, W. R. Keyes, B. Gong, M. C. Michel, A stable isotope study of zinc absorption in young men: effects of phytate and a-cellulose. *Am J Clin Nutr* **40**, 1071–1077 (1984).
56. B. Lönnerdal, Dietary factors influencing zinc absorption. *J Nutr* **130**, 1378S-1383S (2000).
57. K. Jaouen, M. Beasley, M. Schoeninger, J.-J. Hublin, M. P. Richards, Zinc isotope ratios of bones and teeth as new dietary indicators: results from a modern food web (Koobi Fora, Kenya). *Scientific Reports* **6**, srep26281 (2016).
58. M. Costas-Rodríguez, L. Van Heghe, F. Vanhaecke, Evidence for a possible dietary effect on the isotopic composition of Zn in blood via isotopic analysis of food products by multi-collector ICP-mass spectrometry. *Metallomics* **6**, 139–146 (2014).
59. K. Jaouen, P. Szpak, M. P. Richards, Zinc isotope ratios as indicators of diet and trophic level in arctic marine mammals. *PLoS ONE* **11**, e0152299 (2016).
60. K. Jaouen, *et al.*, Tracing intensive fish and meat consumption using Zn isotope ratios: Evidence from a historical Breton population (Rennes, France). *Scientific Reports* **8**, 5077 (2018).
61. E. J. Dasch, Strontium isotopes in weathering profiles, deep-sea sediments, and sedimentary rocks. *Geochimica et Cosmochimica Acta* **33**, 1521–1552 (1969).
62. R. W. Hurst, T. E. Davis, Strontium isotopes as tracers of airborne fly ash from coal-fired power plants. *Geo* **3**, 363–367 (1981).
63. L. T. Steadman, F. Brudevold, F. A. Smith, Distribution of strontium in teeth from different geographic areas. *The Journal of the American Dental Association* **57**, 340–344 (1958).
64. J. R. Gosz, D. G. Brookins, D. I. Moore, Using strontium isotope ratios to estimate inputs to ecosystems. *BioScience* **33**, 23–30 (1983).
65. P. L. Koch, Isotopic reconstruction of past continental environments. *Annual Review of Earth and Planetary Sciences* **26**, 573–613 (1998).

66. G. Åberg, The use of natural strontium isotopes as tracers in environmental studies. *Water Air Soil Pollut* **79**, 309–322 (1995).
67. J. E. Ericson, Strontium isotope characterization in the study of prehistoric human ecology. *Journal of Human Evolution* **14**, 503–514 (1985).
68. M. Balasse, Reconstructing dietary and environmental history from enamel isotopic analysis: Time resolution of intra-tooth sequential sampling. *Int. J. Osteoarchaeol.* **12**, 155–165 (2002).
69. R. A. Bentley, Strontium isotopes from the earth to the archaeological skeleton: A review. *J Archaeol Method Theory* **13**, 135–187 (2006).
70. C. H. Sullivan, H. W. Krueger, Carbon isotope analysis of separate chemical phases in modern and fossil bone. *Nature* **292**, 333–335 (1981).
71. A. Longinelli, Oxygen isotopes in mammal bone phosphate: A new tool for paleohydrological and paleoclimatological research? *Geochimica et Cosmochimica Acta* **48**, 385–390 (1984).
72. B. Luz, Y. Kolodny, M. Horowitz, Fractionation of oxygen isotopes between mammalian bone-phosphate and environmental drinking water. *Geochimica et Cosmochimica Acta* **48**, 1689–1693 (1984).
73. B. H. Passey, *et al.*, Carbon isotope fractionation between diet, breath CO_2, and bioapatite in different mammals. *Journal of Archaeological Science* **32**, 1459–1470 (2005).
74. B. N. Smith, S. Epstein, Two categories of $^{13}C/^{12}C$ ratios for higher plants. *Plant Physiology* **47**, 380–384 (1971).
75. M. H. O'Leary, Carbon isotopes in photosynthesis fractionation techniques may reveal new aspects of carbon dynamics in plants. *BioScience* **38**, 328–336 (1988).
76. G. D. Farquhar, J. R. Ehleringer, K. T. Hubick, Carbon isotope discrimination and photosynthesis. *Annual Review of Plant Physiology and Plant Molecular Biology* **40**, 503–537 (1989).
77. M. Sponheimer, *et al.*, Do "savanna" chimpanzees consume C_4 resources? *Journal of Human Evolution* **51**, 128–133 (2006).
78. D. Codron, *et al.*, The confounding effects of source isotopic heterogeneity on consumer–diet and tissue–tissue stable isotope relationships. *Oecologia* **169**, 939–953 (2012).
79. A. Zazzo, *et al.*, Herbivore paleodiet and paleoenvironmental changes in Chad during the Pliocene using stable isotope ratios of tooth enamel carbonate. *Paleobiology* **26**, 294–309 (2000).
80. A.-M. Bacon, *et al.*, Nam Lot (MIS 5) and Duoi U'Oi (MIS 4) Southeast Asian sites revisited: Zooarchaeological and isotopic evidences. *Palaeogeography, Palaeoclimatology, Palaeoecology* **512**, 132–144 (2018).
81. C. J. Still, J. A. Berry, G. J. Collatz, R. S. DeFries, Global distribution of C_3 and C_4 vegetation: Carbon cycle implications. *Global Biogeochem. Cycles* **17**, 1006 (2003).
82. M. J. Kohn, Carbon isotope compositions of terrestrial C_3 plants as indicators of (paleo)ecology and (paleo)climate. *PNAS* **107**, 19691–19695 (2010).
83. H. Friedli, H. Lötscher, H. Oeschger, U. Siegenthaler, B. Stauffer, Ice core record of the $^{13}C/^{12}C$ ratio of atmospheric CO_2 in the past two centuries. *Nature* **324**, 237 (1986).
84. L. K. Ayliffe, A. R. Chivas, Oxygen isotope composition of the bone phosphate of Australian kangaroos: Potential as a palaeoenvironmental recorder. *Geochimica et Cosmochimica Acta* **54**, 2603–2609 (1990).
85. J. D. Bryant, B. Luz, P. N. Froelich, Oxygen isotopic composition of fossil horse tooth phosphate as a record of continental paleoclimate. *Palaeogeography, Palaeoclimatology, Palaeoecology* **107**, 303–316 (1994).
86. M. J. Kohn, Predicting animal $\delta^{18}O$: Accounting for diet and physiological adaptation. *Geochimica et Cosmochimica Acta* **60**, 4811–4829 (1996).
87. S. Pederzani, K. Britton, Oxygen isotopes in bioarchaeology: Principles and applications, challenges and opportunities. *Earth-Science Reviews* **188**, 77–107 (2019).
88. M. J. Kohn, M. J. Schoeninger, J. W. Valley, Herbivore tooth oxygen isotope compositions: Effects of diet and physiology. *Geochimica et Cosmochimica Acta* **60**, 3889–3896 (1996).

89. J. D. Bryant, P. N. Froelich, A model of oxygen isotope fractionation in body water of large mammals. *Geochimica et Cosmochimica Acta* **59**, 4523–4537 (1995).
90. H. C. Fricke, W. C. Clyde, J. R. O'Neil, Intra-tooth variations in $\delta^{18}O$ (PO_4) of mammalian tooth enamel as a record of seasonal variations in continental climate variables. *Geochimica et Cosmochimica Acta* **62**, 1839–1850 (1998).
91. H. C. Fricke, W. C. Clyde, J. R. O'Neil, P. D. Gingerich, Evidence for rapid climate change in North America during the latest Paleocene thermal maximum: oxygen isotope compositions of biogenic phosphate from the Bighorn Basin (Wyoming). *Earth and Planetary Science Letters* **160**, 193–208 (1998).
92. W. Dansgaard, Stable isotopes in precipitation. *Tellus* **16**, 436–468 (1964).
93. N. Buchmann, J.-M. Guehl, T. S. Barigah, J. R. Ehleringer, Interseasonal comparison of CO_2 concentrations, isotopic composition, and carbon dynamics in an Amazonian rainforest (French Guiana). *Oecologia* **110**, 120–131 (1997).
94. N. Buchmann, J. R. Ehleringer, CO_2 concentration profiles, and carbon and oxygen isotopes in C3 and C4 crop canopies. *Agricultural and Forest Meteorology* **89**, 45–58 (1998).
95. D. McCarroll, N. J. Loader, "Isotopes in tree rings" in *Isotopes in Palaeoenvironmental Research*, Developments in Paleoenvironmental Research., (Springer, Dordrecht, 2006), pp. 67–116.
96. N. J. van der Merwe, E. Medina, The canopy effect, carbon isotope ratios and foodwebs in amazonia. *Journal of Archaeological Science* **18**, 249–259 (1991).
97. J. C. Vogel, Isotopic assessment of the dietary habits of ungulates. *South African Journal of Science* **74**, 298–301 (1978).
98. J. R. Ehleringer, C. B. Field, Z. Lin, C. Kuo, Leaf carbon isotope and mineral composition in subtropical plants along an irradiance cline. *Oecologia* **70**, 520–526 (1986).
99. J. R. Ehleringer, Z. F. Lin, C. B. Field, G. C. Sun, C. Y. Kuo, Leaf carbon isotope ratios of plants from a subtropical monsoon forest. *Oecologia* **72**, 109–114 (1987).
100. E. Medina, G. Montes, E. Cuevas, Z. Rokzandic, Profiles of CO_2 concentration and $\delta^{13}C$ values in tropical rain forests of the upper Rio Negro Basin, Venezuela. *Journal of Tropical Ecology* **2**, 207–217 (1986).
101. L. da S. L. Sternberg, S. S. Mulkey, S. J. Wright, Oxygen isotope ratio stratification in a tropical moist forest. *Oecologia* **81**, 51–56 (1989).
102. N. J. van der Merwe, E. Medina, Photosynthesis and $^{13}C/^{12}C$ ratios in Amazonian rain forests. *Geochimica et Cosmochimica Acta* **53**, 1091–1094 (1989).
103. J. Krigbaum, Neolithic subsistence patterns in northern Borneo reconstructed with stable carbon isotopes of enamel. *Journal of Anthropological Archaeology* **22**, 292–304 (2003).
104. J. Krigbaum, M. H. Berger, D. J. Daegling, W. S. McGraw, Stable isotope canopy effects for sympatric monkeys at Taï Forest, Côte d'Ivoire. *Biology Letters* **9**, 20130466 (2013).
105. H. V. Graham, *et al.*, Isotopic characteristics of canopies in simulated leaf assemblages. *Geochimica et Cosmochimica Acta* **144**, 82–95 (2014).
106. S. A. Blumenthal, J. M. Rothman, K. L. Chritz, T. E. Cerling, Stable isotopic variation in tropical forest plants for applications in primatology. *Am. J. Primatol.* **78**, 1041–1054 (2016).
107. P. Roberts, S. A. Blumenthal, W. Dittus, O. Wedage, J. A. Lee-Thorp, Stable carbon, oxygen, and nitrogen, isotope analysis of plants from a South Asian tropical forest: Implications for primatology. *Am J Primatol* **79**, n/a-n/a (2017).
108. P. Roberts, *et al.*, Direct evidence for human reliance on rainforest resources in late Pleistocene Sri Lanka. *Science* **347**, 1246–1249 (2015).
109. P. Roberts, *et al.*, Fruits of the forest: Human stable isotope ecology and rainforest adaptations in Late Pleistocene and Holocene (~36 to 3 ka) Sri Lanka. *Journal of Human Evolution* **106**, 102–118 (2017).
110. R. E. M. Hedges, L. M. Reynard, Nitrogen isotopes and the trophic level of humans in archaeology. *Journal of Archaeological Science* **34**, 1240–1251 (2007).

111. M. A. Katzenberg, A. L. Waters- Rist, "Stable isotope analysis" in *Biological Anthropology of the Human Skeleton*, (John Wiley & Sons, Ltd, 2018), pp. 467–504.
112. J. N. Aranibar, *et al.*, Nitrogen isotope composition of soils, C_3 and C_4 plants along land use gradients in southern Africa. *Journal of Arid Environments* **72**, 326–337 (2008).
113. S. H. Ambrose, Effects of diet, climate and physiology on nitrogen isotope abundances in terrestrial foodwebs. *Journal of Archaeological Science* **18**, 293–317 (1991).
114. L. A. Martinelli, *et al.*, Nitrogen stable isotopic composition of leaves and soil: Tropical versus temperate forests. *Biogeochemistry* **46**, 45–65 (1999).
115. M. P. Richards, R. E. M. Hedges, Stable isotope evidence for similarities in the types of marine foods used by Late Mesolithic humans at sites along the Atlantic coast of Europe. *Journal of Archaeological Science* **26**, 717–722 (1999).
116. R. M. Nowak, *Walker's Mammals of the World*, 6th Ed. (Johns Hopkins University Press, 1999).
117. D. W. Macdonald, *The Encyclopedia of Mammals*, 2nd Ed. (Oxford University Press, 2009).
118. A. Johnsingh, N. Manjrekar, *Mammals of South Asia Vol. 1* (Universities Press (India) Limited, 2013).
119. A. Johnsingh, N. Manjrekar, *Mammals of South Asia Vol. 2* (Universities Press (India) Limited, 2015).
120. F. Moynier, F. Albarède, G. F. Herzog, Isotopic composition of zinc, copper, and iron in lunar samples. *Geochimica et Cosmochimica Acta* **70**, 6103–6117 (2006).
121. J.-P. Toutain, *et al.*, Evidence for Zn isotopic fractionation at Merapi volcano. *Chemical Geology* **253**, 74–82 (2008).
122. S. R. Copeland, *et al.*, Strontium isotope ratios ($^{87}Sr/^{86}Sr$) of tooth enamel: A comparison of solution and laser ablation multicollector inductively coupled plasma mass spectrometry methods. *Rapid Communications in Mass Spectrometry* **22**, 3187–3194 (2008).
123. K. Britton, V. Grimes, J. Dau, M. P. Richards, Reconstructing faunal migrations using intra-tooth sampling and strontium and oxygen isotope analyses: A case study of modern caribou (Rangifer tarandus granti). *Journal of Archaeological Science* **36**, 1163–1172 (2009).
124. C. M. Johnson, C. J. Fridrich, Non-monotonic chemical and O, Sr, Nd, and Pb isotope zonations and heterogeneity in the mafic- to silicic-composition magma chamber of the Grizzly Peak Tuff, Colorado. *Contr. Mineral. and Petrol.* **105**, 677–690 (1990).
125. S. Talamo, M. Richards, A comparison of bone pretreatment methods for AMS dating of samples >30,000 BP. *Radiocarbon* **53**, 443–449 (2011).
126. R. Longin, New method of vollagen extraction for radiocarbon dating. *Nature* **230**, 241–242 (1971).
127. G. J. van Klinken, Bone collagen quality indicators for palaeodietary and radiocarbon measurements. *Journal of Archaeological Science* **26**, 687–695 (1999).
128. S. H. Ambrose, Preparation and characterization of bone and tooth collagen for isotopic analysis. *Journal of Archaeological Science* **17**, 431–451 (1990).
129. K. P. Jochum, *et al.*, Determination of reference values for NIST SRM 610–617 glasses following ISO guidelines. *Geostandards and Geoanalytical Research* **35**, 397–429 (2011).
130. R Core Team, R: A language and environment for statistical computing. R Foundation for Statistical Computing. *R Foundation for Statistical Computing, Vienna, Austria*, 14 (2018).
131. R. H. Baayen, Analyzing linguistic data. A practical introduction to statistics. 200.
132. P. McCullagh, J. A. Nelder, *Generalized Linear Models, Second Edition* (CRC Press, 1989).
133. D. Bates, M. Mächler, B. Bolker, S. Walker, Fitting Linear Mixed-Effects Models using lme4. *arXiv:1406.5823 [stat]* (2014) (December 9, 2018).
134. H. Schielzeth, W. Forstmeier, Conclusions beyond support: overconfident estimates in mixed models. *Behav Ecol* **20**, 416–420 (2009).
135. D. J. Barr, R. Levy, C. Scheepers, H. J. Tily, Random effects structure for confirmatory hypothesis testing: Keep it maximal. *Journal of Memory and Language* **68**, 255–278 (2013).

136. J. Fox, S. Weisberg, Multivariate Linear Models in R. 31.
137. A. Field, Exploratory Factor Analysis. *Discovering Statistics Using SPSS*, 619–680 (2005).
138. W. Forstmeier, H. Schielzeth, Cryptic multiple hypotheses testing in linear models: overestimated effect sizes and the winner's curse. *Behav Ecol Sociobiol* **65**, 47–55 (2011).
139. A. J. Dobson, *An Introduction to Generalized Linear Models*, 2nd Ed. (Chapman and Hall/CRC, 2002) (December 9, 2018).
140. T. E. Cerling, J. A. Hart, T. B. Hart, Stable isotope ecology in the Ituri Forest. *Oecologia* **138**, 5–12 (2004).
141. T. E. Cerling, J. M. Harris, S. H. Ambrose, M. G. Leakey, N. Solounias, Dietary and environmental reconstruction with stable isotope analyses of herbivore tooth enamel from the Miocene locality of Fort Ternan, Kenya. *Journal of Human Evolution* **33**, 635–650 (1997).
142. N. E. Levin, S. W. Simpson, J. Quade, T. E. Cerling, S. R. Frost, Herbivore enamel carbon isotopic composition and the environmental context of Ardipithecus at Gona, Ethiopia, The Geology of Early Humans in the Horn of Africa, GeoScienceWorld Books (2008) (December 12, 2017).
143. T. E. Cerling, *et al.*, Dietary changes of large herbivores in the Turkana Basin, Kenya from 4 to 1 Ma. *PNAS* **112**, 11467–11472 (2015).
144. M. Sponheimer, *et al.*, Isotopic evidence for dietary variability in the Early Hominin Paranthropus robustus. *Science* **314**, 980–982 (2006).
145. W. Erdelen, Forest ecosystems and nature conservation in Sri Lanka. *Biological Conservation* **43**, 115–135 (1988).
146. F. Kurt, "Muntjac deer" in *Grzimek's Encyclopedia of Mammals*, (McGraw-Hill Publishing Company, 1990), pp. 137–139.
147. A. Jackson, Muntiacus muntjak (Indian muntjac). *Animal Diversity Web* (December 13, 2018).
148. J. E. Jackson, D. I. Chapman, A note on the food of Muntjac deer (Muntiacus reevesi). *Journal of Zoology* **183**, 546–548 (1977).
149. O. Ilyas, J. A. Khan, Food habits of barking deer (Muntiacus muntjak) and goral (Naemorhedus goral) in Binsar Wildlife Sanctuary, India. *Mammalia* **67**, 521–532 (2003).
150. H. W. Krueger, C. H. Sullivan, Models for carbon isotope fractionation between diet and bone. *Stable isotopes in nutrition*, 205–220 (1984).
151. K. Jaouen, What is our toolbox of analytical chemistry for exploring ancient hominin diets in the absence of organic preservation? *Quaternary Science Reviews* **197**, 307–318 (2018).
152. B. Reynard, V. Balter, Trace elements and their isotopes in bones and teeth: Diet, environments, diagenesis, and dating of archeological and paleontological samples. *Palaeogeography, Palaeoclimatology, Palaeoecology* **416**, 4–16 (2014).
153. International Atomic Energy Agency, *Reference and Intercomparison Materials for Stable Isotopes of Light Elements* (International Atomic Agency, 1995).
154. R. Gonfiantini, "Advisory group meeting on stable isotope reference samples for geochemical and hydrochemical investigations, IAEA, Vienna, 19-21 September 1983" (International Atomic Energy Agency, 1984).
155. Carol. Kendall, Elizabeth. Grim, Combustion tube method for measurement of nitrogen isotope ratios using calcium oxide for total removal of carbon dioxide and water. *Anal. Chem.* **62**, 526–529 (1990).
156. J. K. Bohlke, C. J. Gwinn, T. B. Coplen, New Reference Materials for Nitrogen-Isotope-Ratio Measurements. *Geostandards Newsletter* **17**, 159–164 (1993).
157. T. B. Coplen, *et al.*, New Guidelines for δ13C Measurements. *Anal. Chem.* **78**, 2439–2441 (2006).
158. M. J. Kohn, J. Morris, P. Olin, Trace element concentrations in teeth – a modern Idaho baseline with implications for archeometry, forensics, and palaeontology. *Journal of Archaeological Science* **40**, 1689–1699 (2013).

159. R. Lappalainen, M. Knuuttila, R. Salminen, The concentrations of Zn and Mg in human enamel and dentin related to age and their concentrations in the soil. *Archives of Oral Biology* **26**, 1–6 (1981).
160. F. O. Falla-Sotelo, *et al.*, Analysis and discussion of trace elements in teeth of different animal species. *Brazilian Journal of Physics* **35**, 761–762 (2005).
161. J. de D. Teruel, A. Alcolea, A. Hernández, A. J. O. Ruiz, Comparison of chemical composition of enamel and dentin in human, bovine, porcine and ovine teeth. *Archives of Oral Biology* **60**, 768–775 (2015).